FACULTÉ DES ÉTUDES SUPÉRIEURES ET POSTOCTORALES

uOttawa

L'Université canadienne
Canada's university

FACULTY OF GRADUATE AND POSDOCTORAL STUDIES

Daniel M. Pohl

AUTEUR DE LA THÈSE / AUTHOR OF THESIS

M.Sc. (Physics)

GRADE / DEGREE

Department of Physics

FACULTÉ, ÉCOLE, DÉPARTEMENT / FACULTY, SCHOOL, DEPARTMENT

A Study of High-Density Clathrate Hydrates in the CO_2-H_2O System

TITRE DE LA THÈSE / TITLE OF THESIS

Serge Desgreniers

DIRECTEUR (DIRECTRICE) DE LA THÈSE / THESIS SUPERVISOR

CO-DIRECTEUR (CO-DIRECTRICE) DE LA THÈSE / THESIS CO-SUPERVISOR

Zbigniew Stadnik

Peter Piercy

Manuella Vincter

Gary W. Slater

Le Doyen de la Faculté des études supérieures et postdoctorales / Dean of the Faculty of Graduate and Postdoctoral Studies

A study of high-density clathrate hydrates in the CO_2-H_2O system

Daniel M. Pohl

Thesis submitted to the
Faculty of Graduate and Postdoctoral Studies
In partial fulfillment of the requirements
For the MSc degree in Physics

Department of Physics
Faculty of Science
University of Ottawa

Library and Archives
Canada

Published Heritage
Branch

395 Wellington Street
Ottawa ON K1A 0N4
Canada

Bibliothèque et
Archives Canada

Direction du
Patrimoine de l'édition

395, rue Wellington
Ottawa ON K1A 0N4
Canada

Your file Votre référence
ISBN: 978-0-494-79714-3
Our file Notre référence
ISBN: 978-0-494-79714-3

NOTICE:

The author has granted a non-exclusive license allowing Library and Archives Canada to reproduce, publish, archive, preserve, conserve, communicate to the public by telecommunication or on the Internet, loan, distribute and sell theses worldwide, for commercial or non-commercial purposes, in microform, paper, electronic and/or any other formats.

The author retains copyright ownership and moral rights in this thesis. Neither the thesis nor substantial extracts from it may be printed or otherwise reproduced without the author's permission.

AVIS:

L'auteur a accordé une licence non exclusive permettant à la Bibliothèque et Archives Canada de reproduire, publier, archiver, sauvegarder, conserver, transmettre au public par télécommunication ou par l'Internet, prêter, distribuer et vendre des thèses partout dans le monde, à des fins commerciales ou autres, sur support microforme, papier, électronique et/ou autres formats.

L'auteur conserve la propriété du droit d'auteur et des droits moraux qui protège cette thèse. Ni la thèse ni des extraits substantiels de celle-ci ne doivent être imprimés ou autrement reproduits sans son autorisation.

In compliance with the Canadian Privacy Act some supporting forms may have been removed from this thesis.

While these forms may be included in the document page count, their removal does not represent any loss of content from the thesis.

Conformément à la loi canadienne sur la protection de la vie privée, quelques formulaires secondaires ont été enlevés de cette thèse.

Bien que ces formulaires aient inclus dans la pagination, il n'y aura aucun contenu manquant.

Canada

Abstract

Gas clathrate hydrates are inclusion compounds in which a guest gas molecule is trapped within a host cage made up of hydrogen-bonded water molecules [1]. Sequestration of CO_2 in dense hydrate form has been proposed as one solution for rising levels of CO_2 in Earth's atmosphere [2]. Recent research has predicted the existence of a high-density clathrate structure capable of realizing this goal [3]. In this thesis, powder x-ray diffraction of the CO_2-H_2O system as a function of increasing pressure (0 to 2.5 GPa) at sub-ambient temperatures (250 to 260 K) was performed in pursuit of discovering novel high-density hydrates of CO_2. In addition to previously reported clathrate structures [4], CO_2 FIS I_h, a non-clathrate structure previously unobserved in the CO_2-H_2O system but reported in other systems [5], was identified and characterized. Using similar experimental techniques, unrelated work on the structural stability of dickite, a layered silicate mineral, is also presented.

Statement of Originality

The work presented in this thesis is, to the best knowledge of its author, an original work in the field of high-pressure condensed matter physics. Sample preparation at the *Laboratoire de physique des solides denses* (LPSD) was done by the author with collaboration from author's research supervisor, Dr. Serge Desgreniers. Powder x-ray diffraction experiments at the Canadian Light Source, Raman spectroscopy experiments at LPSD, data analysis and interpretation were performed solely by the author. Data analysis was performed by the author using commercial software. This work represents the first known observation of the orthorhombic filled-ice I_h structure (FIS I_h) in the CO_2-H_2O system, a structure common to other gas hydrates forming guest-host systems. In addition, this work presents the first known observation of a structural phase transition in St. Claire Dickite at ~8.18 GPa and 295 K.

Acknowledgements

First and foremost I would like to thank my supervisor, Dr. Serge Desgreniers, for all his help and support on this project over the years. His loose hand and endless supply of patience (despite my steep learning curve!) provided me with the time and freedom to tackle and solve day to day problems in the lab on my own; an environment that has benefited my work immensely. His theoretical and practical knowledge of dense gas hydrates has helped me dig my way out of many conundrums in pursuit of the results herein. In addition, I wish to thank Serge for the many opportunities he provided for me to fly out to Saskatoon to perform powder x-ray diffraction experiments at the Canadian Light Source (CLS) at the University of Saskatchewan. Without his generous financial support I would not have been able to perform this research.

Secondly, I would like to thank my colleagues in the *Laboratoire de physique des solides denses* (LPSD) in the Physics Department at the University of Ottawa. Thanks to Dr. Jesse Smith for helping me with everything from much needed advice to technical support. His "MacGyver-esque" creativity and insight often helped me reach simple, yet elegant solutions in the lab. His professionalism and work ethic set a standard for me during my time at LPSD. Thank you to Catherine Aldous, my colleague and best friend of 5 years, for your advice, friendship, and for keeping me sane through the tough times. I couldn't have done it without you! Thanks to Laura Downie and Alexandre Bouchard for your advice, comradery and for providing much needed diversions from research without which I would have been worse for.

I am indebted to Phillip Vinten for "grammatical advice" during the editing of this thesis. I hope it wasn't as painful for you to read as it was for me to see that much red ink!

Thanks to Dr. Ning Chen and Dr. Chang-Yong Kim for their help in the upkeep of the Hard X-ray MicroAnalysis beamline (HXMA) at the CLS as well as their help with overcoming the challenges faced during the experiments we performed there.

Most of all I would like to thank my parents, Emilia and Karol Pohl, for their support and encouragement to continue and do the best that I can in my studies and in the world. Thank you for your love, moral support, advice and patience. Also, thank you for putting up with far too many late night noisy returns from the lab and for tolerating my wide-range of moods and attitudes during these past two years! You are the best!

Table of Contents

Abstract ii

Statement of Originality iii

Acknowledgements iv

Table of Contents vi

List of Figures viii

List of Tables xiv

Introduction xvi

Chapter 1 - Research at extreme conditions

1.1 - Introduction to pressure 1

1.2 - Generating high static pressure: the diamond anvil cell 6

1.3 - Introduction to pressure measurement 16

1.4 - The ruby fluorescence method 17

1.5 - Introduction to temperature 20

1.6 - Temperature measurement 22

1.7 - Temperature correction for the ruby fluorescence technique 24

1.8 - X-ray diffraction 26

1.9 - Synchrotron radiation 29

1.10 - Experimental set-up at the Canadian Light Source Hard X-ray MicroAnalysis beamline... 31

1.11 - Taking a calibration standard 35

1.12 - X-ray image processing of the standard 36

1.13 - Data analysis: unit cell indexing 40

1.14 - Data analysis: Rietveld refinement 42

1.15 - Raman spectroscopy 43

1.16 - Summary 45

Chapter 2 - Gas clathrate hydrates

2.1 - Gas clathrate hydrates 47

2.2 - Hydrate structures 48

2.3 - Hydrate formation and bonding 50
2.4 - Stoichiometry 53
2.5 - Hydrate formation conditions 54
2.6 - Gas sequestration 56

Chapter 3 - The CO_2-H_2O system: background and sample preparation

3.1 - The CO_2-H_2O system 60
3.2 - CO_2 Hydrate: sample synthesis and loading 65

Chapter 4 - The CO_2-H_2O system: analysis and results

4.1 - Introduction to powder x-ray diffraction experiments 70
4.2 - sI CO_2 Hydrate 71
4.3 - CO_2 FIS I_h 77
4.4 - Dissociation into Ice VI and CO_2-I 82

Chapter 5 - The CO_2-H_2O system: discussion and conclusion

5.1 - Comparison of CO_2 hydrate sI to other systems 84
5.2 - Comparison of CO_2 FIS I_h to other systems 89
5.3 - Unknown Phases 93
5.4 - Dissociation into Ice VI and CO_2-I 97
5.5 - Summary, conclusions and future work 98

Chapter 6 - Structural phase transition in dickite at high pressure and room temperature

6.1 - Introduction to dickite 103
6.2 - Powder x-ray diffraction of dickite 104
6.3 - Raman spectroscopy of dickite 111

Licenses 117

References 118

List of Figures

Chapter 1

Figure 1.1 – For a closed system, an increase in volume will cause a decrease in pressure (top). Similarly, an increase in pressure will cause a decrease in volume (bottom). 2

Figure 1.2 – A first order phase transition is characterized by a finite discontinuity in volume. 4

Figure 1.3 – Schematic diagram of the interior of the Earth. 360 GPa of pressure separates the conditions on the surface to the inner core [13]. 5

Figure 1.4 – Schematic diagram of a Bridgman high pressure cell. Two tungsten-carbide anvils were forced together by a large hydraulic press. Pressures achieved were as high as 10 GPa. 7

Figure 1.5 – The first diamond anvil cell, created by Charles E. Weir and colleagues of the National Bureau of Standards in 1958. This photo is a contribution of the National Institute of Standards and Technology.. 8

Figure 1.6 – The diamond anvil cell. Two opposing diamonds and a metal gasket with a hole drilled into it form a compression chamber for high pressure study of a sample. [21] 9

Figure 1.7 – In the above photographs taken through one anvil of the diamond anvil cell with transmitted light, pressure is applied to a sample mixture of N_2 and CH_4 which initially appears transparent. The sample suddenly gains texture as it crosses a phase boundary, visually indicating this transition to the experimenter. The ability to watch the sample under a microscope is thus very useful. (Pictures courtesy of Catherine Aldous, LPSD) 10

Figure 1.8 – Gasket preparation. A 0.25mm thick steel gasket is placed between the diamond anvils (left). Next, pressure is applied to indent the gasket to the desired thickness (middle). Finally, a hole is drilled through the indentation (right). 11

Figure 1.9 - Under a microscope the culet of a 16-faceted anvil shows signs of damage. A large subsurface fault can be seen by the darkened region near the bottom, as well as a large crack running along the culet's surface. (Picture courtesy of Serge Desgreniers, LPSD) 12

Figure 1.10 – The diamond anvil cell used in this research. The piston and cylinder sides (left) are machined to fit together precisely when assembled (right). The diamond anvils can be seen at the centers of the piston and cylinder (left). 13

Figure 1.11 – Four pressure screws (only two are shown in this photograph) are used to pull the piston and cylinder together and generate the high pressures inside the compression chamber. 14

Figure 1.12 – The ruby fluorescence method. One or more ruby microspheres (~15μm in diameter) are placed in the compression chamber (left). The fluorescence spectrum from ruby is characterized by two strong peaks, R_1 and R_2, that redshift in wavelength with increasing pressure (right). 18

Figure 1.13 – Comparison of pressure formulae for the ruby fluorescence technique [24, 25, 26]. All calibrations are comparable below 10 GPa which is the pressure limit in this work. 19

Figure 1.14 – The pressure-temperature phase diagram of H_2O [28] 20

Figure 1.15 – An end welded Type K thermocouple. 22

Figure 1.16 – A thermocouple enters the cell through an unused screw hole on the back (left), runs across the bottom of the cell (middle) and is fixed to the diamond and insulated with tape (right).. 23

Figure 1.17 – A decrease in temperature causes the ruby fluorescence spectrum to blueshift. Because the ruby fluorescence method for calculating pressure depends on knowing the R_1 peak position before and after the application of pressure, an appropriate temperature correction must be applied. 25

Figure 1.18 – Single crystal diffraction creates an array of Bragg spots on an area detector resulting from the crystal orientation with respect to the incident x-ray beam 27

Figure 1.19 – Powder x-ray diffraction creates intensity rings on an area detector due to the random orientation of sample crystallites. The right panel gives an example of a powder diffraction image. The white part in the image is the shadow cast by the beam stop 28

Figure 1.20 – Schematic diagram of the HXMA beamline at CLS [adopted from reference 13]. 31

Figure 1.21 – Upstream components used for high pressure x-ray diffraction at the CLS HXMA beamline. He flight tube (1), collimator assembly (2), sample (3), beamstop (4), and MAR345 imaging plate area detector (5) 32

Figure 1.22 – With an x-ray beam diameter comparable to the sample diameter, diffraction off the metal gasket results (left). Broad gasket rings often obscure sample Debye rings making structural determination difficult. The use of a 60 µm diameter clean-up aperture aligned close to the sample eliminates this problem caused by the gasket. Clearer sample Debye rings arising from the sample only can now be seen (right). 34

Figure 1.23 – A 2D x-ray diffraction image is integrated to get a 1D x-ray diffraction pattern. 35

Figure 1.24 – A cubic calibration standard like lanthanum hexaboride (NIST SRM 660a) [33] is chosen because it produces a strong high symmetry pattern 36

Figure 1.25 – Scattering geometry. 37

Figure 1.26 – Fit2D calculates the experimental configuration parameters that define the geometry of the diffraction experiment by analyzing the pattern of a calibration standard. 38

Figure 1.27 – The x-ray diffraction pattern of lanthanum hexaboride is fit to a cubic lattice in XRDA. The expected lattice parameter is recovered within the range of error. This indicates a successful calibration has been performed. Observed intensities do not match theoretical intensities due to the fact that they were calculated assuming single crystal diffraction. 39

Figure 1.28 – The presence of very broad dark rings and very thin lighter rings in a diffraction image may indicate two separate phases in the sample. A similar indicator is the presence of both spotty rings and complete rings. 40

Figure 1.29 – Raman spectra of Argon clathrate hydrate plotted with increasing pressure. The left panel shows the structural lattice modes, while the right panel shows the OH stretching modes of

the hydrate. A structural phase transition is characterized in a Raman spectrum by a sudden shift, disappearance, or appearance of vibrational modes as is the case here at ~1.00 GPa. (Figure taken from Shimizu et al. [40]) 44

Chapter 2

Figure 2.1 – Cage polyhedra: a) pentagonal dodecahedron (5^{12}), b) tetrakaidecahedron ($5^{12}6^{2}$), c) hexakaidecahedron ($5^{12}6^{4}$), d) irregular dodecahedron ($4^{3}5^{6}6^{3}$), and icosahedron ($5^{12}6^{8}$). Gas clathrate hydrate structures f) cubic structure I, g) cubic structure II, and h) hexagonal structure H. [Figures by Komarov *et al.* [15]] 49

Figure 2.2 – A hexagonal lattice of H_2O molecules similar to Ice I_h (left). Gas molecules pack into channels formed between ice layers (right) in the "filled ice" structure. [Figures by Komarov *et al.* [15]]. 50

Figure 2.3 – Dissociation lines for some gas clathrate hydrates as a function of pressure and temperature. The phases of pure H_2O (dark lines) are overlaid to give perspective. [Data accumulated from various sources [26-29]] 55

Figure 2.4 – Guest atoms or molecules shown with increasing diameter and the known hydrate structures they adopt as a function of increasing pressure. Clathrate hydrates involved are the cubic structure I (sI), cubic structure II (sII), hexagonal structure (sH), and the tetragonal structure (sT). Filled ice structures resembling Ice I_h , Ice Ic, and Ice II are labeled (FIS I_h), (FIS I_c) and (FIS II) respectively. Systems that dissociate in the shown pressure range are labeled (Dis). Data accumulated from various sources [12, 24, 30-42]. 58

Chapter 3

Figure 3.1 - Superimposed phase diagrams of pure H_2O, pure CO_2, and the known dissociation boundary of CO_2 sI hydrate [3, 4, 5]. The l and g subscripts refer to liquid and gaseous phases respectively 60

Figure 3.2 – Superimposed phase diagram of pure H_2O (black) and CO_2 clathrate hydrate (blue). The shaded region in blue represents an additional phase discovered, but unidentified, by Honda *et al.* [7]. 63

Figure 3.3 – Guest molecules shown with increasing diameter and the hydrate structures they adopt as a function of increasing pressure. The region of interest in this work for the CO_2-H_2O system is labeled in grey. Clathrate hydrate structures involved are the cubic structure I (sI), cubic structure II (sII), hexagonal structure (sH), and the tetragonal structure (sT). Filled ice structures resembling Ice I_h are labeled (FIS I_h). Systems that dissociate in the indicated pressure range are labeled (Dis). A loose trend can be seen in structures that are adopted with increasing pressure 64

Figure 3.4 - High pressure containment vessel for synthesizing CO_2 clathrate hydrate (left). 5 steel rods are inserted in the vessel along with the constituents (center). The vessel is attached to a motor-driven rotator and then placed into a freezer (right) 66

Figure 3.5 – Conditions maintained to synthesize CO_2 hydrate in this work. Freezer temperature cycling and absorption of gas into the ice caused a range of temperature and pressure conditions represented by the arrows. At all times conditions were kept below the hydrate dissociation boundary. 67

Figure 3.6 – Cryogenic loading of CO_2 hydrate. The DAC cylinder is half immersed in liquid nitrogen to keep conditions below the hydrate dissociation boundary. Hydrate crystals are smashed into a fine powder atop the gasket and then pushed into the compression chamber. The cell must be closed before frost contaminates the chamber. 68

Chapter 4

Figure 4.1 – X-ray diffraction patterns of the CO_2 - H_2O system recorded with increasing pressure. 1) Pure sI CO_2 Hydrate. 2) Phase mixture containing FIS I_h , Ice VI, and an unknown phase. 3) Phase mixture containing FIS I_h, Ice VI, CO_2, and an unknown phase. 4) Mixture of Ice VI and CO_2. 70

Figure 4.2 – Comparison of simulated x-ray diffraction pattern for CO_2 hydrate sI (top) and observed pattern (bottom). Certain peaks that exist in the simulated pattern are absent from the observed pattern between the angles of 4° and 7° (2θ). 72

Figure 4.3 - Comparison of x-ray diffraction simulated pattern for CO_2 hydrate sI having low CO_2 site occupancy (top) and observed pattern (bottom). The (200), (210), and (211) peaks that were strong for full cage occupancy between the angles 4° and 7° (2θ) have now vanished. The calculated and observed x-ray diffraction patterns closely resemble each other 73

Figure 4.4 - Indexing of peaks recorded by x-ray diffraction of sI CO_2 hydrate done in XRDA. All peaks in the diffraction pattern match expected reflections for an sI clathrate with low guest site occupancy. 74

Figure 4.5 – Rietveld refinement of x-ray diffraction pattern of CO_2 hydrate sI at 0.27 GPa and 260 K. The black line represents the experimental data, the red dots represent calculated intensities, the tick marks represent calculated peak positions and the line at the bottom is the difference between the calculated and observed pattern. 76

Figure 4.6 – Superimposed phase diagrams of H_2O [28] and CO_2 [79] in the region of interest. Uncertainty in pressure or temperature measurements make sorting out occluded constituent H_2O difficult because as many as 6 different phases are expected in this region of the phase diagram. 78

Figure 4.7 – Indexing of the x-ray diffraction pattern recorded at 0.45 GPa and 250K with CO_2 FIS I_h (green) and occluded Ice VI (red) at 0.45 GPa and 250 K. Blue tick marks represent an unknown phase in the mixture. 79

Figure 4.8 - Histogram (red bars) of CO_2 sH hydrate overlaid over the diffraction pattern taken at 0.45 GPa and 250 K. Blue tick marks represent unidentified peaks after the fitting of CO_2 FIS I_h. No match can be found between the two in this diffraction pattern, indicating that CO_2 sH hydrate is likely not present. 81

Figure 4.9 – Indexing of peaks recorded by x-ray diffraction at 0.94 GPa and 250 K. All peaks in the diffraction pattern match expected reflections for either solid CO_2 (red) or Ice VI (green). * indicate two unidentified peaks likely arising from a contaminant. 83

Chapter 5

Figure 5.1 Unit cell volumes (left) and V/V_0 (right) vs. pressure of sI clathrate hydrate for three different systems. Overlaid are Birch-Murnaghan equations of state that best fit the available data (fit parameters are given in the inset table in the left panel). Data for xenon and methane hydrates are compiled from many sources [10, 74, 83, 88-91]. The parameter marked with an asterisk was altered to better fit the published data [89]. Uncertainty on V, V_o, K_o, and P for CO_2-sI are 8 $Å^3$, 20 $Å^3$, 0.5 GPa, and 0.4 GPa respectively. 84

Figure 5.2 - Comparison of orthorhombic FIS I_h lattice parameters vs pressure for three different systems. Data for Ar-H_2O and CH_4-H_2O systems taken from works by Yang *et al.* [97] and Hirai *et al.*[66] respectively. Data points shown with squares, circles, or triangles represent a, b, and c lattice parameters respectively. The left graph shows the entire range of data points in which methane FIS I_h exists, while the right graph shows the low pressure region of interest. The b and c lattice parameters are nearly identical for the CO_2 FIS I_h and thus overlap on the graph. Uncertainty on lattice parameters and P for CO_2 FIS I_h are 0.01 Å and 0.4 GPa respectively. 89

Figure 5.3 – Comparison of FIS I_h unit cell volumes vs pressure for three different systems. Actual data points are shown as well as Birch-Murnaghan equation of state fits proposed by the authors [66, 97]. The left graph shows the entire range of data points used to fit the EOS to methane FIS while the right graph shows the low pressure region of interest. The volume parameter marked with an asterisk was altered to better fit the author's data. Uncertainty on V, V_o, K_o, and P for CO_2 FIS I_h are 2 $Å^3$, 10 $Å^3$, 2 GPa, and 0.4 GPa respectively. 91

Figure 5.4 - Comparison of FIS I_h V/V_0 vs. pressure graph for three different systems. 92

Figure 5.5 - Observed phases in the CO_2-H_2O system represented as arrows and overlaid by the phase diagram of pure H_2O [28] and CO_2 [79]. The vertical height of the green bars is representative of the experimental temperature range. The sI CO_2 hydrate phase transforms into a phase mixture containing CO_2 FIS I_h and an unknown phase at 0.45 GPa. At 0.70 GPa the peaks of the unknown phase change enough to call this as a separate unknown phase. Beyond 0.95 GPa, CO_2 hydrate is unstable against the formation of its constituents. Uncertainty on pressure measurements is 0.4 GPa. 94

Figure 5.6 – Unit cell volume vs. pressure for Ice VI and CO_2-I observed throughout the course of the experiment. Data points of occluded material before and after complete dissociation of hydrates are included. Data is in agreement with Birch-Murnaghan equations of state (parameters in the inset table) based on other high pressure works on these pure substances [98-101]. Uncertainty for V and P data points are 2 $Å^3$ and 0.4 GPa respectively. 97

Figure 5.7 – New proposed phase diagram for the CO_2-H_2O system. Thin black lines represent the phase diagram for pure H_2O. The solid blue line represents the known dissociation boundary for CO_2 hydrate sI. Thick solid light green lines represent new phase boundaries of CO_2 FIS I_h. Dotted lines represent extrapolations. The dark green dotted line at 0.7 GPa is the proposed phase boundary

between two unidentified phases coexisting with FIS I_h. Dissociation occurs at 0.94 GPa in this system. 100

Figure 5.8 - Guest species (atoms or molecules) shown with increasing diameter and the hydrate structures they adopt as a function of increasing pressure. The structures found in this work for the CO_2-H_2O system are included. Clathrate hydrates involved are the cubic structure I (sI), cubic structure II (sII), hexagonal structure (sH), and the tetragonal structure (sT). The filled ice structure resembling Ice I_h is also indicated (FIS I_h). Two unknown structures are labeled (U1) and (U2). Systems that dissociate in the shown pressure range are labeled (Dis). 101

Chapter 6

Figure 6.1 – Powder x-ray diffraction patterns of St. Claire Dickite from sample 1. The changes observed in the x-ray diffraction patterns indicate a sequence of three different phases labeled 1-3. 104

Figure 6.2 – Indexing of x-ray diffraction pattern recorded from dickite's intitial phase at 0.09 GPa at room temperature. Note the x-ray diffraction pattern has been background subtracted. The unit cell is monoclinic with the space group cc. The lattice parameters are a = (5.15 ± 0.01) Å, b = (8.93 ± 0.01) Å, c = (14.42 ± 0.01) Å, with angle β = (96.77 ± 0.01) $^{\circ}$, giving a unit cell volume v = (659 ± 1) $Å^3$.. 105

Figure 6.3 - Indexing of x-ray diffraction pattern recorded from dickite's second phase, at 3.00 GPa and 295 K. The unit cell is monoclinic with the space group cc, lattice parameters a = (5.10 ± 0.01) Å, b = (8.79 ± 0.01) Å, c = (13.85 ± 0.01) Å, angle β = (89.43 ± 0.01) $^{\circ}$, and unit cell volume v = (620 ± 1) $Å^3$.. 107

Figure 6.4 – Lattice parameters (left), beta angle (top right), and volume (bottom right) of St. Claire Dickite as functions of increasing pressure. The phase transition at 2.20 GPa can be described as a "layer-slipping", which occurs when one sheet settles onto another, causing the c-axis to suddenly compresses and beta angle to shrink. The reduction of the c lattice parameter naturally causes a reduced unit cell volume. Uncertainty for lattice parameters, β, V and P are 0.01 Å, 0.01 $^{\circ}$, 1 $Å^3$ and 0.1 GPa respectively. 109

Figure 6.5 –Background subtracted powder x-ray diffraction pattern of dickite's unknown third phase recorded at 10.04 GPa and 295 K. Inset shows the pattern without background subtraction. 110

Figure 6.6 – Raman spectra of the OH stretching modes plotted as a function of pressure. In the first sample (bottom panel) a clear transition is observed between 2.20 GPa and 2.30 GPa. In the second sample (top panel), a clear transition is seen between 8.18 GPa and 8.48 GPa. Uncertainty on pressure measurements are 0.1 GPa. 112

Figure 6.7 – Band wavenumber vs. pressure for the OH stretching modes of St. Claire Dickite. Two transitions are seen and marked with dotted vertical lines. 113

Figure 6.8 - Raman structural lattice modes overlaid as a function of pressure. Phase transitions are not as obvious as they were for the OH stretching modes, but can be marked by a slight down-shift

in peak position. In the first sample (bottom panel) the transition occurs between 2.20 GPa and 2.30 GPa. In the second sample (top panel), the transition occurs between 8.18 GPa and 8.48 GPa. Uncertainty on pressure measurements are 0.1 GPa. 114

Figure 6.9 – Peak position vs. Pressure graph of the lattice modes of Ste. Claire Dickite. Two transitions are seen and marked with dotted vertical lines. 115

List of Tables

Chapter 1

No Tables

Chapter 2

Table 2.1 – Comparison of cage diameter to maximum guest diameter for gas clathrate hydrates. The guest must have a diameter smaller than the cage diameter. [Adapted from reference 53]. 52

Chapter 3

No Tables

Chapter 4

Table 4.1 – Miller indices, observed Bragg angles (2θ), and d-spacings for diffraction peaks for sI CO_2 hydrate at 0.27 GPa and 260 K. Low differences between expected and observed d-spacings indicate a good fit to the cubic structure with lattice parameter a = (11.87 ± 0.01) Å. 75

Table 4.2 – Refined fractional coordinates of atoms in CO_2 sI hydrate. Occupancies of guest atoms are presented as found by FullProf. Uncertainties on occupancy could not be evaluated and are certainly larger than 10% 76

Table 4.3 - Miller indices, observed Bragg angles (2 θ), and d-spacings for diffraction peaks for CO_2 FIS I_h at 0.45 GPa and 250 K. The small difference between expected and observed d-spacings indicate a good fit to the orthorhombic structure with lattice parameters a = (4.85 ± 0.01) Å, b = (7.65 ± 0.01) Å, c = (7.65 ± 0.01) Å 80

Table 4.4 – List of d-spacings for unknown peaks at 0.45 GPa and 250K (left), and at 0.93 GPa and 250 K (right). It is suggested in Chapter 5 that two separate unknown phases (1 and 2) coexist with CO_2 FIS I_h at different pressures. 80

Table 4.5 – Atomic fractional coordinates, unit cell symmetry, space group, and lattice parameters used to generate the histogram for CO_2 sH hydrate shown in Figure 4.8. Guest atoms are also labled to which cage they belong in brackets. Data taken from Manakov et al. [70]. 82

Chapter 5

Table 5.1 – Cage occupancies, hydration numbers, and experimental conditions for several sI hydrate forming systems. 86

Chapter 6

Table 6.1 - Miller indices, observed Bragg angles (2 θ), and d-spacings for diffraction peaks of St. Claire Dickite at 0.09 GPa and 295 K. The small differences between the expected and observed d-spacings indicate a good fit to the monoclinic structure. 106

Table 6.2 - Miller indices, observed Bragg angles (2 θ), and d-spacings for diffraction peaks of St. Claire Dickite at 3.00 GPa and 295 K. The small difference between expected and observed d-spacings indicate a good fit to the monoclinic structure. 108

Table 6.3 - Observed Bragg angles (2 θ) and d-spacings for diffraction peaks of St. Claire Dickite's unknown third phase at 10.04 GPa and 295 K. 110

Introduction

The field of high-pressure condensed matter physics is a diverse realm yielding results in a wide range of subjects of both theoretical and industrial interest. The advent of x-ray diffraction techniques in the early 1900's has led to the structural characterization of many materials and has advanced our knowledge of the condensed state. With the introduction of the diamond anvil cell (DAC) in 1958 [6], material characterization was able to be pursued up to pressures on the order of gigapascals (GPa). Properties that do not exist at ambient conditions could now be explored in the laboratory. Pressure induced structural phase transitions, novel superconducting materials [7], metal-semiconductor transitions [8], novel energetic materials [9], and even insight into formation conditions on planetary bodies [10] are among the results coming from this exciting field.

One particularly interesting group of materials that has been the subject of increasing research are gas clathrate hydrates. Originally discovered in 1811 by Sir Humphrey Davy [11], gas clathrate hydrates are inclusion compounds in which a guest gas molecule is trapped within a host cage made up of hydrogen-bonded water molecules [1]. Gas clathrate hydrates exhibit interesting properties such as variable stoichiometry and wide-ranging stability conditions. The potential for these compounds to be used as a storage medium for fuel (methane hydrate) and the sequestration of greenhouse gasses, like carbon dioxide, into more manageable forms has become the motivation for this and other recent research [1].

The main body of this thesis describes research carried out on high-pressure gas clathrate hydrate phases in the CO_2-H_2O system. Powder x-ray diffraction is used to characterize the structures that the CO_2-H_2O system assumes at conditions of increasing pressure (0 to 2.5 GPa) and sub-ambient temperatures (250 to 260 K). Conclusions are then made on the potential use of gas clathrate hydrates to sequester atmospheric CO_2.

In the final chapter, a second project (unrelated to gas clathrate hydrates) concerning high-pressure structural phase transitions in dickite is presented. Dickite is a layered silicate mineral from the Kaolin group, a group of "sheet silicates" which exhibit interesting compression behaviour. Results from powder x-ray diffraction experiments and vibrational (Raman) spectroscopy as a function of pressure are presented and discussed.

This thesis is organized as follows: an overview of high-pressure research is given in Chapter 1, along with the theory and techniques behind powder x-ray diffraction and Raman spectroscopy, the two main experimental techniques used in this work. Chapter 2 provides a detailed description of gas clathrate hydrates, the topic of this work, including a brief history, their structure(s), formation conditions, and motivations for the present research. In Chapter 3, the discussion focuses on the specific hydrate-forming system pertaining to this work: the CO_2-H_2O system. Its history and interest to researchers is reviewed, and then the methods used for sample synthesis and preparation for experimentation in this work are discussed. Chapter 4 gives an overview of the x-ray diffraction experiments performed on CO_2 hydrate for this work, as well as the results obtained from those experiments. Finally, Chapter 5 compares the results shown in Chapter 4 to the works of others on the CO_2-H_2O system and other similar hydrate-forming systems, and conclusions are drawn. This chapter finishes by suggesting ways to improve and continue the work on the CO_2-H_2O system. Chapter 6 contains the details of a side project examining phase transitions in dickite.

Chapter 1 - Research at extreme conditions

Pressure

1.1 – Introduction to pressure

When one endeavours to explore the behaviour of matter at extreme conditions, an understanding of relevant thermodynamic variables is necessary. The first variable to consider, pressure, is defined as the force per unit area exerted normal to a surface:

$$P = \frac{F}{A} \tag{1}$$

The conjugate variable to pressure is volume, defined as the amount of three dimensional space that a substance occupies. Studying the relationship between these two variables will help in understanding the motivations behind this research.

All materials are composed of collections of atoms and/or molecules, ordered into specific phases (solid, liquid, gas) presenting a definite structure that depends on the nature and strength of the interactions between the constituents. Whether solid, liquid or gas, all forms of matter occupy a certain volume at a certain pressure. Imagine, for example, a gas existing in a container of volume V at a pressure P. A valve separates the container from another container where near vacuum exists. It is known that if the valve were opened, the volume available to the gas would suddenly increase, and it would expand into the second container, decreasing the pressure.

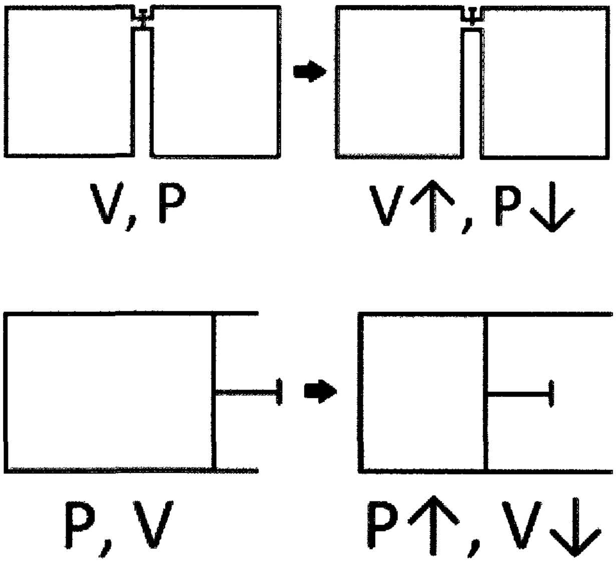

Figure 1.1 – For a closed system, an increase in volume will cause a decrease in pressure (top). Similarly, an increase in pressure will cause a decrease in volume (bottom).

One can look at this from the other perspective. If the pressure on a gas were increased by an external application of force on its volume, the volume would in that case decrease. As the volume decreases, interactions between the gas' individual constituents will increase until, eventually, in order to minimize free energy, the nature of the substance will change. This is referring to what is known as a "phase transition". A phase transition occurs when the nature of bonding in a material is altered. With sufficient application of pressure, a gas may thus be transformed into its liquid state. Similarly, a liquid may be transformed into a solid with the application of a high enough pressure, and a solid into a solid of a different crystal structure. High pressure research focuses on solid-solid phase transitions at high pressures.

First-order phase transitions

A better definition of a phase transition is necessary to understand what exactly happens to, for instance, a solid subjected to pressures at this transition point. Thermodynamics tells us that all systems tend to minimize their total energy and come to an equilibrium state after being forced away from a previous equilibrium. A system's energy can by expressed by the following relation:

$$E = TS - PV \tag{2}$$

where E is the energy, and T, S, P, and V are the thermodynamic variables temperature, entropy, pressure, and volume respectively. The change in energy of a system can be expressed by the differential of this expression:

$$dE = TdS - PdV \tag{3}$$

Only the intensive variables T and P can be directly changed in an experiment. The extensive variables S and V can only be changed as an indirect result of a change in the intensive variables. Various thermodynamic potentials have been introduced to describe different processes, and the one that best describes a phase transition is the Gibb's Free energy:

$$G = E + PV - TS \tag{4}$$

Within the boundaries of a phase, the Gibb's free energy increases with an increase in pressure, and decreases with an increase in temperature. At a phase boundary, however, a transition occurs where the system either absorbs or releases a large amount of energy in an attempt to reach equilibrium. During this transition, pressure and temperature remain constant, and as a result there must also be no change in Gibb's free energy. The required change in energy must therefore occur through a change in volume and entropy.

$$dG = VdP - SdT = 0 \quad (5)$$

$$\left(\frac{dG}{dP}\right)_T = V, \qquad \left(\frac{dG}{dT}\right)_P = -S \quad (6,7)$$

Such a transition in a solid is known as a first order phase transition because its Gibb's free energy is discontinuous at its first derivative by a finite amount. A graph of pressure vs. volume across a first order phase transition would resemble Figure 1.2:

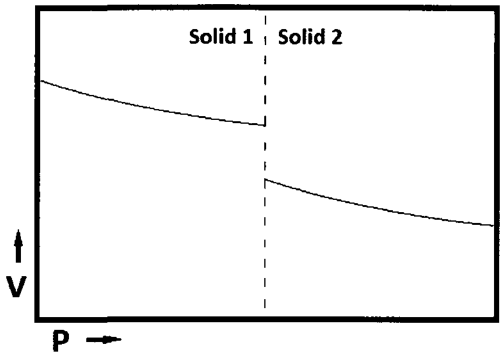

Figure 1.2 – A first order phase transition is characterized by a finite discontinuity in volume.

When a solid material is subjected to pressure, its atoms get closer and closer together. The reduction in volume with pressure for a solid can be modeled by an equation of state provided enough compression data is recorded. The model used in this work is the Birch-Murnaghan equation of state [12] given in Equation 8:

$$V = V_0\left[1 + K_0'\left(\frac{P}{K_0}\right)\right]^{-\frac{1}{K_0'}} \quad (8)$$

where V_0 is the volume at zero pressure, P is the pressure, K_0 is the bulk modulus, and K_0' is the rate of change of the bulk modulus with pressure. If the pressure continues to increase and a phase boundary is encountered, the lattice will reorganize itself into a different structure with, most likely, a denser packing of atoms in order to reach a new equilibrium. The denser packing naturally means that a large volume change must take place and a new equation of state will be needed to describe further compression.

High Pressure

The "high pressures" referred to in this research are on the order of gigapascals (GPa). To put this into perspective, consider atmospheric pressure as a reference. 1 GPa is equivalent to about 10,000 times the atmospheric pressure at sea level. At the deepest part of Earth's oceans, the Mariana Trench in the western Pacific Ocean, pressures reach ~0.1 GPa, or 1000 atmospheres [13]. Inside the Earth, pressures increase greatly with depth, as can be seen in Figure 1.3. The Earth's core is estimated to have a pressure of ~360 GPa, or 3.6×10^6 atm [13].

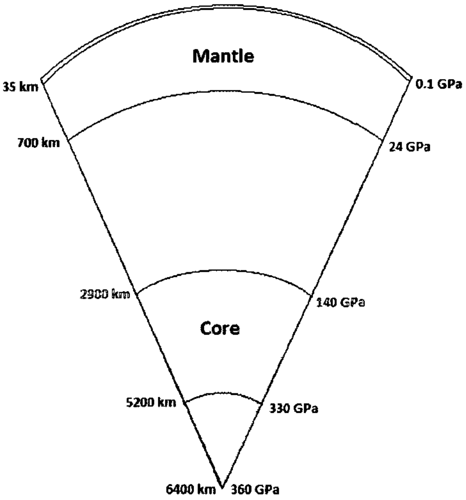

Figure 1.3 – Schematic diagram of the interior of the Earth. 360 GPa of pressure separates the conditions on the surface to those of the inner core [13].

Still greater pressures can be found in the solar system. The core of Jupiter, the most massive planet in our solar system, is estimated to have a core pressure as high as 4500 GPa [14]. The motivations for research at these extreme conditions are plentiful. If one can simulate the pressure and temperature conditions of a planetary body in the lab, then one can study natural phenomenon unique to certain environments and how they evolve. Methane hydrate, for example, is a substance thought to have been dominant in the nebula from which Saturn, Uranus, Neptune, and their major moons formed [15]. A study done by Loveday *et al.* [10] determined that on Titan, Saturn's largest moon, storage of this hydrate in previously unknown high-density phases at pressures above 3 GPa and the gradual release of it over the course of its evolution allowed it to exist today in significant quantities instead of dissociating into its constituents. Jupiter is thought to contain liquid hydrogen at a depth where large pressure and high temperature prevail: 140 GPa and 4000 K [16]. In the interior of our own planet Earth, many interesting phenomena exist at extreme conditions. Magma convection currents deep in the Earth's mantle are the driving forces behind continental drift. Whether or not currents flow is determined by plasticity, ductility, temperature, pressure, and other factors that affect the material deposits in the mantle; all of which are still subjects of debate [17]. Studying the materials present at those conditions is therefore important to understand how convection currents work. The work in this thesis focuses on crystalline structures that form below the 5 GPa pressure range and sub-ambient temperature. This pressure range, although quite modest, has produced interesting results on our system of study.

1.2 - Generating high static pressure: the diamond anvil cell

While it is interesting to some extent to theorize as to what should occur to certain materials subjected to extreme pressures, it is necessary to actually achieve them in the laboratory and perform experiments under those conditions. The field of high pressure research began in the early 1900s with the extraordinary work of a single individual. Back then, methods of generating high pressures involved the use of large volume presses capable of generating pressures on the order of megapascals. After receiving his PhD in Physics in 1908 from Harvard University, Percy Williams Bridgman went on to revolutionize the field of high pressure research by introducing a hydraulic, ram-driven, piston-cylinder design press. At the center of this device were two opposing anvils made of tungsten carbide (WC):

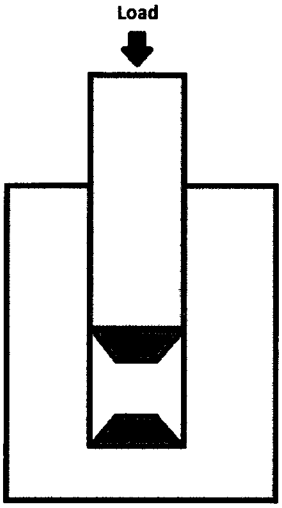

Figure 1.4 – Schematic diagram of a Bridgman high pressure cell. Two tungsten-carbide anvils were forced together by a large hydraulic press. Pressures achieved were as high as 10 GPa.

The fact that tungsten carbide was stronger than many available materials at that time, even hardened steel, made it an ideal choice for a compression device. After years of refinement, Bridgman's high-pressure devices eventually managed to generate pressures exceeding 10 GPa, two orders of magnitude greater than that achieved by earlier devices [18]. Using this apparatus, Bridgman made countless contributions to field of high pressure research, including the discovery of new phases in many different systems, the measurements of isothermal compressibility, electrical and thermal conductivity, viscosity, and tensile strength of hundreds of different compounds, eventually earning a Nobel Prize in Physics in 1946 for his work [19].

The sheer size of the hydraulic presses used by Bridgman, and difficulty of use were perhaps one reason why not too many experimentalists pursued high pressure research beyond Bridgman's achievements. In addition, the apparatus design limited the types of viable experiments possible. This all changed in 1958 when the first diamond anvil cell (DAC) was invented by Charles E. Weir, Ellis R. Lippincott, Alvin Van Valkenburg, and Elmer N. Bunting of the National Bureau of Standards (NBS) [6] (see Figure 1.5).

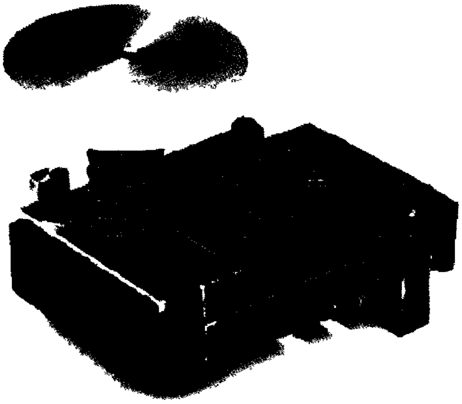

Figure 1.5 – The first diamond anvil cell, created by Charles E. Weir and colleagues of the National Bureau of Standards in 1958. This photo is a contribution of the National Institute of Standards and Technology.

To date, many different modifications to the DAC have been implemented, depending on the different experimental needs of individual labs, however the basic core design remains the same (see Figure 1.6).

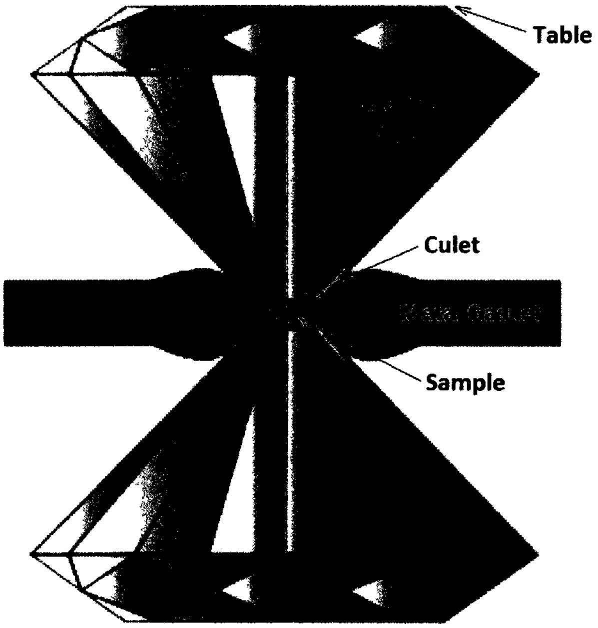

Figure 1.6 – The diamond anvil cell. Two opposing diamonds and a metal gasket with a hole drilled into it form a compression chamber for high pressure study of a sample. [21]

The core of the DAC consists of two opposing, gem-quality, brilliant cut diamonds. Each diamond's tip is cut and polished to form a small flat surface called the culet. The material to be studied is placed in between the two diamond anvils and the culets are driven together by an appropriate mechanism. The genius of the original NBS DAC design, which can be seen as a miniature Bridgman cell, was that the opposing diamond anvils were not driven together by pressing axially against the two diamond tables with a press, but rather by using a screw to operate a lever-arm which in turn distributed the force around the sides of the table (see Figure 1.5). This left the tables unobstructed, and, importantly, the sample could be viewed through the anvils using a microscope before, during, and after compression. What made this DAC design superior to previous high pressure cells was the ability to see phase transitions by changes in sample texture and colour (see Figure 1.7 for an example), the establishment of domains at phase boundaries, and the creation of single crystals, among other abilities.

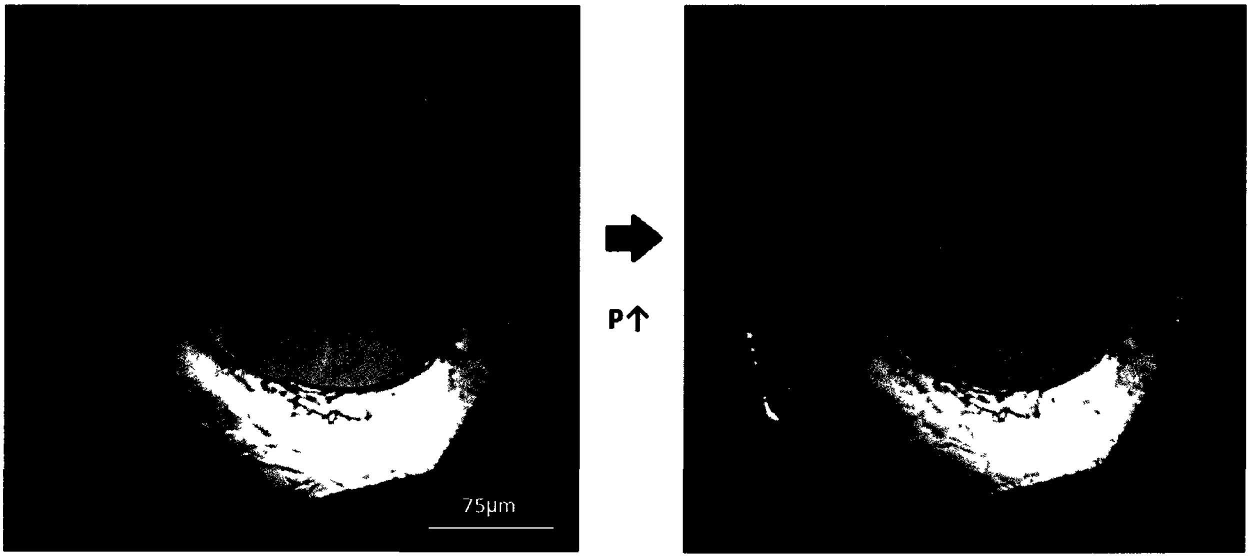

Figure 1.7 – In the above photographs taken through one anvil of the diamond anvil cell with transmitted light, pressure is applied to a sample mixture of N_2 and CH_4 which initially appears transparent. The sample suddenly gains texture as it crosses a phase boundary, visually indicating this transition. The ability to watch the sample under a microscope is thus very useful. (Pictures courtesy of Catherine Aldous, LPSD)

The choice of diamond as the anvil material was not random. First, being the strongest natural material, diamond can withstand the largest load (leading to the highest sample pressure) without breaking. Second, diamond is also mostly transparent to a wide range of probing radiation: ultra violet, visible, infrared, and x-rays. This allows a whole range of optical and scattering experiments by passing radiation through the DAC, such as Raman spectroscopy, Brillouin scattering, infrared spectroscopy, and x-ray absorption and scattering. Third, diamond is an excellent conductor of heat (actually the very best material), allowing one to measure the sample temperature from the diamond with relative accuracy. Selection of proper diamonds is important: they must be inclusion-free (free of anything that may cause a crack at high pressures), have low optical birefringence (a result of a low density of dislocations), and have a low density of chemical impurities. Diamonds are classified according to their impurity content, which most commonly involves nitrogen substitutions: types Ia, Ib, IaB, etc. Pure diamond is classified as type IIa and is the most desirable, as any impurities affect the optical and mechanical properties of the diamond. Natural type IIa diamonds are rare and costly. For the work in this thesis, type Ia diamonds with a culet diameter of 300 μm were used.

Although not in the original NBS design, the gasket is an essential part of all modern DACs; it was first introduced in 1964 by van Valkenburg [18]. In order to prevent the sample material from extruding out from between the diamond anvils during a compression sequence, a thin piece of metal with a hole drilled through it (the gasket) is placed in between the anvils.

Figure 1.8 – Gasket preparation. A 0.25mm thick steel gasket is placed between the diamond anvils (left). Next, pressure is applied to indent the gasket to the desired thickness (middle). Finally, a hole is drilled through the indentation (right).

The combination of the anvil culets and metal gasket walls create a sealed compression chamber in which the sample under pressure is contained (see Figure 1.6). The gasket is first prepared by selecting a piece of hard, yet ductile metal and indenting it with the diamond anvils by placing it carefully between them and then driving the anvils into it. By watching under a microscope, the extrusion of metal by the anvils can be observed as pressure is increased, and the width of this extrusion can be used to gauge the thickness of the remaining material in between the anvils (the eventual thickness of the compression chamber). Typically, an initial gasket thickness of 250 μm is reduced below 100 μm as a result of the indentation.

The choice of gasket material is also important. For pressures below 50 GPa, fully hardened stainless steel (ANSI T301) is commonly used, however higher pressures require stronger materials such as rhenium. After indentation is completed, a hole is drilled in the center of the indentation using specially made tungsten carbide precision drill bits with diameters varying from 75 to 200 μm. In addition to containing the sample, the gasket also serves the purpose of preventing the anvils from coming into contact with each other. Users of early DACs quickly discovered that, as hard as they might be, diamonds were not indestructible when put up against themselves. Stress-induced chips and faults could eventually lead to diamond failure (see Figure 1.9). By taking proper care to align the anvils and by using a gasket, this can be minimized.

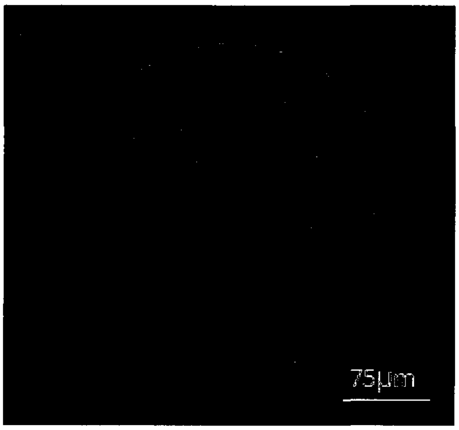

Figure 1.9 - Under a microscope the culet of a 16-faceted anvil shows signs of damage. A large subsurface fault can be seen by the darkened region near the bottom, as well as a large crack running along the culet's surface. (Picture courtesy of Serge Desgreniers, LPSD)

Apart from these basic components, individual cell design depends on the intended purpose of experiments and sample loading requirements. The cell type used in this work was of a cylinder-piston design with a pressure membrane fitting (see Figure 1.10).

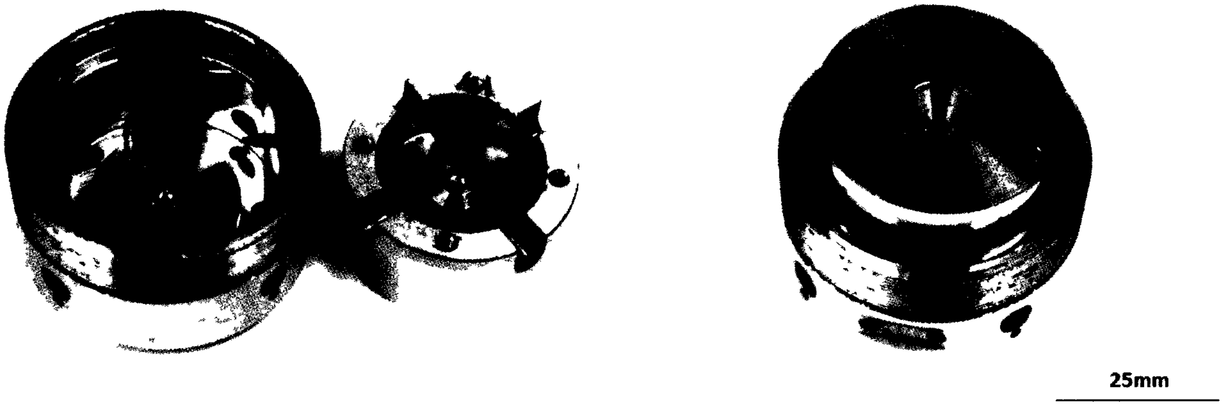

Figure 1.10 – The diamond anvil cell used in this research. The piston and cylinder sides (left) are machined to fit together precisely when assembled (right). The diamond anvils can be seen at the centers of the piston and cylinder (left).

The "membrane cell" used in this work is divided into two main parts: the piston and the cylinder. The piston consists of a cylindrically-shaped piece of machined steel approximately 45mm in diameter and 15mm in height, with a hole machined through the center of its diameter. The purpose of the hole is to provide a line of sight to the diamond anvil table. The next major component of the piston is the seat. The seat is a device used to support the anvil and transfer the applied force to its table. The seat is an important component because it must be strong enough to support the forces applied to it, while at the same time keep the anvil in its original alignment. Seats are thus usually manufactured using hardened steel or tungsten carbide.

Many experiments involving radiation scattering off the sample in a DAC (such as x-ray diffraction, to be discussed in Section 1.3) also require that the maximum scattering angle be achieved without reducing the functionality of the DAC. Because the diamond anvils themselves are transparent to many probing radiations, the limiting factor is seat material. If the seat is composed of a dense metal, then radiation scattering off the sample will be absorbed by it. For this purpose, materials such as beryllium, which is transparent to x-rays because of its low atomic number, are used instead.

On the piston of the cell used in this work, a tungsten carbide seat was used. Of course, the anvil is then placed on the seat and glued in place after a delicate alignment procedure. The cylinder side of the cell is a hollowed out piece of machined stainless steel made with dimensions to fit the piston inside of it and precision ground to within a tolerance of ~10 µm. Like the piston, the cylinder is equipped with a seat (made out of beryllium this time) and a diamond anvil.

Two more features are prevalent on the cylinder body: screw holes and threads. The membrane cell has two main ways of driving the piston into the cylinder to create pressure; manually, with the so-called "pressure screws", or with the aid of a pneumatically-driven membrane. The default way to generate pressure is to use the pressure screws. Four screw clearance holes pass through the cylinder and align with the threaded holes in the piston. When the screws are tightened slowly one by one, the piston is driven into the cylinder in a controlled way (see Figure 1.11).

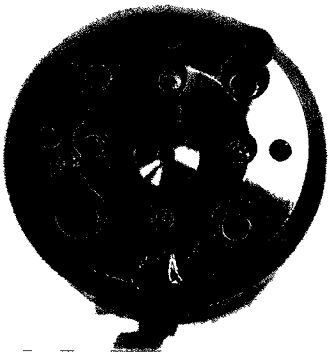

Figure 1.11 – Four pressure screws (only two are shown in this photograph) are used to pull the piston and cylinder together and generate the high pressures inside the compression chamber.

When the pressure screws cannot be used or are inconvenient, the pneumatic membrane assembly is used instead. This assembly consists of an inflatable metallic membrane held in place against the DAC piston by a metal collar which screws into the large threads on the outer edge of the cylinder. A high pressure gas capillary is connected to the membrane on one end and to a pressure controller at the other. The pressure controller consists of a system of valves and gas canisters that feed gas at high pressure through the capillary and into the membrane at a controlled flow rate, while measuring the membrane gas pressure at the same time. As the membrane inflates, it pushes down on the piston and the sample pressure is thus increased. Pneumatic membranes are used frequently in situations where the cell must be kept, for instance, in a vacuum chamber, such as in cryogenic experiments, and the screws cannot be accessed for manual pressure adjustment. The membrane is also able to achieve much smoother increasing and decreasing pressure ramps than the screws as the control of applied pressure is not subject to human error as much as the screws are. Furthermore, the use of the membrane allows for the control of the sample pressure without disturbing the DAC position in space, a major asset in many precise experiments.

It is worth introducing, at this point, the notions of hydrostatic and non-hydrostatic pressure conditions. It is not enough to be able to create high pressures in a DAC, but one must also be aware of the type of pressure conditions actually achieved. The force applied to the compression chamber is entirely along one axis (the axis of the opposing diamonds). The gasket provides radial support for the sample under load and ensures that an equal pressure is applied in all directions and not just along the axis of the load. This ensures hydrostatic pressure conditions. At the relatively low pressures used in this work (<5 GPa), hydrostatic conditions are nearly always achieved. At higher pressures, and especially for solid samples, achieving hydrostatic conditions in a compression chamber is not certain and more technically challenging. This can lead to, for instance, spectroscopic line broadening which is undesirable for structure determination and phase boundary determination. Hydrostatic pressure conditions can be maintained to higher pressures by filling the gasket with a pressure-transmitting medium such as a methanol-ethanol-water mixture (in a certain proportion), silicone oil, or compressible gases, such as argon or helium, in their liquid state. Such a medium creates a uniform compression of the sample from all sides as it does not develop substantial shear stresses. The most desirable medium is helium, as it maintains near-hydrostatic pressures above 30 GPa. Loading gaseous media into a DAC, however, requires the use of complicated high pressure gas loading systems which are not widely available.

1.3 – Introduction to pressure measurement

Achieving very high pressures, an amazing feat in itself, is useless without a way to accurately measure them during an experiment. Many techniques have been developed to either measure or estimate the sample pressure in a wide range of situations, from the minute pressures of an artificially created vacuum to the immense pressures found at the core of neutron stars. At the low end of this range (10^{-8} to 1000 Pa), Pirani or ionization gauges are frequently employed to measure gas pressures in vacuum chambers. For still higher pressures, (1 to 100 MPa), common instruments used include pressure transducers.

Aside from having low maximum pressure sensitivity, these pressure measuring methods work by bringing some type of device in direct contact with the pressure atmosphere in need of measuring. There is an upper limit to this approach, above which mechanical failure of gauge components will occur. In addition, one of the major reasons behind creating a compression chamber out of diamond is to provide the strongest possible containment vessel for the immense pressures involved. If one were able to drill through one of the anvils and install a tiny device for measuring pressure, the structural integrity of the diamonds themselves may fail in the attempt, or during a subsequent experiment. Finally, the extremely small sample volume itself (~1×10^{-15} litres) would create problems in any such attempt.

The search for a more practical pressure gauge for experiments carried out in a DAC begins with a consideration of the original definition of pressure as force divided by area. One can simply measure the applied force on the diamonds and divide it by the surface area of the diamond culets to obtain a figure, however this method has been proved to be accurate only up to 2.6 GPa [22]. A much more useful approach is to take advantage of the properties of diamond and use an "optical" technique to measure pressure. Such a pressure gauge would obviously be dependent on the particular radiation used, and would thus have to be calibrated against an absolute pressure scale. Fortunately, the non-invasive, optical technique known as the “ruby fluorescence method” was introduced by Forman *et al.* in 1972 [23] as a solution to this problem.

1.4 - The ruby fluorescence method

As mentioned previously, diamond anvils are transparent to a wide range of radiation, making spectroscopic experiments possible. In the ruby fluorescence method, one or multiple small microspheres of ruby (Al_2O_3:Cr) are placed in the DAC’s compression chamber (see Figure 1.12, left) with the sample and then illuminated by a laser, causing them to fluoresce. The fluorescence spectrum of ruby is dominated by two very strong peaks, labeled R_1 and R_2 (see Figure 1.12, right).

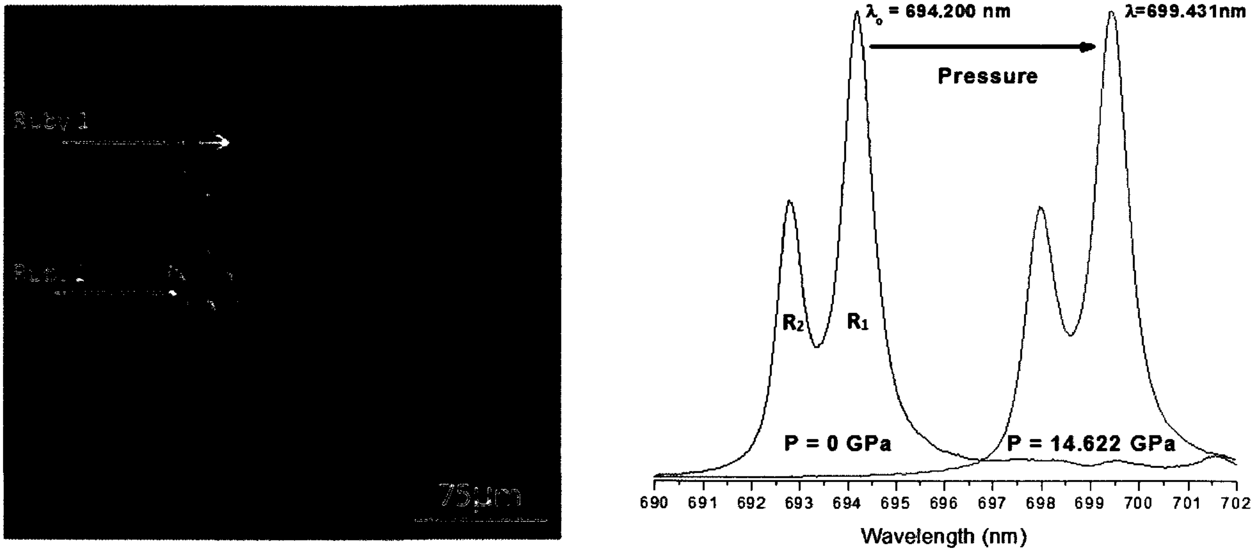

Figure 1.12 – The ruby fluorescence method. One or more ruby microspheres (~15µm in diameter) are placed in the compression chamber (left). The fluorescence spectrum from ruby is characterized by two strong peaks, R_1 and R_2, that redshift in wavelength with increasing pressure (right).

Ruby is a good candidate for pressure measurement because the spectral wavelength of the two fluorescence peaks increases almost linearly with pressure up to ~50 GPa (see Figure 1.12, right). By measuring the peak positions before and after the application of pressure, one can use a simple formula to calculate sample pressure. In 1977, Mao *et al.* published a calibration equation which has been used extensively for determining pressure by ruby fluorescence:

$$P = \frac{A}{B}\left[\left(1+\frac{\lambda}{\lambda_o}\right)^B - 1\right] \tag{9}$$

where P is pressure measured in GPa, λ is the ruby R_1 line wavelength in nm at high pressure, λ_o is the ruby R_1 line wavelength in nm at ambient pressure, A=1904, B=5 (for non-hydrostatic conditions [24]) or B=7.665 (for quasi-hydrostatic conditions [25]). The calibration was established by performing simultaneous photoluminescence of ruby and x-ray diffraction measurements of four metals all placed together in the DAC. X-ray diffraction was used to determine the unit cell volumes of each metal as a function of load, which were then used in isothermal equations of state derived from shock wave experiments and thermodynamics to find their corresponding pressures. Pressures were then correlated to the spectral shift of the ruby luminescence. Recently, in 2008, Dewaele *et al.* modified this equation with updated parameters, A=1920 and B=9.61, after performing a similar experiment in which helium was used as a hydrostatic pressure transmitting medium in the DAC [26]. This modification proved to be a better approximation to hydrostatic pressure conditions, however below 50 GPa, not much difference is noticed. Because the present work does not exceed pressures of 10 GPa, careful consideration of a high pressure scale equation is less important (see Figure 1.13).

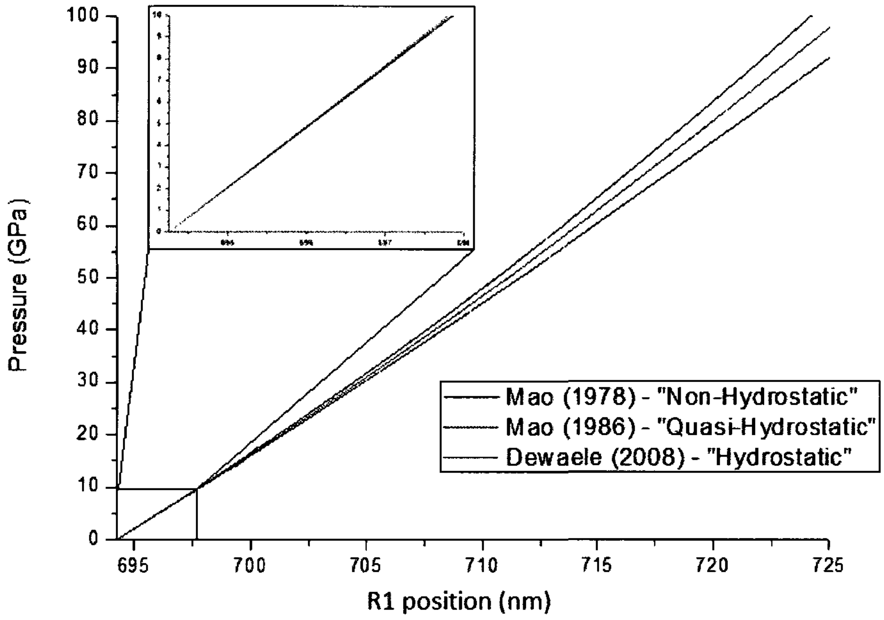

Figure 1.13 – Comparison of pressure formulae for the ruby fluorescence technique [24, 25, 26]. All calibrations are comparable below 10 GPa which is the pressure limit in this work.

When using the ruby fluorescence technique, it is important to keep in mind that pressure is not the only factor that contributes to the R-line positions. Other factors include the position of the ruby in the compression chamber, the specific chemical composition of the ruby [27], and the sample temperature. These factors can have their effects minimized or otherwise be accounted for if proper care is taken, thus providing a reliable measure of pressure.

Temperature

1.5 – Introduction to temperature

The vast majority of publications in high pressure research focus on experiments at high pressure and ambient temperature conditions. This is done because the addition of another variable in any experiment, especially a state variable such as temperature, is difficult, and in many cases, expensive to accomplish. It is prudent to explore as much as possible with one variable before moving on to another one. Once sufficient progress has been made on one front, however, it is only natural to want to expand another. As an example, consider the system that has perhaps been studied more extensively than any other: H_2O. One glance at the pressure-temperature phase diagram in Figure 1.14 will reveal a few of the multitude of phases that exist in this system.

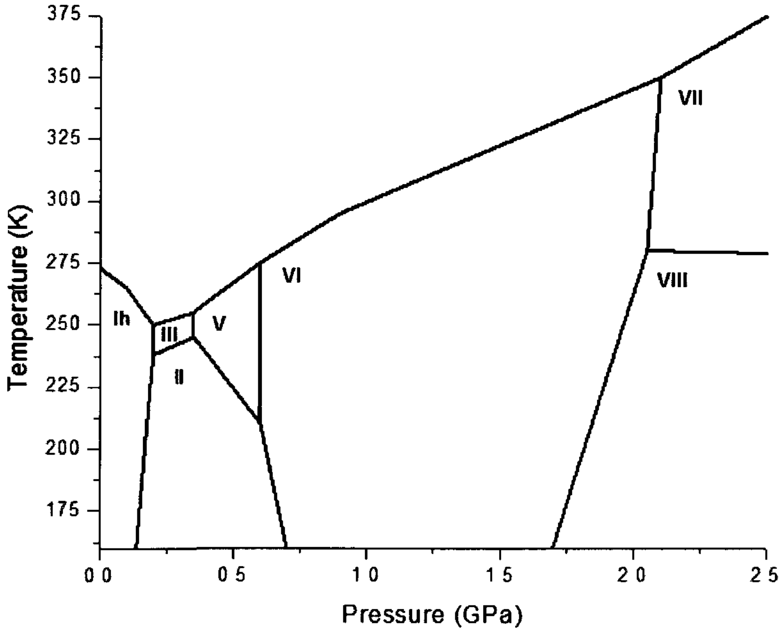

Figure 1.14 – The pressure-temperature phase diagram of H_2O [28].

H_2O is a liquid at ambient conditions (101 kPa and 300K), but adopts the hexagonal crystal structure in phase I_h that we are all familiar with just a 30 K drop in temperature. If instead of lowering the temperature, we increase the pressure to 1 GPa, H_2O will adopt a tetragonal structure known as Ice VI. At even higher pressures, it adopts a cubic structure in a phase called Ice VII. Dropping the temperature from this point by 30K we find another tetragonal structure designated as Ice VIII. If temperature was not at all explored, our knowledge of this system would be greatly reduced. The study of physical systems beyond the conditions found in everyday life is important for our understanding of the nature of matter. As previously mentioned about pressure, these widely ranging temperatures are indeed found, not so much on Earth, but elsewhere in the solar system. Studying the structure of matter at extreme temperatures is important in our understanding of geophysics, astrophysics, and other related fields.

Non-ambient temperatures in a DAC can be achieved in a variety of ways. Because the temperature range of the work in this thesis is confined to below ambient temperature, it is best to focus the discussion on cooling methods. Typically, low temperature experiments are performed using thermoelectric cooling or by using cryostats with liquid nitrogen or liquid helium. A more simplistic method was chosen for this work because extremely low temperatures were not necessary. For the diffraction experiments described in Chapter 4, the DACs were cooled to -80°C in a freezer and then brought to the beamline for quick exposure to x-rays. Because of this method, the sample temperatures during exposure ranged from 250 K to 260 K, which was acceptable for our purposes.

1.6 - Temperature measurement

Being able to control sample temperature is a challenge. Just as it was with pressure, it is necessary to be able to accurately measure the temperature. There are several options available for measuring temperature and these options can be classified into two main categories: contact and non-contact. This refers simply to whether or not the device needs to be in physical contact with the object to be measured. For the work in this thesis involving non-ambient temperatures, a thermocouple was chosen for contact temperature measurement (see Figure 1.15).

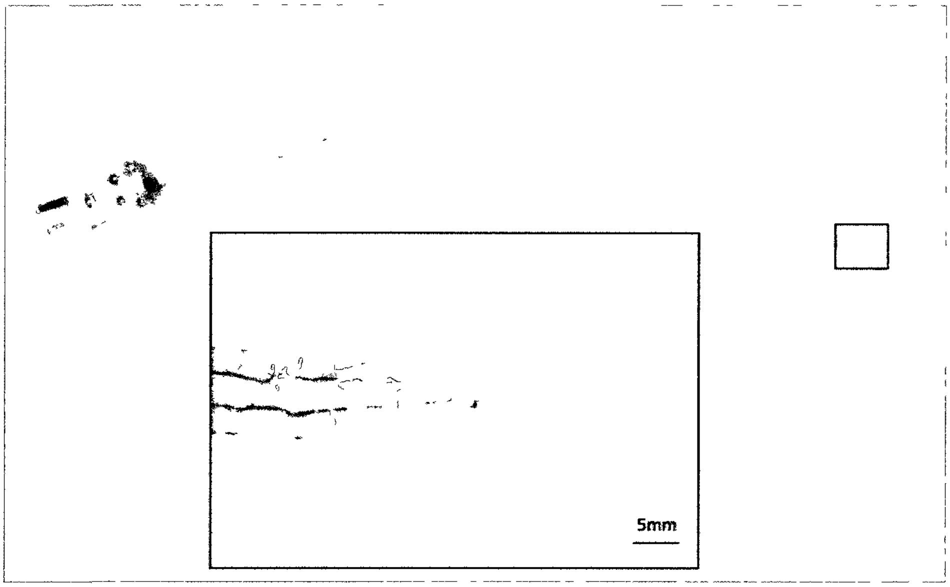

Figure 1.15 – An end welded Type K thermocouple.

The thermocouple measures temperature by taking advantage of the thermoelectric, or "Seebeck effect", a phenomenon discovered in 1821 by Thomas Johann Seebeck. A junction is created between two wires created from dissimilar metals, called the "hot junction". The remaining leads are connected to a voltmeter. The junction created by the voltmeter is referred to as the "cold junction". If the two junctions are not at the same temperature, the charge carriers (electrons or holes) will diffuse in opposite directions. This thermoelectric voltage leads to the flow of an electric current between the two junctions. The two dissimilar metals will each, depending on their composition, experience currents of different direction and magnitude. The sum of these two in the entire circuit will yield a net output voltage which is related to the temperature in a non-linear fashion and can be approximated by a polynomial specific to the types of metal used. There are seven categories of thermocouples commonly available. Depending on the temperature range required, the sensitivity of the signal required, the atmosphere of operation (some atmospheres are harmful to certain thermocouple metals) and other factors, certain thermocouples are better than others. For all experiments requiring temperature measurements in this work, a type K "Chromel-Alumel" thermocouple manufactured by Omega Engineering [29] was used. The maximum temperature range is -200°C to 1250°C with an error given by the greater of 2.2°C and 0.75% (above 0°C), or 2.2°C and 2.0% (below 0°C).

The thermocouple is attached to the cell by first passing it through an unused screw hole of ~3 mm diameter located on the rear of the cylinder, then passing tightly against the interior floor and up onto the stage where the diamond anvil is mounted (see Figure 1.16 left and middle). Because the compression chamber must remain intact, measurement using a contact device must be made by placing it right up against the diamond anvil (see Figure 1.16 right).

Figure 1.16 – A thermocouple enters the cell through an unused screw hole on the back (left), runs across the bottom of the cell (middle) and is fixed to the diamond and insulated with tape (right).

A tiny drop of thermally conducting compound is placed on the side of the anvil, and the hot junction bead of the thermocouple is pressed down into the drop and covered over with tape. The thermal compound ensures good thermal conductivity between the junction and the diamond, and thus the sample. The tape holds the junction against the anvil while at the same time providing electrical insulation to the junction from the cylinder and piston which it may otherwise come into contact with. This is important as the accuracy of temperature measurement depends on the elimination of any external contributions to the thermocouple voltage.

A final consideration in thermocouple set-up is the “cold junction”. As mentioned before, the net thermocouple voltage is equal to the difference in voltages generated across the two junctions of the thermocouple which are themselves generated by gradients in temperature. While the temperature varies at the “hot junction”, the “cold junction” temperature must be kept constant. In the experiments in this thesis, the cold junction was set at 0°C by immersing it in an ice bath. In this way, the reliability of temperature measurements was ensured.

1.7 - Temperature correction for the ruby fluorescence technique used to measure pressures

As mentioned before, temperature has an effect on the peak positions of the fluorescence spectrum of ruby (see Figure 1.17). It is critical that this be corrected for in order to be able to measure pressure correctly.

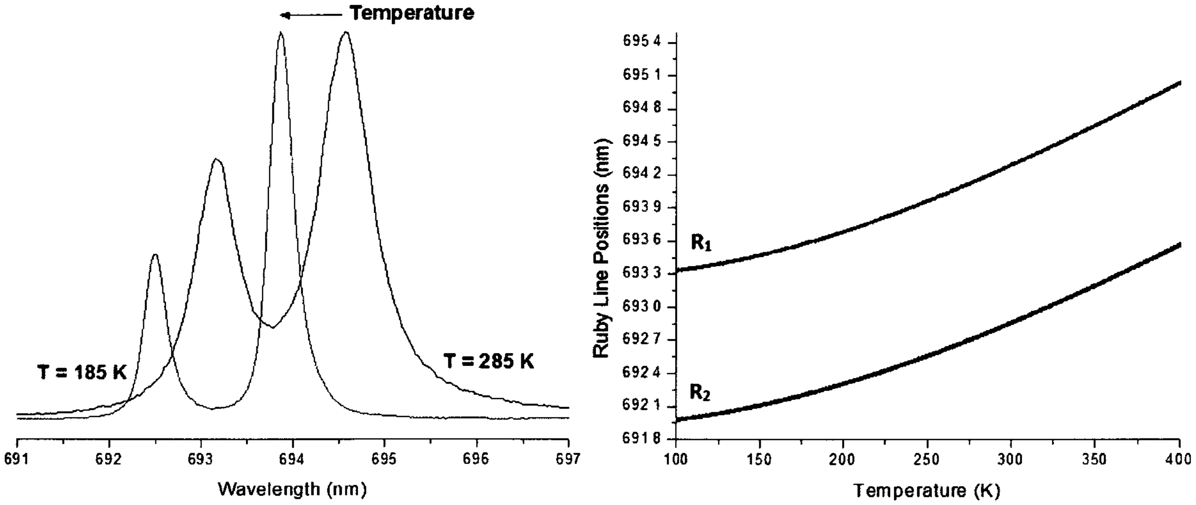

Figure 1.17 – A decrease in temperature causes the ruby fluorescence spectrum to blueshift. Because the ruby fluorescence method for calculating pressure depends on knowing the R_1 peak position before and after the application of pressure, an appropriate temperature correction must be applied.

In 1963, McCumber and Sturge [30] produced a study to address this problem by describing the shifts in terms of Raman scattering of Debye-model phonons. Under normal experimental conditions (in which temperature does not change), the reference R_1 position taken at zero pressure would also be taken at room temperature. The approach used by McCumber and Sturge is to recalculate what the R_1 position would have been had it been recorded at a different temperature:

$$\varepsilon_n(T) = \varepsilon_n(0) + \alpha_n \left(\frac{T}{T_D}\right)^4 \int_0^{T_D/T} dx \frac{x^3}{e^x - 1} \tag{10}$$

where $\varepsilon_n(T)$ is the R_1 position at temperature T, $\varepsilon_n(0)$ is the R_1 position at 0K, α_n is a fitting parameter, and T_D is the Debye temperature. For convenience this method was implemented in a spreadsheet so that the user need only input the temperature and observed R_1 position in order to retrieve the correct pressure.

In the remaining sections of Chapter 1 the main experimental methods used, powder x-ray diffraction and Raman spectroscopy, are introduced, as well as some important methods of data analysis pertaining to these methods.

Powder x-ray diffraction

1.8 - X-ray diffraction

X-ray diffraction is an experimental tool that, since its introduction in the early 1900's by W. L. Bragg and W. H. Bragg, has grown from a means to determine basic unit-cell parameters in materials, to a multi-disciplinary field capable of providing information such as cell structure, atomic positions and occupancy. Many complimentary techniques have been developed to use new types of x-ray sources, and better ways of analyzing and refining data have led to the increase in numbers of users of this tool, and the subsequent increase in obtainable information.

A brief review of diffraction theory is necessary to appreciate the work carried out in this thesis. X-rays are a form of electromagnetic radiation with a wavelength in the range of 0.01 to 10 nm. Because x-ray wavelengths are on the order of the distance between atoms in the condensed state, diffraction can arise from a solid much like visible light can diffract from an obstacle. The diffracted intensity will benefit from constructive interference only if it satisfies Bragg's Law:

$$2\mathrm{d}\sin\theta = \mathrm{n}\lambda \tag{11}$$

where *d* is the inter-atomic distance between atomic planes in a crystal, θ is the angle between the incident radiation and the planes, *n* is an integer, and *λ* is the incident x-ray wavelength. The existence and intensity of valid Bragg "reflections" depends on the crystal structure and crystal orientation with respect to the beam. Because these reflections are related to the crystal structure, collecting diffraction images on a detector and performing analysis techniques on them can assist one in determining and refining a crystalline structure. This is the goal of x-ray diffraction.

There are two types of x-ray diffraction that are commonly used: single crystal x-ray diffraction and powder x-ray diffraction (introduced in 1916 by Debye and Scherrer and independently in 1917 by Hull [31]). In single crystal x-ray diffraction, a single crystal of the sample under investigation is mounted on a goniometer (a device used to rotate a sample) and exposed to a monochromatic x-ray beam at specific crystal orientations. The result on the detector is an array of Bragg spots representing each reflection in the crystal satisfying Bragg's law, as seen in Figure 1.18.

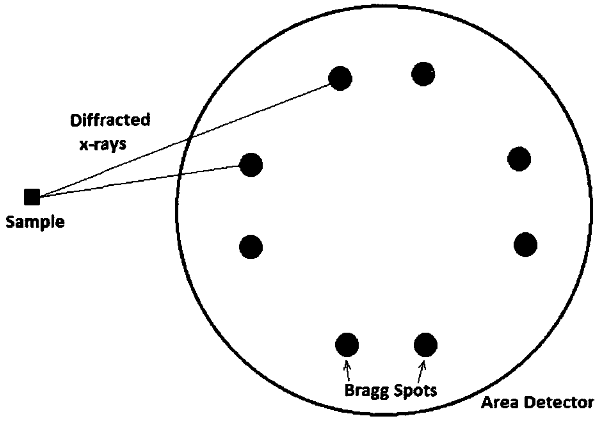

Figure 1.18 – Single crystal diffraction creates an array of Bragg spots on an area detector resulting from the crystal orientation with respect to the incident x-ray beam.

In powder x-ray diffraction, a powder consisting of crystallites of the sample is exposed to a monochromatic x-ray beam. Because of the large number of crystallites and their random orientation, every possible crystal orientation is represented. This results in diffraction cones which create Debye intensity rings on an area detector, as can be seen in Figure 1.19.

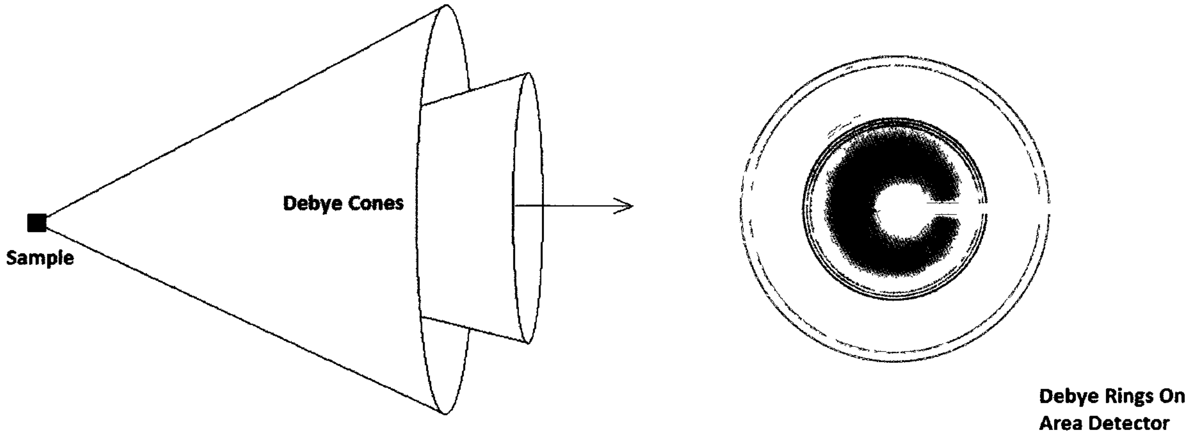

Figure 1.19 – Powder x-ray diffraction creates intensity rings on an area detector due to the random orientation of sample crystallites. The right panel gives an example of a powder diffraction image. The white part in the image is the shadow cast by the beam stop.

These Debye rings can be thought of as simply the normal Bragg spots arising from a single crystal, but distributed around in a circle due to the random orientation of the powder.

One must weigh the advantages and disadvantages when choosing between these two types of x-ray diffraction. Single crystal x-ray diffraction is the preferred method for structural determination because, not only are the reflections obvious, but the relative intensity between Bragg spots in the image are maintained, which is crucial when considering unit cell parameters such as atomic position and occupancy. In powder x-ray diffraction, because of the random orientation of the crystallites, reflection overlapping occurs, which leads to a misrepresentation of the true peak intensities. Also, obtaining a suitable powder is not always possible. A powder x-ray diffraction pattern must therefore undergo structural refinement (to be introduced shortly) in order to correct these intensities. On the other hand, it is important to be able to precisely control and know the position and orientation of the single crystal during the entire duration of a single crystal diffraction experiment otherwise the above effect will occur. This introduces obvious difficulties in sample mounting and goniometry. A powder sample requires only that the x-ray beam hit it for the pattern to emerge. Single crystal diffraction experiments run the risk of missing information if improper or incomplete rotations are performed. Peaks in the eventual x-ray diffraction pattern may be entirely missing because of such an error. This is not possible with a perfect powder sample, and one can be confident that all possible reflections will create rings on the detector. However, if one has an imperfect powder, or a powder with preferred instead of random orientation, then some peaks may be missing. One of the most limiting factors, however, is that oftentimes it is not even possible to create a single crystal of the sample in question, especially under conditions of high pressure and varying temperature. Even if one were to create a single crystal and begin a high pressure experiment, the chances of maintaining a single crystal past a phase boundary are not high.

Because of the difficulties inherent with single crystal diffraction experimental set-up and sample growth, the method chosen for this work was powder x-ray diffraction. The following sections describe the experimental set-up and the procedure used for our diffraction experiments.

1.9 - Synchrotron radiation

Perhaps the biggest disadvantage of the DAC is the available sample volume. The smaller volume facilitates the generation of enormous pressures but at the same time it makes x-ray diffraction experiments more complicated. The less material that exists for x-rays to diffract from, the more time that is required to create an equivalent x-ray diffraction image. Fortunately, this can be remedied by using an x-ray source with a higher flux. A common lab source such as a copper radiation tube produces a flux of about $1\text{x}10^8$ photons/s•mm^2 [13]. Synchrotron radiation sources, which have existed for more than 50 years now, have been growing in popularity and are now the most widely used x-ray source for studying samples in DACs. A synchrotron is a type of charged particle (in our case, electron) accelerator in which both electric and magnetic fields are used in such a way as to control and accelerate a very well confined beam. The charged particles are then confined to a storage ring for future use. Various insertion devices are installed around the perimeter of the particle storage ring such as wigglers and undulators. These insertion devices, when placed into the beam path, cause the electrons to oscillate and thus accelerate to release radiative energy, or "synchrotron radiation". Due to the use of many alternating magnetic poles in an insertion device and the magnitude of the magnetic field, the released flux can be quite high ($1x10^{13} – 1x10^{19}$ photons/s•mm^2).

The small sample volume is not the only limiting factor of the DAC; the diamond anvils themselves cause problems. A pair of diamonds 1.5 mm thick, such as those used in a DAC, will absorb 99% of all photons from a conventional copper tube source (~8 keV) [13]. Furthermore, x-ray diffraction experiments require diffracted photons to travel unimpeded to the detector. The construction of the membrane DAC allows for an angular window of ~30° (2θ) from the central axis before the cylinder or anvil seat material interferes. Reflections that scatter to higher angles will be blocked by the cell material and will not reach the detector. Synchrotron radiation remedies these two problems by its very nature. Diamonds become more transparent to higher x-ray energies. High energy x-rays, with energies above 10 keV, are known as "hard x-rays" and are easily achieved by a third-generation synchrotron radiation source. Furthermore, the wavelength of a synchrotron radiation source can be very short (~0.5 Å, corresponding to an energy of ~24.4 keV). From Bragg's Law, the use of shorter wavelengths allows crystal reflections to occur at lower angles than a normal source, thus eliminating the restricted angle problem in DAC use.

1.10 - Experimental set-up at the Canadian Light Source Hard X-ray MicroAnalysis beamline

All x-ray diffraction experiments described in this work were performed at the Canadian Light Source (CLS), a national synchrotron radiation facility located at the University of Saskatchewan, in Saskatoon, SK, Canada.

Work was performed at the Hard X-ray MicroAnalysis, (ID06) beamline (HXMA), one of several available at the facility, but the only one set up to produce the hard x-rays required for DAC research. The details of operation of the beamline itself are beyond the scope of this thesis, but a schematic diagram (Figure 1.20) and general description is warranted.

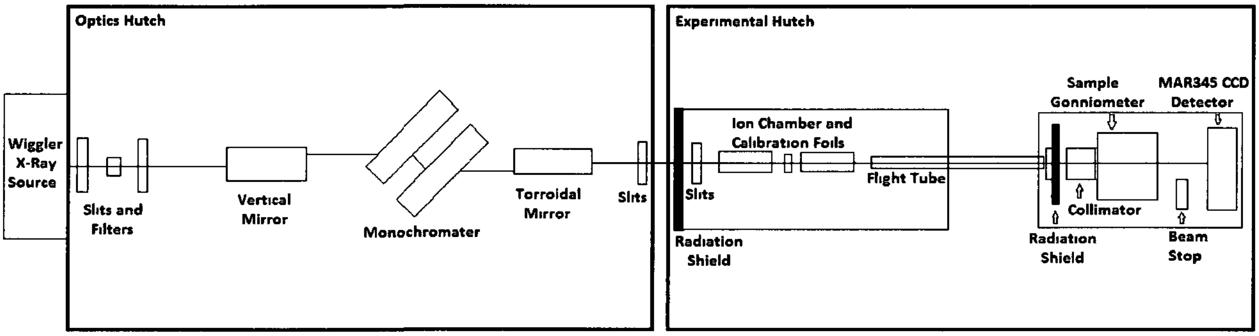

Figure 1.20 – Schematic diagram of the HXMA beamline at CLS [adopted from reference 13].

At HXMA, a 63-pole wiggler insertion device creates a source of synchrotron radiation from the storage ring which is fed through two hutches before arriving at the sample. The first hutch, the "optics hutch", contains all the permanently installed equipment necessary to create a focused monochromatic beam of x-rays. The polychromatic beam first passes through a series of slits and filters to reduce its size, after which it is directed through a monochromator by a vertical mirror. The monochromator consists of two silicon crystals cut along the (111) planes, which select out, by diffraction, all but a very narrow range of wavelengths from the incoming synchrotron radiation beam. A toroidal mirror then focuses the monochromatic beam into the second hutch, the "experimental hutch". The experimental hutch contains, in order, a radiation shield to absorb unwanted scattering from the optics hutch, slits to confine the monochromatic beam further, two ion chambers and an energy calibration foil (used in combination to measure precisely the x-ray beam energy), a flight tube containing helium to reduce scattering from air during the beam's transit through the length of the hutch, final slits and another radiation shield to protect the sample and detector. Immediately beyond this shield is a 30 μm collimator used to reduce the beam's diameter, and then a space for installing a goniometer for sample mounting. The final components beyond this are a beam stop (BS) and a MAR345 imaging plate area detector (see Figure 1.21). Upon reaching the sample position, the x-ray beam (for all experiments performed in this work) possesses an energy of 24.3500 keV, or a wavelength of 0.509176 Å, and a diameter of 30 μm.

Figure 1.21 – Upstream components used for high pressure x-ray diffraction at the CLS HXMA beamline. He flight tube (1), collimator assembly (2), sample (3), beamstop (4), and MAR345 imaging plate area detector (5).

The goniometer consists of a collection of motorized stages, on top of which the sample mount is fixed. The stages allow one to control the sample position in the beam using a series of computer macros at a station located outside of the experimental hutch [32].

All components up to the final radiation shield are pre-installed by beamline scientists prior to our arrival. Our installation begins by sliding the MAR345 detector, which is mounted on rails, into place at the end of the beam path. Next, the elevation of the beam itself with respect to the detector must be aligned by first finding the beam position, and then raising or lowering the optical table holding the detector. This is done with the assistance of "burn" paper, a specialized paper that changes colour when exposed to x-rays. Next, the goniometer is assembled in its position and its motorized stages are tested. Once this is completed, the beam stop is placed in its approximate position in front of the detector. The beam stop is a small bullet-shaped piece of brass containing a Si PIN diode for measuring the direct beam intensity, and then packed with lead to stop the beam from directly reaching the detector, as this can be damaging. The beam stop is then centered on the beam axis by using its motorized stages. The next component to be installed is the collimator assembly. First, a blank collimator with a large aperture used for rough positioning is placed in front of the radiation shield in the path of the beam. The collimator's motorized stages are operated from outside the hutch and made to scan the beam across the collimator in each direction. By monitoring the counts recorded in the beam stop diode, the exact center position for the collimator can be achieved. The blank collimator is then replaced with the real one (diameter 30 µm) and the process is repeated. This final collimator is necessary when we remember than the sample diameter, dictated by the drilled hole in the gasket, is approximately 100 µm. If the beam were too large then diffraction would not be restricted to the sample volume, but also to the surrounding gasket material. Even with a 30 µm collimated beam, some gasket diffraction lines appear in the final image. This has recently been remedied by the introduction of a "beam clean-up" aperture in front of the collimator with a diameter of 60 µm (see Figure 1.22).

Figure 1.22 – With an x-ray beam diameter comparable to the sample diameter, diffraction off the metal gasket results (left). Broad gasket rings often obscure sample Debye rings making structural determination difficult. The use of a 60 µm diameter clean-up aperture aligned close to the sample eliminates this problem caused by the gasket. Clearer sample Debye rings arising from the sample only can now be seen (right).

After the setup is complete, no further adjustments need to be made to the detector, the beam stop, or the collimator positions. The sample is then mounted atop the goniometer and a similar centering procedure is performed until the maximum counts on the diode are recorded. Once this is completed the detector can be erased and a diffraction image can be recorded.

1.11 - Taking a calibration standard

In the analysis of powder x-ray diffraction images, the 2D image is first processed by integrating all intensity at a given deflection/Bragg angle. This process produces a 1D x-ray diffraction pattern as shown in Figure 1.23.

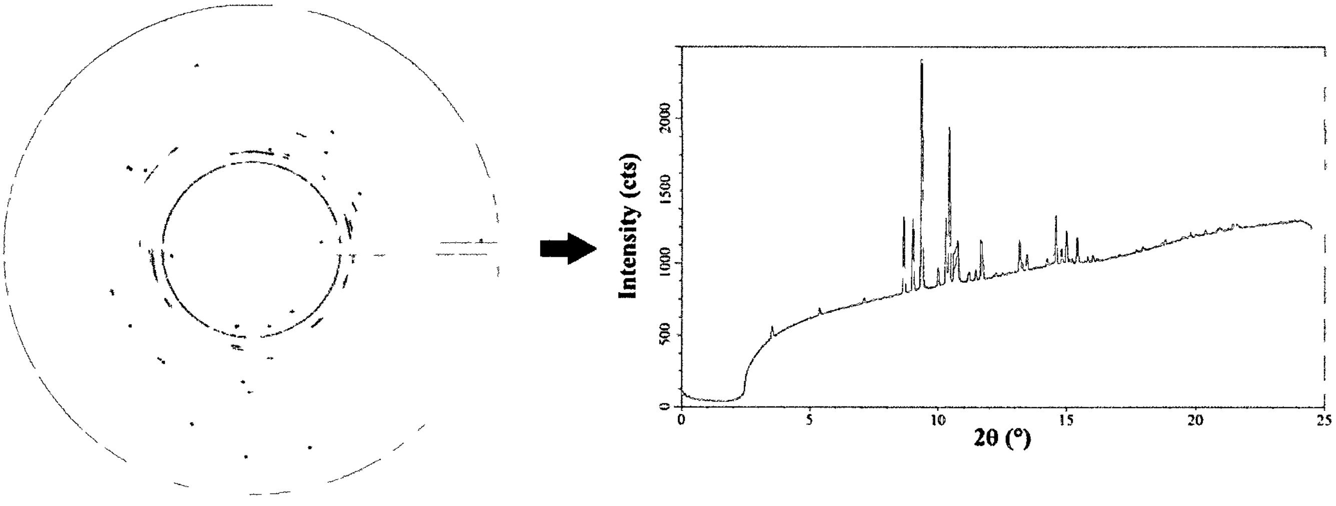

Figure 1.23 – A 2D x-ray diffraction image is integrated to get a 1D x-ray diffraction pattern.

The 1D pattern is then processed by either unit cell indexing or full pattern Rietveld refinement (details in section 1.14) to obtain the crystal structure. In order to be able to perform this integration, however, the geometry of the experiment, as well as other information is required, such as the distance from the sample to the detector, the position of the detector with respect to the beam, the angle of the detector, and the x-ray wavelength. To obtain this information, an image of a calibration standard is recorded and integrated. Using known parameters of the standard, computer software can be used to extract the missing information. Provided that the detector, beam stop, and collimator are not moved after the standard is taken, these parameters can be used to integrate the images taken of all the samples during the experimental run (of course, other factors such as tripping of the beam cause minor changes which may affect the experiment so in practice a standard is taken at least every 8 hours).

The standard used for calibration in this work was lanthanum hexaboride (LaB_6). As certified by the National Institute of Standards & Technology (NIST), Standard Reference Material 660a, lanthanum hexaboride powder, has a cubic unit cell with a lattice parameter of (0.41569162 ± 0.00000097) nm at a temperature of 22.5°C [33]. A cubic standard is a good choice because it has high symmetry which produces a strong pattern with well defined peaks, as seen in Figure 1.24.

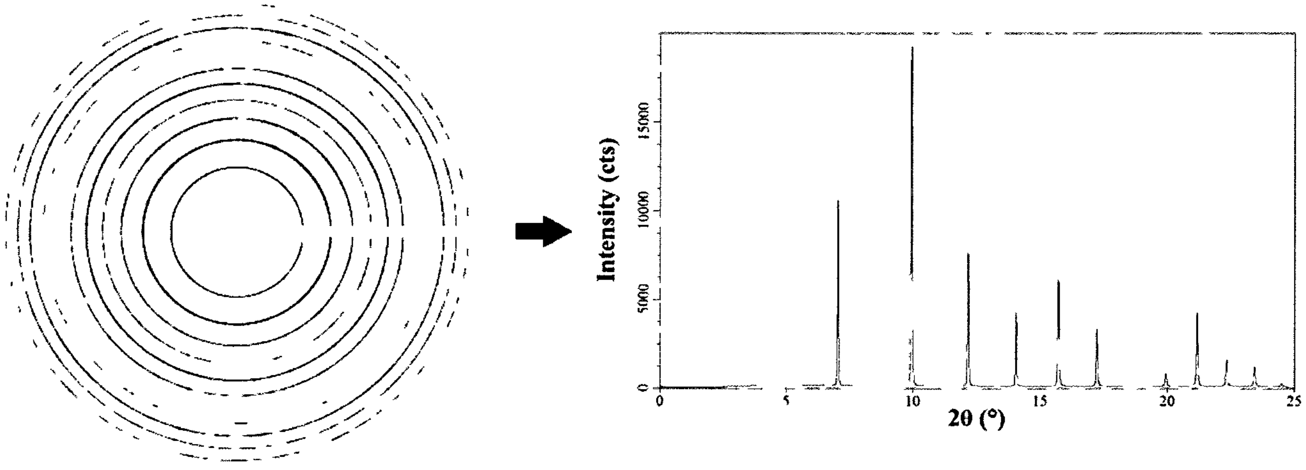

Figure 1.24 – A cubic calibration standard like lanthanum hexaboride (NIST SRM 660a) [33] is chosen because it produces a strong high symmetry pattern.

1.12 – X-ray image processing of the standard

Once a calibration image is taken of the standard, software is used to analyze it. The software package used in this work for integrating MAR345 images is called Fit2D [34]. Pattern integration of the standard begins by defining a beam center position. If the beam center position is not obvious on the image, which is the case in this work because the beam stop blocks all direct photons, it must be determined by an alternate method. In Fit2D, the beam center can be extrapolated by selecting at least 3 points on a Debye ring on the calibration pattern. A graphical interface allows the user to click on these points manually after observing the pattern. The second thing that must be determined is the rotation and tilt of the detector. Despite careful installation of the experimental setup, small errors in the rotation and tilt of the detector with respect to the beam path always exist. These parameters can be calculated in Fit2D by selecting points on other Debye rings in the pattern, then instructing the software to perform a least squares fit of the rings to elliptical coordinates. Finally, the sample to detector distance is required to complete the geometrical description of the experiment. The sample to detector distance is calculated by Fit2D for each observed Debye ring and refined by using the experimental geometry shown in Figure 1.25, where 2θ is the scattering angle of a given Debye ring, r is the radial distance to the ring from the beam center, and D is the sample to detector distance. These parameters are related by Equation 12.

$$2\theta = \tan^{-1}\left(\frac{r}{D}\right) \qquad (12)$$

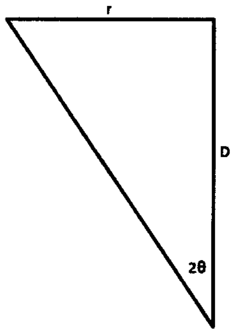

Figure 1.25 – Scattering geometry.

In other words, by knowing the radial distance on the detector of the Debye ring (which is done manually by the user in Fit2D) and the scattering angle from which it was created, the sample to detector distance can be calculated. The scattering angle is a parameter determined by modifying Bragg's Law in the following way:

$$2\theta = 2\sin^{-1}\left(\frac{\lambda}{2\mathrm{d}}\right) \tag{13}$$

where, λ is the synchrotron radiation wavelength determined through other means, and d is the interplanar spacing in the crystal which can be found for individual reflections in a cubic unit cell such as lanthanum hexaboride by the relation:

$$d_{hkl} = \frac{a}{\sqrt{h^2 + k^2 + l^2}} \tag{14}$$

where a is the lattice parameter, and h, k, and l, are the Miller indices specific to each reflection. All of this work requires only selecting the calibrant of use (the lattice parameter and expected Miller indices are programmed into the software), inputting the wavelength, and selecting several points on Debye rings on the image. The resulting calibration parameters are shown on the screen as in Figure 1.26.

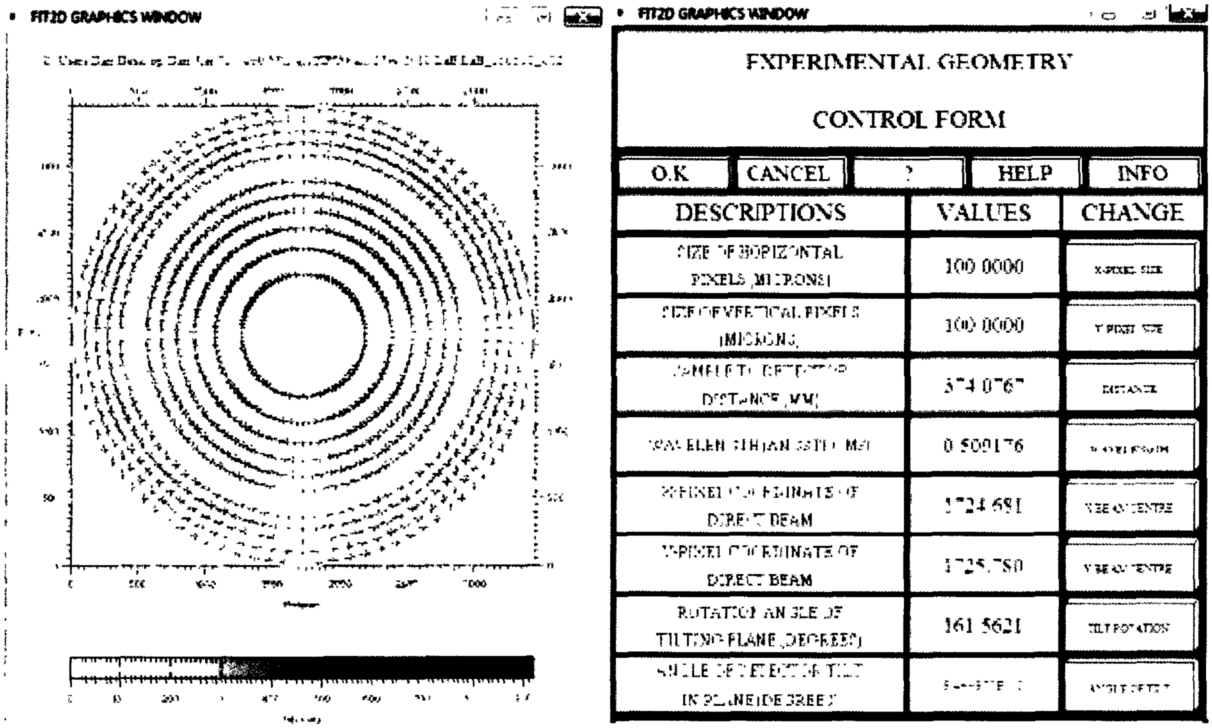

DESCRIPTIONS	VALUES	CHANGE
SIZE OF HORIZONTAL PIXELS (MICRONS)	100.0000	X-PIXEL SIZE
SIZE OF VERTICAL PIXELS (MICRONS)	100.0000	Y-PIXEL SIZE
SAMPLE TO DETECTOR DISTANCE (MM)	374.0767	DISTANCE
WAVELENGTH (ANGSTROMS)	0.500176	WAVELENGTH
X-PIXEL COORDINATE OF DIRECT BEAM	1724.691	X-BEAM CENTRE
Y-PIXEL COORDINATE OF DIRECT BEAM	1725.780	Y-BEAM CENTRE
ROTATION ANGLE OF TILTING PLANE (DEGREES)	161.5621	TILT ROTATION
ANGLE OF DETECTOR TILT IN PLANE (DEGREES)	[illegible]	ANGLE OF TILT

Figure 1.26 – Fit2D calculates the experimental configuration parameters that define the geometry of the diffraction experiment by analyzing the pattern of a calibration standard.

Using these parameters, any diffraction image taken in the same experimental configuration can be integrated by Fit2D into a 1D diffraction pattern. As a final step, the calibration pattern is exported into an indexing program called *X-ray Diffraction Analysis* (XRDA) [35] where its peaks are fit to Lorentzian functions with a linear baseline (see figure 1.27). By associating each peak with a specific *hkl* reflection, specifying the crystal symmetry, and inputting the x-ray wavelength, XRDA can use the calculated *d*-spacings to calculate the lattice parameter of the structure. If the calculated lattice parameter agrees with the theoretical lattice parameter provided by NIST, the calibration was successful.

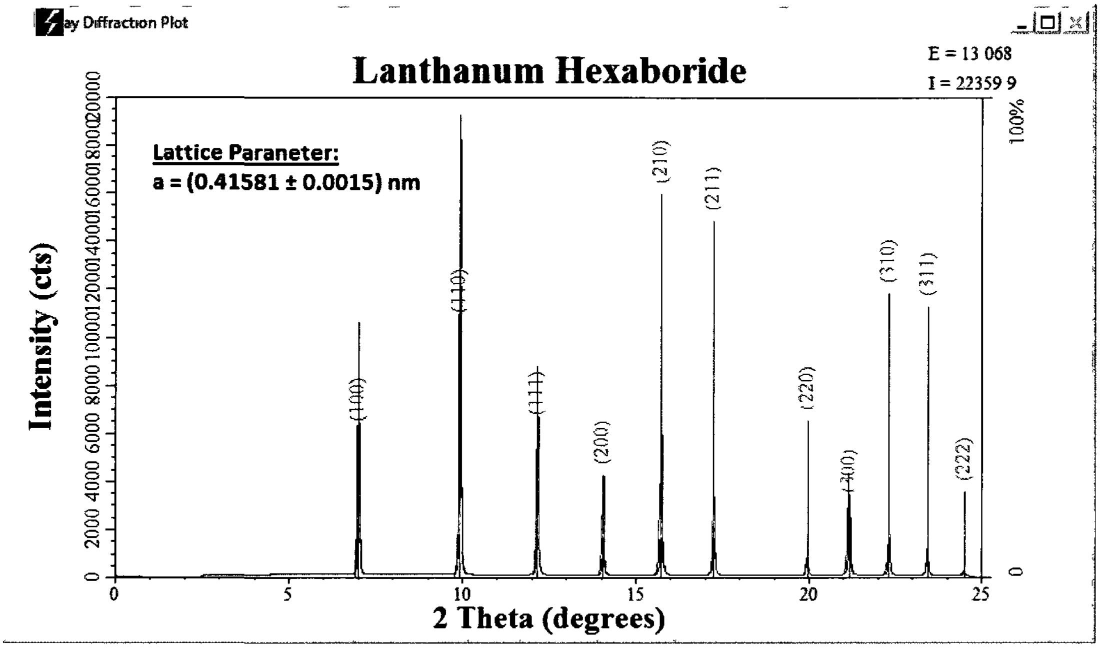

Lanthanum Hexaboride

Lattice Paraneter:
a = (0.41581 ± 0.0015) nm

E = 13 068
I = 22359 9

Figure 1.27 – The x-ray diffraction pattern of lanthanum hexaboride is fit to a cubic lattice in XRDA. The expected lattice parameter is recovered within the range of error. This indicates a successful calibration has been performed. Observed intensities do not match theoretical intensities due to the fact that they were calculated assuming single crystal diffraction.

Data Analysis

1.13 – Data analysis: unit cell indexing

The first step in data analysis is to identify any possible candidates for the structure that are expected, including any possible contaminants. The first way to do this is by examining the unintegrated image for clues. Oftentimes, the existence of more than one phase in a sample is obvious by a drastic difference in width and intensity of the Debye rings resulting from different phases. A second way the image can be useful in identifying different phases is by the appearance of spotty rings together with complete rings. This situation suggests that one phase is a good powder, creating complete Debye rings, while a second is a powder of inferior quality, creating spotty Debye rings, as in Figure 1.28.

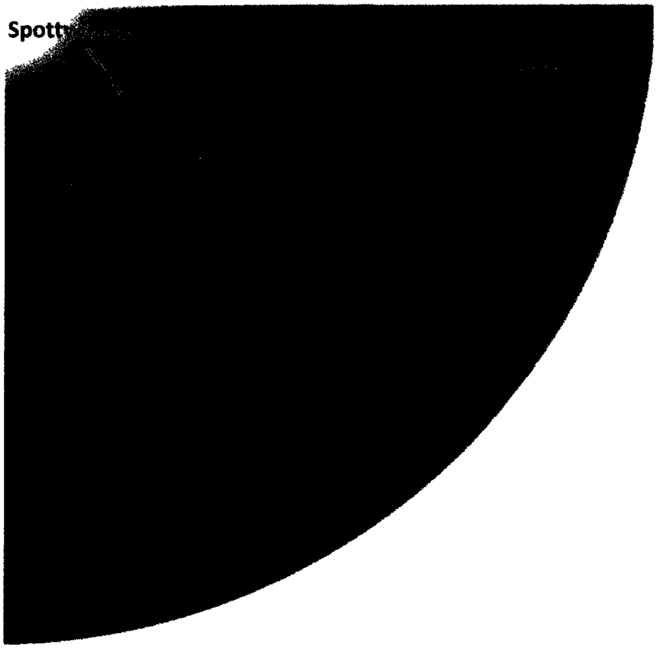

Figure 1.28 – The presence of very broad dark rings and very thin lighter rings in a diffraction image may indicate two separate phases in the sample. A similar indicator is the presence of both spotty rings and complete rings.

Once the peaks from one particular phase are identified they can be indexed in a program such as XRDA. As mentioned above, if a candidate structure is expected in the x-ray diffraction pattern and is indeed observed, this structure's peaks can be fit and assigned Miller indices. Similar to the calibration standard, a crystal symmetry is selected by the user to correspond to the inputted indices and then the program can fit the structure. The calculated lattice parameters and unit cell volume can be compared to literature values for expected candidates to verify its identity. Indexing in this manner is simple when the structures involved are expected and known, but when a new structure appears in the pattern that cannot be easily identified, another technique is required.

Solving an unknown structure from a powder diffraction pattern is a difficult problem, especially for unit cells with low Bravais symmetry. If one is left with x-ray diffraction peaks that cannot be attributed to an expected unit cell, it is possible to use them to calculate what its unit cell should be using automatic indexing programs. Software, such as the CRYSFIRE [36] suite of indexing programs, can take the x-ray wavelength and d-spacings of observed peaks as input data and compare these reflections with those expected from thousands of unit cells in a matter of seconds. CRYSFIRE outputs lists of possible unit cells in order of merit for the user to confirm manually through indexing. The problem with these software packages is that they require the input of numerous peaks (as high as 20) as a minimum to start with; any less and the accuracy of the indexing declines, especially if the Bravais symmetry of the actual unit cell is low. Furthermore, one must be sure that each peak in the input is part of the same phase; otherwise results will suffer. Oftentimes an unknown pattern does not contain enough peaks, and/or the user cannot be sure that every peak belongs to the pattern because he has not indexed it yet. Problematic as they might be, these software packages often prove to be successful.

Another technique that is useful in some cases is x-ray diffraction pattern simulation. Given the unit cell symmetry, type of atoms and their coordinates, atomic site occupancy and other parameters, one can use software packages to simulate what the expected diffraction pattern should be for a given unit cell. This proved to be very useful in this work as will be explained in Chapter 4, as a precursor to indexing of CO_2 clathrate hydrate sI. The program used in this work was PowderCell [37].

1.14 – Data analysis: Rietveld refinement

The main drawback of powder x-ray diffraction is the problem of line overlap. Any given peak in the x-ray diffraction pattern can be the sum of more than one reflection which leads to errors in the resulting peak intensities. Because the intensities are crucial to the structure factor of the unit cell, this poses a problem in structure determination. Analysis of single crystal diffraction patterns simply involves fitting the expected profile to the recorded diffraction pattern. This is not possible for powder diffraction patterns due to the mismatch in peak intensities. Fortunately, in the 1960s, Rietveld introduced a powerful method of refining crystal structures from powder x-ray diffraction data [38].

Instead of measuring the integrated intensities, the Rietveld refinement method records the entire powder diffraction pattern as a set of observed intensities per step in 2θ and then compares this to an equivalent set of calculated intensities per step in 2θ. The calculation takes into consideration unit cell lattice parameters, atomic positions and occupancy, background intensity, peak shapes and thermal parameters. The user must first start with a reasonably close structure and input all necessary data into a Rietveld refinement software package. The software then refines the structural parameters by a minimization method until the calculated x-ray diffraction pattern best matches the observed pattern. This is usually done one parameter at a time with careful supervision by the user to avoid the software falling into false minima (with possible results that do not make physical sense). Provided that the starting structure was chosen correctly, the patterns will converge and the structural information of the sample is obtained. All refinement done in this work was done in a software package called FullProf [39].

Complimentary experimental methods

1.15 – Raman spectroscopy

Raman spectroscopy gives information on the vibrational modes of a crystal lattice. When a crystal lattice is illuminated by visible light, the introduced energy is translated into vibrations that can be described as "modes" specific to the specific lattice structure. Many different vibrational modes can exist in a solid such as stretching modes, rotational modes, and bending modes. Not all of the modes of a given crystal can be excited by any given wavelength (such as the 532 nm frequency-doubled YAG laser used in this work), but those that can are said to be "Raman active". Excitation of Raman modes not excited by 532 nm light require the use of different excitation wavelengths. In Raman spectroscopy, a visible light laser is focused onto a sample crystal, exciting its Raman active modes. The incident photons either gain or lose energy producing anti-Stokes or Stokes scattering, respectively. The scattered light is collected and fed into a spectrograph, producing a Raman spectrum. The more energy a photon gains or loses during scattering, the farther it will be from the laser line on the Raman spectrum. Using different laser excitation wavelengths will result in different scattered energies, therefore Raman spectra are commonly presented in units of cm^{-1} with respect to the laser line to facilitate comparison to the work of others. Examples of Raman spectra are given in Figure 1.29.

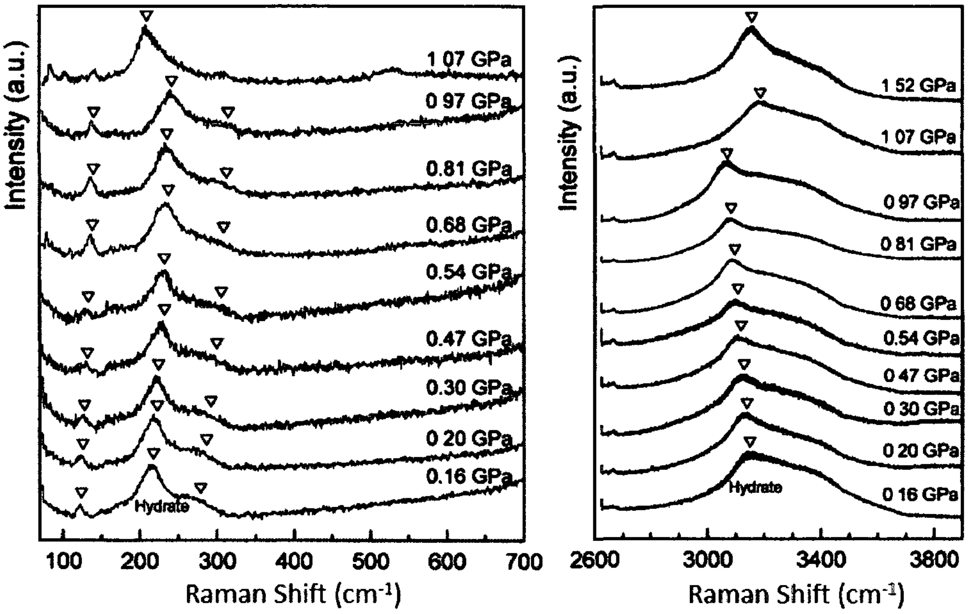

Figure 1.29 – Raman spectra of Argon clathrate hydrate plotted with increasing pressure. The left panel shows the structural lattice modes, while the right panel shows the OH stretching modes of the hydrate. A structural phase transition is characterized in a Raman spectrum by a sudden shift, disappearance, or appearance of vibrational modes as is the case here at ~1.00 GPa. (Figure taken from Shimizu et al. [40])

In high pressure research, Raman spectroscopy is commonly used as a technique complimentary to x-ray diffraction, which is also true in the case of the present work on clathrate hydrates. This technique is used for several reasons. The first is to verify that the desired sample had been loaded in the DAC. As will be explained in the next chapter, a successful loading of the hydrate sample into the DAC is not a certainty, and even if loading was successful, there is no immediate visual way to know if that sample is indeed the desired hydrate, or a phase separation of its constituents. For this purpose, Raman spectroscopy can be used immediately after loading to verify if the vibrational modes characteristic of the constituent ingredients H_2O and CO_2 are present in the DAC, and if they are present in sufficient amounts (by the strength of the signal) to warrant experimentation. The Raman signature of the CO_2 molecule in the hydrate is, unfortunately, too close to that of its pure form that it cannot be distinguished by a single spectrum. If, however, the signal is strong enough, a high pressure experiment can be performed, where Raman spectra of the sample are recorded of the sample at increasing pressure.

This leads to the second use of Raman spectroscopy in this work. Because a structural phase transition changes the lattice structure of a material, the vibrational modes will also be changed. The creation or destruction of bonds in a new structure will cause old modes to disappear and new modes to appear in its Raman spectrum. By collecting Raman spectra of a sample over ranges of pressure and temperature, one can pinpoint exactly where a phase transition occurs, however x-ray diffraction is still required to identify the nature of those transitions.

This method is complimentary to x-ray diffraction because, while it does not give the detailed information about the new structure, it can be performed in almost any lab where synchrotron radiation does not exist (note: at CLS, one can also carry out Raman spectroscopy in addition to x-ray diffraction). The exact boundaries of the phase diagram of a system can be explored in detail, needing diffraction only to identify the actual structures.

1.16 – Summary

Now that a thorough introduction to research at extreme conditions has been presented it is worth summarizing this information and how it was used in pursuit of the results presented in the following chapters.

The bulk of high pressure research focuses on identification of new structural phase transitions in materials and determination of the exact nature of those structures. The defining apparatus in this field is the diamond anvil cell which is able to exert gigapascals of pressure onto a material. This enormous pressure often has the effect of causing the material to transform its structure into some new high-density phase. By performing diffraction experiments on a material at these conditions using synchrotron radiation, and by performing subsequent data analysis (pattern indexing and Rietveld refinement), the structural parameters of these new phases can be determined.

A complimentary method to x-ray diffraction, Raman spectroscopy, is another common tool used in high pressure research. Raman spectroscopy is useful for identifying the exact boundaries between structural phases, a task not well suited to x-ray diffraction.

The following chapters describe work carried out on high pressure phases and structural phase transitions in CO_2 clathrate hydrate. After defining CO_2 clathrate hydrates and describing their synthesis, x-ray diffraction experiments performed on the sample to verify the successful synthesis of the compound and comparison to literature are presented. Next, it will be shown through the use of x-ray diffraction and Rietveld refinement that a new, previously unobserved, structural phase exists for the CO_2-H_2O system at high pressure.

Chapter 2 - Gas clathrate hydrates

2.1 - Gas clathrate hydrates

After establishing chlorine as an element in 1810, the British chemist Sir Humphrey Davy began work on a substance called "oxymuriatic acid" (HCl solution) and made a notable discovery. He found that when brought to low temperatures, rather than separate into solid ice and gaseous chlorine (at 0°C), oxymuriatic acid froze into one solid phase at a temperature higher than the ice point of water [11]. Unbeknownst to him, he had just discovered the first gas clathrate hydrate.

Gas clathrate hydrates are inclusion compounds consisting of polyhedral cages formed by hydrogen-bonded water molecules in which free gas molecules or atoms are trapped. Perhaps the most interesting fact about these compounds is that the only bonding between the guest gas molecules and host cages are van der Waal dispersion forces. As a result of this, gas clathrate hydrates exhibit non-stoichiometry (the inability to assign a formula to the substance) despite assuming regular lattice structures. For the first century since their discovery, however, their study was mostly of academic interest since no practical use could be found for them. Studies consisted of forming hydrates with different guest species and attempting to extend their known dissociation boundaries and determine chemical formulae. Due to the issue of non-stoichiometry, many "revisions" of hydrate formulae were made over the years by different experimentalists in attempts to determine their structures. (Note: In this thesis the term "dissociate" refers to the pressure or temperature induced separation of a hydrate into its constituent pure phases, and not any type of molecular dissociation).

Modern research in gas clathrate hydrates began in 1934 when Hammerschmidt discovered that blockages in high pressure natural gas transmission lines were being caused by the formation of these gas hydrates [41]. The high pressure and low temperature of these lines created the ideal environment for hydrate formation, and, because this caused problems for the natural gas industry, the study of gas clathrate hydrates was no longer simply an academic curiosity. Much work (funded by the American Gas Association) was done to find ways of dissociating the hydrates or preventing their formation in fuel lines, but even still their structures remained elusive until the 1950's when Stackelberg and Müller culminated two decades of x-ray diffraction studies on hydrates to come up with two commonly found hydrate crystal structures, namely, structures I and II (sI and sII) [42]. Together with the discovery of an hexagonal structure (sH) hydrate by Ripmeester *et al.* in 1987 [43], this ended the longstanding confusion of hydrate structures, but the problem with stoichiometry, a topic very relevant to this work, still remained.

2.2 – Hydrate structures

The first of the three main hydrate structures, sI hydrate, has a body-centered cubic unit cell consisting of two types of polyhedral cages formed by the H_2O molecules. The smaller of these cages has a dodecahedral structure while the larger is a tetrakaidecahedron. In 1984, Jeffrey [44] suggested a nomenclature system for these polyhedra: n^m where n is the number of edges in a face type and m is the number of instances of that face type. For example, the smaller cage in sI hydrate is labeled 5^{12} because it consists of 12 5-sided faces, thus making it a pentagonal dodecahedron. The larger cage is labeled $5^{12}6^2$ because it consists of 12 5-sided faces and 2 6-sided faces. Each unit cell in sI hydrate consists of 2 small 5^{12} cages and 6 large $5^{12}6^2$ cages.

The second main hydrate structure, sII hydrate, has a diamond shaped cubic unit cell also consisting of two types of polyhedra. Like the sI hydrate, the small cage has a 5^{12} structure, while the larger cage is in this case a hexakaidecahedron ($5^{12}6^4$). The unit cell of a sII hydrate has 16 small 5^{12} and 8 large $5^{12}6^4$ cages altogether. The third and most recently discovered clathrate hydrate structure is sH hydrate. This hydrate has a hexagonal unit cell containing three different polyhedra; a dodecahedron (5^{12}), an irregular dodecahedron ($4^35^66^3$), and an icosahedron ($5^{12}6^8$). The three structures can be seen in Figure 2.1.

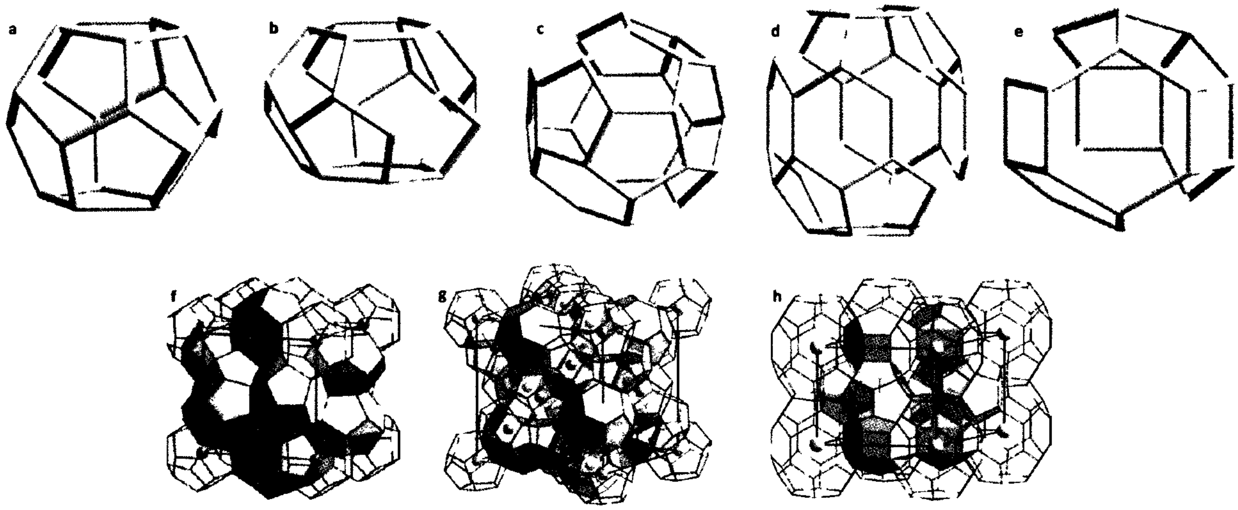

Figure 2.1 – Cage polyhedra: a) pentagonal dodecahedron (5^{12}), b) tetrakaidecahedron ($5^{12}6^2$), c) hexakaidecahedron ($5^{12}6^4$), d) irregular dodecahedron ($4^35^66^3$), and icosahedron ($5^{12}6^8$). Gas clathrate hydrate structures f) cubic structure I, g) cubic structure II, and h) hexagonal structure H. [Figures by Komarov *et al.* [45]]

Of all the hundreds of compounds that form clathrate hydrates, all adopt one of these three structures with the exceptions of bromine [46], dimethyl ether [47], and ethanol [48]. Various structural analogues exist where the cage structure is formed with something other than water. Schlenker *et al.* [49], for example, synthesized a high-silica zeolite (ZMS-39) with the exact same structure as clathrate hydrate sI, except that the H_2O is replaced with Si_2O [49], a compound referred to as a "clathrasil". Clathrate structures were also found that were formed from Group XIV elements, namely C, Ge, and Sn [50]. Studying structural analogues like these is helpful because it provides insight into solving problems involving actual gas clathrate hydrate.

Recently, a new class of structures has been discovered to exist in many clathrate systems at high pressure [51]. The clathrate hydrate structures described above all contain several types of polyhedra where the diameter of cages is much greater than the diameter of the guest molecules, leading to inefficient space filling compared with simple ice structures. In the new class of structures, called "filled ices" (FIS), the guest molecules occupy channels between the simple space-filling polyhedra of a known ice structure. The diameter of these channels is comparable to the guest diameter, and therefore a high-packing efficiency is achieved. In 2001, for example, Loveday *et al.* found that methane sH clathrate hydrate transforms into an orthorhombic FIS, seen in Figure 2.2, at 2 GPa which closely resembles Ice-I_h [5].

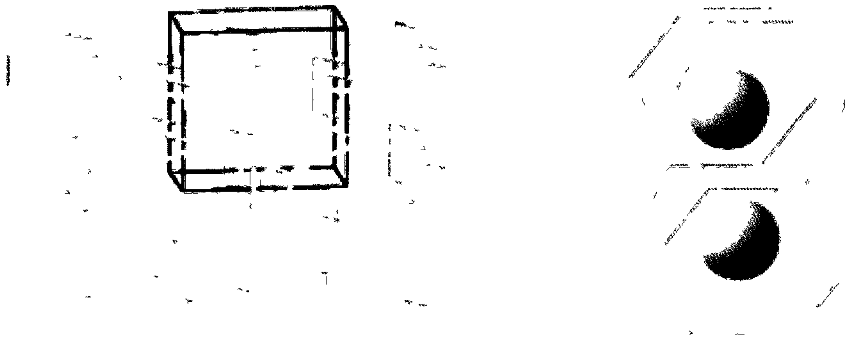

Figure 2.2 – A hexagonal lattice of H_2O molecules similar to Ice I_h (left). Gas molecules pack into channels formed between ice layers (right) in the "filled ice" structure. [Figures by Komarov *et al.* [45]].

It is important to note that the filled ice structure is not a clathrate hydrate, as it does not form cages. It will be discussed together with the clathrate hydrates because of its relevance to the upcoming work.

2.3 – Hydrate formation and bonding

The theory of gas clathrate hydrate nucleation is beyond the scope of this thesis, but a brief comment is necessary to understand how these structures arise. When water is cooled below 277 K, molecular dynamics studies[52] indicate that its molecules begin to link together with hydrogen bonds to form clusters of pentagons and hexagons, shapes that are preferred due to minimal O-O-O angle deviation from the normal 104.45° of water. Eventually, once these clusters reach a certain critical density, nucleation of the solid state begins. If dissolved gas molecules are present in the water, the hydrophobic interaction will cause an attraction between the solvent and the gas molecules. The water rings then cluster around the gas molecules and form polyhedra, and if a sufficient density of polyhedra is achieved these clusters will begin to agglomerate into clusters of polyhedra and initiate nucleation of the clathrate hydrate structures[53].

As mentioned previously, each clathrate structure is composed of more than one type of polyhedral cage. If all of its polyhedra are not present in the cluster then nucleation is inhibited. Furthermore, the stability of the polyhedra in question actually requires the inclusion of a guest gas species. A clathrate hydrate structure completely devoid of guest gas molecules or atoms is not stable[54]. The van der Waals forces between the guest and cage structure prevent its collapse. Despite this fact, not all cages in an entire clathrate structure require a guest molecule so long as the majority of them do. This has caused problems in developing stoichiometric descriptions of gas clathrate hydrates, as will be discussed shortly.

Perhaps the biggest factor in determining what hydrate structure a certain guest will form is its diameter. As a general rule, the guest must have a diameter smaller than the diameter of the cage in order to be able to fit inside, yet large enough to provide enough repulsive force to maintain the structural integrity of the cage structure. Only one gas molecule may occupy each cage, with two exceptions. The first occurs with guest gases like hydrogen and helium which are actually small enough to stabilize a clathrate structure by double occupancy. The second exception is the isocahedral $5^{12}6^{8}$ cage of the sH hydrate, which has the potential to hold up to five guest molecules.

Finally, any guest that is small enough to fit into a structure's small cage will also enter its large cage. Table 2.1 shows a comparison between the average cage diameter and the maximum guest diameter allowed for each hydrate cage.

Hydrate Structure	sI		sII		sH		
Cage	Small	Large	Small	Large	Small	Medium	Large
Description	5^{12}	$5^{12}6^{2}$	5^{12}	$5^{12}6^{4}$	5^{12}	$4^{3}5^{6}6^{3}$	$5^{12}6^{8}$
Number of Cages/Unit Cell	2	6	16	8	3	2	1
Average Cavity Diameter (Å)	7.90	8.66	7.82	9.46	7.82	8.12	11.42
Maximum Guest Diameter (Å)	4.58	6.00	4.58	6.60	4.58	4.58	8.60

Table 2.1 – Comparison of cage diameter to maximum guest diameter for gas clathrate hydrates. The guest must have a diameter smaller than the cage diameter. [Adapted from reference 53].

Table 2.1 summarizes the limits in guest diameter for each of the three hydrate structures. In addition to the general size rules for occupancy, it is not necessary that all cages in a hydrate structure be occupied by a guest gas molecule in order to stabilize the structure [53]. Structure I for example, may be stabilized by guests occupying only its large cage. This occurs for guests whose diameters are larger than the small cage diameter, but smaller than the large cage diameter such as CO_2 (5.12 Å). Structure H can only be formed when its two largest cages are occupied. This can be achieved in a pure hydrate where both cages are occupied by the same gas species, or in a mixed hydrate, where a gas molecule is larger than 4.58 Å and thus requires a second gas species to help enter the medium sized cage and thus stabilize the structure. Such gases are referred to as "help gases".

As for the FIS, it is not yet clear why this structure is commonly adopted after the clathrate hydrate structures lose stability under pressure. More modeling work is needed to explain how and why the FIS structure arises.

2.4 - Stoichiometry

As mentioned previously, the pioneers of research in gas clathrate hydrates were challenged in determining the stoichiometry of these compounds. Davy's initial discovery of chlorine hydrate in 1818 led him to propose a formula of $Cl_2 \bullet 10H_2O$; this was corroborated by Faraday in 1823 but ultimately proved incorrect. Villard proposed a general formula of $M + 6H_2O$ in 1895 (where M is the guest species) for all gas clathrate hydrates which also eventually proved unreliable [53]. These early attempts were all made by trying to directly measure the water to gas ratio in the hydrates. Unlike most solids, gas clathrate hydrate composition is variable with the temperature and pressure conditions prevailing during its period of formation. While it is possible to measure the ratio of the individual constituents after they dissociate out of the hydrate phase, this does not accurately represent the composition of the hydrate phase. Changes in temperature and pressure after the initial formation of the hydrate often cause it to occlude water in an unpredictable fashion, removing it from the hydrate mass. It is difficult to completely separate the water from the hydrate, and thus any compositional measurement will be skewed.

Even after the advent of indirect methods such as vibrational (Raman) spectroscopy and x-ray diffraction, the determination of composition and structure in gas clathrate hydrates still proved difficult. On the basis of the three established hydrate structures and their constituent polyhedra, formulae for gas clathrate hydrates are currently written down according to the number of water molecules and cages as follows: For sI hydrate, $6(5^{12}) \bullet 2(5^{12}6^{2}) \bullet 46H_2O$, for sII hydrate,

$16(5^{12})\bullet8(5^{12}6^{4})\bullet136H_2O$, and for sH hydrate $3(5^{12})\bullet2(4^{3}5^{6}6^{3})\bullet1(5^{12}6^{8})\bullet34H_2O$. Making the assumption that at most one guest can fit into each cage, except in the case of the $5^{12}6^{8}$ cage which can hold up to five, this gives ideal guest:host ratios (or "hydration ratios") of 1:5.75 for sI hydrate, 1:5.66 for sII hydrate, and 1:3.4 for sH hydrate. The problem with gas clathrate hydrate stoichiometry is, that in most cases, this ideal ratio is never achieved because it may not be necessary or possible to fill every cage of the structure with a guest [53].

The FIS seems to be more stoichiometric depending on the guest species. Calculations of the density of orthorhombic methane FIS gives a fixed 1:2 guest:water ratio and thus the formula guest$\bullet2H_2O$, as in the case of $CH_4\bullet2H_2O$, for instance [10]. Other FIS examples include tetragonal argon FIS ($2Ar\bullet6H_2O$) [55] and the orthorhombic tetrahydrofuran FIS ($THF\bullet6H_2O$) [56].

2.5 – Hydrate formation conditions

The formation of gas clathrate hydrates requires more than just having a guest with the guest diameter in presence of H_2O. Pressure and temperature conditions need to be optimal in order for clathrate hydrates to nucleate. Established dissociation curves for a few gas clathrate hydrates as a function of pressure and temperature are shown in Figure 2.3. The phase diagram of pure H_2O is overlaid with darker phase lines for reference.

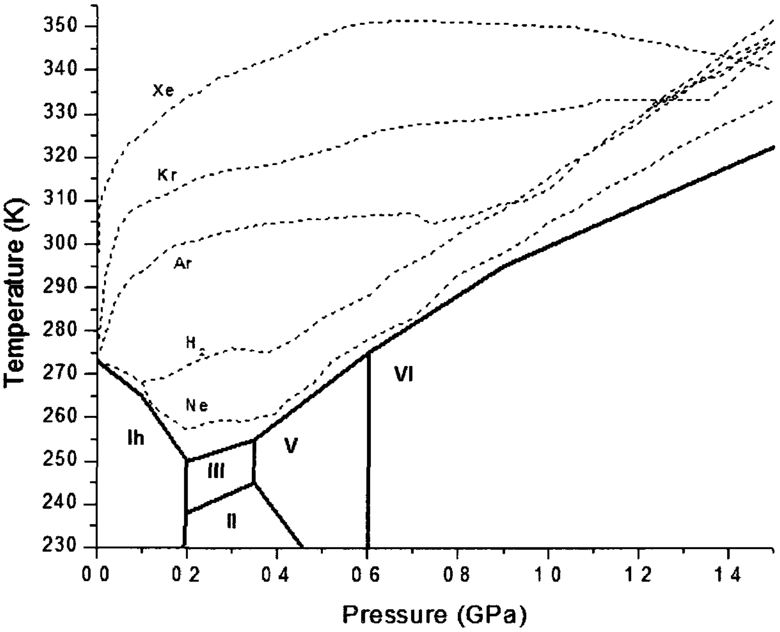

Figure 2.3 – Dissociation lines for some gas clathrate hydrates as a function of pressure and temperature. The phases of pure H_2O (dark lines) are overlaid to give perspective. [Data accumulated from various sources [57-60]]

All temperature-induced dissociation lines exist above the freezing point of water at all pressures. In general, the temperature of dissociation increases with increasing guest diameter. Looking at the examples of helium and hydrogen clathrates, the dissociation boundary follows that of water with increasing pressure, always staying a few degrees above it. The second factor critical to hydrate formation is time. Depending on the hydrate one is trying to synthesize, different pressure and temperature conditions need to be held for an extended period of time to allow constituents to mix together and form the hydrate. For xenon hydrate, for example, one must mix pure water (ice) and xenon gas in a high pressure vessel, keep pressure and temperature conditions below the dissociation line (achievable at room temperature with moderate pressures), and allow sufficient time for the gas molecules to be enclathrated by the water. This is best done with excess gas such that one can monitor the gas uptake into the ice by monitoring how much the vessel pressure decreases after loading over time. Once formed, any excess constituent material can be removed to recover a pure hydrate sample.

2.6 - Gas sequestration

The most widely cited reason for the study of gas clathrate hydrates is their ability to store gases in solid form [1, 2, 44, 53]. While the initial surge in research, fronted by the fuel industry, aimed at finding ways to dissociate gas hydrates in pipelines, it was also realized that if hydrates could form so easily in the man-made conditions of pipelines, they certainly form in nature under similar conditions. It is estimated that natural deposits of gas clathrate hydrates (methane) may be twice as great as the entire global fossil fuel reserve [61]. The obvious commercial interest in this has made research into hydrocarbon clathrates a priority, however sequestration of other gases is also of interest.

Carbon dioxide is a greenhouse gas which is a leading contributor to global warming on Earth [62]. At present, approximately 10 billion tonnes of CO_2 is released into the atmosphere each year by the combustion of fossil fuels. In order for atmospheric concentrations to be stabilized, this figure would have to be reduced to about 5.5 billion tonnes [62]. The fact that CO_2 can form clathrate hydrates led Marchetti to propose, in 1977, using this as a viable method of mitigating this increasing danger to our planet [63]. The basic idea would be that CO_2 emissions from industry, which are currently released into the atmosphere, could instead be collected and stored in clathrate hydrate form, thus removing them from the carbon cycle.

The viability of both of these examples of gas sequestration relies on the ratio of host to guest molecules in the hydrate as well as the pressures at which the structures stabilize. Most gas hydrates adopt structure I at the lowest pressures. Transformation into structure II will result in an increase in gas storage capacity by as much as 1.5% assuming full cage occupancy. Transformation to structure H, on the other hand, could potentially increase storage by up to 70% when the large cage is occupied by 5 guest molecules. Even better, the guest:host ratio of the FIS suggests a gas storage capacity increase of 187% over the sI clathrate. Practical sequestration techniques in any gas clathrate hydrate system would require stability of these high density structures at relatively low pressures. Since the FIS is known to only exist at pressures unreasonable for practical sequestration, it represents an interesting topic of fundamental study.

Naturally occurring, methane hydrate, for example, is known to exist in all three clathrate structures at different pressures and temperatures. Molecular dynamics studies done by Susilo *et al.* found than methane hydrate sI becomes stable at 2.65 MPa at 0°C and has a near complete (90%+) occupancy, able to store approximately 160-170 gas volume/hydrate volume (v_g/v_h) which is the highest ratio found for any hydrate structure [64]. Pure sII and sH hydrates are also possible, however the pressures required become too high for any practical fuel storage. Structure H has been reported to exist with full (5 guests) occupancy of its large cage above 0.6 GPa (286 v_g/v_h) [64]. With the aid of larger molecule help gases stabilizing the large cage of sH hydrate, it is possible to create a binary gas hydrate (methane+help gas) which exists at a lower, and thus more practical pressure than even sI hydrate, however methane content suffers as a result, dropping to ~143 v_g/v_h [64].

Aside from the study of gas storage in high density hydrates such as methane hydrate sH, purely academic interest exists in exploring the stability conditions and different phases of clathrate hydrates. Not all gas clathrate hydrates are capable of realizing the storage potential of sH hydrate. Depending on reasons previously discussed about guest size, and additional reasons to do with molecular shape, certain hydrate systems never adopt the hexagonal structure entirely before proceeding to a FIS or to dissociation. In Figure 2.4, pressure vs. guest diameter is plotted for a few hydrate systems, along with the structures observed in each case.

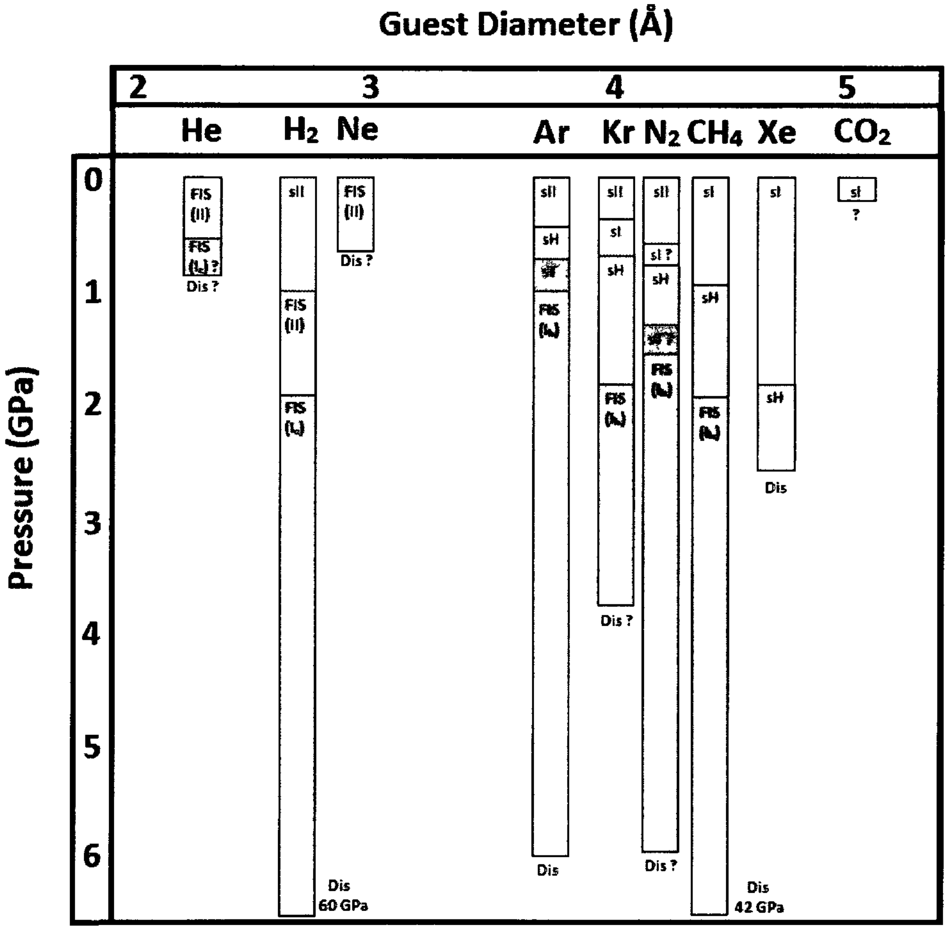

Figure 2.4 – Guest atoms or molecules shown with increasing diameter and the known hydrate structures they adopt as a function of increasing pressure. Clathrate hydrates involved are the cubic structure I (sI), cubic structure II (sII), hexagonal structure (sH), and the tetragonal structure (sT). Filled ice structures resembling Ice I_h , Ice Ic, and Ice II are labeled (FIS I_h), (FIS I_c) and (FIS II) respectively. Systems that dissociate in the shown pressure range are labeled (Dis). Data accumulated from various sources [1, 55, 65-77].

It is apparent in Figure 2.4 that guests with larger diameters tend to form sI initially and then transform into sH at higher pressures. Guests with diameters below ~4.5 Å tend to adopt sII before sI and then proceed to sH clathrate. Guests below ~4 Å in diameter such as argon and hydrogen have been known to multiply occupy smaller cages in order to stabilize them. Data on He and Ne clathrates has shown that pure hydrates are not possible, but Ice II – like structures are possible. All clathrate systems, with the exception of Xe hydrate, eventually assume a FIS resembling Ice I_h at high guest diameter, and Ices II and I_c at lower guest diameter. This is the case at least at room temperature. Figure 2.4 should not be taken to represent definitive phase boundaries but rather as a rough guide to observable trends among various clathrate systems. Experimental temperatures in the above table vary depending upon the source.

Now that a basic idea of gas hydrate formation, structure, hydration trends versus pressure, and research motivation have been examined, the remainder of this thesis will focus on our recent work on the CO_2 – H_2O system.

Chapter 3 - The CO_2-H_2O system: background and sample preparation

3.1 - The CO_2-H_2O system

CO_2 clathrate hydrate was first discovered in 1882 by Wrobelski [78] and like most other gas clathrate hydrates was treated as an academic subject until the idea of its use for sequestration became popular. In 1954, cumulative diffraction work [42] on CO_2 hydrate classified it as a structure sI clathrate hydrate. Work up to 25 MPa [79] established the dissociation line of CO_2 sI hydrate into its constituents, as seen in Figure 3.1.

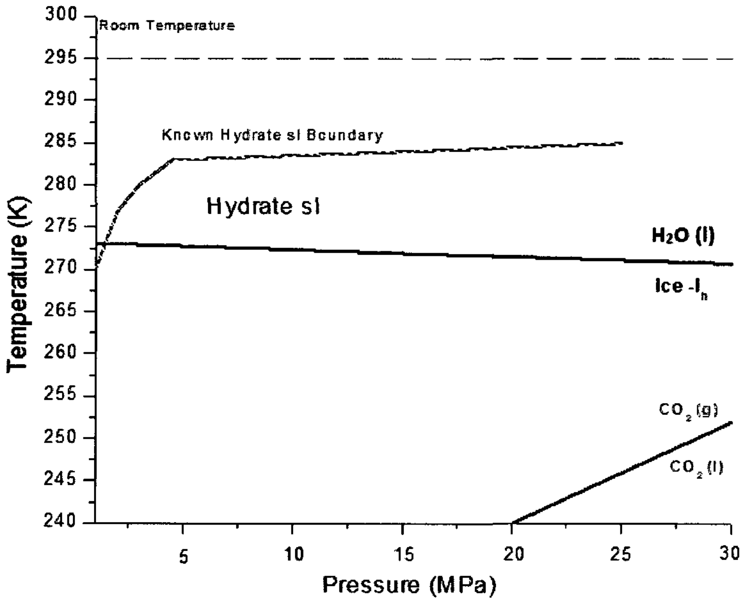

Figure 3.1 - Superimposed phase diagrams of pure H_2O, pure CO_2, and the known dissociation boundary of CO_2 sI hydrate [28, 79, 80]. The l and g subscripts refer to liquid and gaseous phases respectively.

As mentioned in Chapter 2, if the formation of a dense clathrate hydrate is ever to be used as a method of carbon sequestration, maximum gas storage density must be achieved at a relatively low pressure to make it viable and useful. While pressures of GPa are simple to achieve in a DAC, they would be challenging and perhaps hazardous to achieve on a large scale. It is for this reason, perhaps, that the dissociation line was not initially studied further than 25 MPa. However, if we recall that the use of a help gas may, in some instances, drop the required pressure necessary to form a higher density structure like sH clathrate, the dissociation line warrants further study.

Motivation for beginning this project came from the fact that this system had not been studied at high pressure nearly as much as other gas clathrate hydrate systems had and the fact that CO_2 capture in a hydrated compound could represent an avenue for carbon sequestration. CO_2 clathrate hydrate presents an interesting challenge because of its molecular diameter. As noted in Figure 2.4, predictable structure trends with pressure occur for all clathrate systems. These trends break down when the guest diameter approaches a limit defined by H_2O cage diameters in a given clathrate structure. Below approximately 4 Å, the formation of sII clathrate is most likely to occur with double occupancy; the sI hydrate is adopted at higher pressure. Different types of FISs exist resembling Ice I_h, Ice I_c and Ice II. Above approximately 4 Å (when the guest size approaches the approximate diameter of the 5^{12} cage common to all structures), the sI clathrate is stable exclusively at low pressure, followed by the other clathrate structures such as sII, sH, and the FIS I_h or I_c at higher pressures. As the diameter of xenon happens to be the exact diameter of the 5^{12} cage (4.58 Å) before stretching, a much larger guest size would reduce the chances of the 5^{12} cage participating in gas species hosting. The fact that the CO_2 molecule, with a length of 5.12 Å, has been shown to form a sI clathrate hydrate leads one to the conclusion that its stability is maintained, as stated before, mainly by occupation of the large $5^{12}6^2$ cages. The closer the guest diameter gets to the 6.0 Å diameter of the large cage in sI, the less likely it is that clathrate stability will be achieved. Guests with larger diameters have been known to form sH clathrates only with the aid of help gases [53]. Taking into account that CO_2 barely meets the diameter limits of sI by stretching of the cage, it stands to reason that it may just be the largest guest capable of forming sH clathrate without a help gas.

Based on the assumption that CO_2 hydrate would present the sH structure at high pressure, Alavi *et al.*[3] published a molecular dynamics study of CO_2 sH hydrate stability in three situations: 100 K and ambient pressure, 273 K and 0.01 GPa, and 300 K and 0.5 GPa. In each case, the free energies were calculated based on the trapping of 1 CO_2 molecule in each of the small and medium cages and between 1 and 5 CO_2 molecules in the large cage. It was found that at 100 K and ambient pressure, 5 CO_2 molecules were favored energetically in the sH large cage. At 273 K and 0.01 GPa, 3 CO_2 molecules create stability. At 300 K and 0.5 GPa stability breaks down, with the best situation being 3 CO_2 molecules in the large cage. Alavi et al. [3] further stated that CO_2 sH hydrate should be more stable than CH_4 sH hydrate under these conditions. It is known that CH_4 clathrate does indeed adopt this structure and it is thus reasonable to conclude that CO_2 clathrate must as well and should, in fact, exist.

In 2008, Honda *et al.* [77] attempted to extend the current knowledge of CO_2 clathrate hydrate phases at high pressure by using DACs to reach the required pressure conditions for the formation of additional dense phases. Their study was performed between 0.3 and 3.3 GPa and 250 and 270 K by Raman and XRD and resulted in the discovery of a "new" phase between 0.9 and 1.3 GPa. To our knowledge, the structural solution of this new phase was not completed by Honda *et al.* [77] and so further study was warranted in order to determine its exact nature. Based on this new information, the phase diagram of CO_2 clathrate hydrate was extended by Honda *et al.* [77] Results are shown in Figure 3.2.

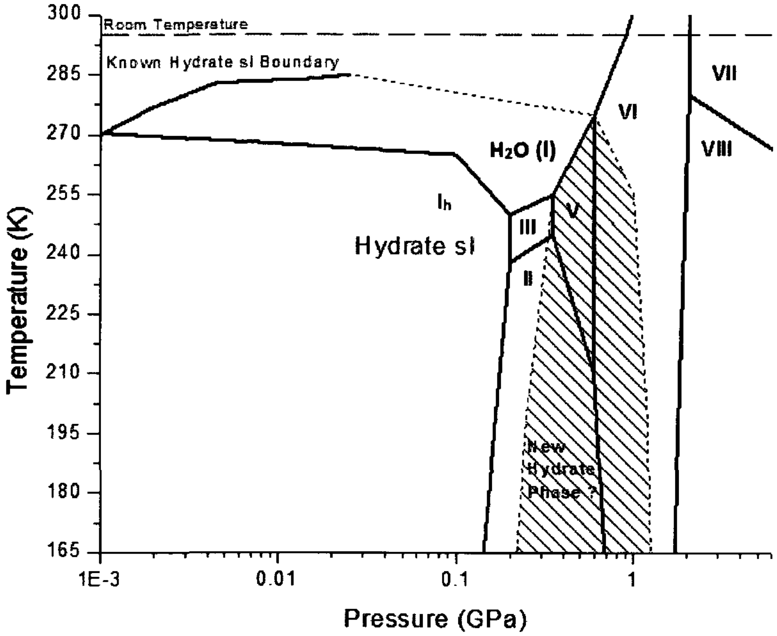

Figure 3.2 – Superimposed phase diagram of pure H_2O (black) and CO_2 clathrate hydrate (blue). The shaded region in blue represents an additional phase discovered, but unidentified, by Honda *et al.*[77].

Although the identity of the new phase was not determined in this study, a look at crystalline structures adopted with guests closely approaching the diameter of CO_2 may help to significantly narrow down the possibilities. Figure 3.3 shows the relevant section of the pressure vs. guest diameter chart presented in Figure 2.4.

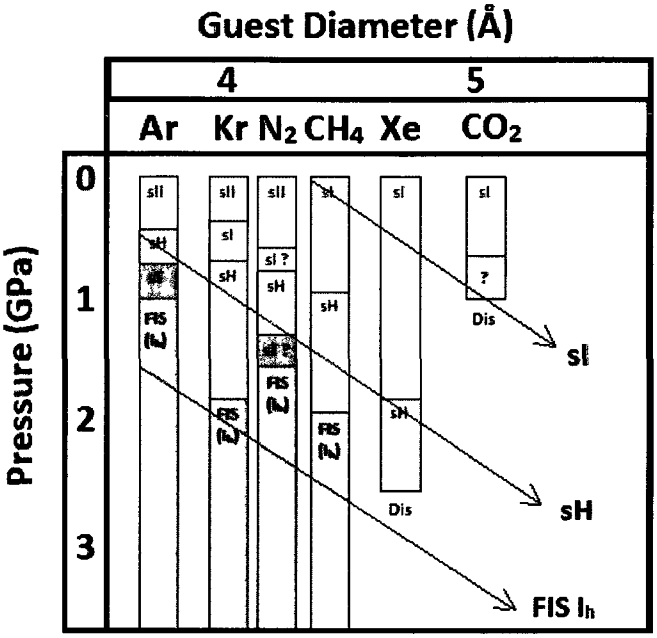

Figure 3.3 – Guest molecules shown with increasing diameter and the hydrate structures they adopt as a function of increasing pressure. The region of interest in this work for the CO_2-H_2O system is labeled in grey. Clathrate hydrate structures involved are the cubic structure I (sI), cubic structure II (sII), hexagonal structure (sH), and the tetragonal structure (sT). Filled ice structures resembling Ice I_h are labeled (FIS I_h). Systems that dissociate in the indicated pressure range are labeled (Dis). A loose trend can be seen in structures that are adopted with increasing pressure.

Figure 3.3 shows that, above 4.2 Å, all gas clathrate hydrates adopt the sI structure first, then transform into sH, and finally transform into FIS I_h structures. Xenon hydrate has not yet shown a FIS at room temperature, however it is possible that the correct isotherm has not yet been examined. Similarly, CO_2 clathrate hydrate appears to break from the observed trend by first transitioning out of sI at an inconsistently low pressure, and secondly by only adopting one new phase before dissociation (similar to Xenon hydrate). This can be explained if Honda *et al.* [77] did not examine the isotherm that would support the trend observed with the other clathrate systems, however more data is required at lower temperature. The work done in this thesis aims to continue research on the CO_2-H_2O system and to try to determine the nature of the unknown phase discovered by Honda *et al.* [77]

3.2 - CO_2 Hydrate: sample synthesis and loading

The gas clathrate hydrate formation conditions discussed in Chapter 2 are certainly applicable to the synthesis of CO_2 clathrate; however, a further challenge is presented in this case because the dissociation line exists below ambient temperature conditions, as shown in Figure 3.1. This necessitates cooling the sample preparation vessel to maintain the appropriate temperature. A study done by Kawamura *et al.* in 2002 [81] on CO_2 clathrate formation led to the conclusion that the *time required to form an equal volume of hydrate decreased rapidly close to the hydrate* dissociation boundary. Maintaining a temperature of -1°C at 1.6 MPa formed the hydrate in 70 minutes, while at -5°C it took approximately 200 minutes at the same pressure. Performing the same hydrate growth at -10°C took up to 700 minutes to obtain an equal volume.

A second consideration in hydrate synthesis is the state of the H_2O starting material. Below 50 MPa pure CO_2 exists as a gas, however H_2O will be found as either liquid or Ice I_h, depending on the exact temperature selected below the hydrate dissociation boundary. Under the conditions selected by Kawamura *et al.* [81], H_2O began as a liquid at -1°C (and 1.6 MPa), but was solid at -5°C and -10°C. This was a factor in the formation rate, as it is more difficult for the guest gas to delocalize H_2O molecules in the solid state than in the liquid state.

Because pressures below 50 MPa are difficult to attain and maintain in a DAC, a new high pressure vessel was assembled with the above considerations in mind. Figure 3.4 shows the vessel used in this study.

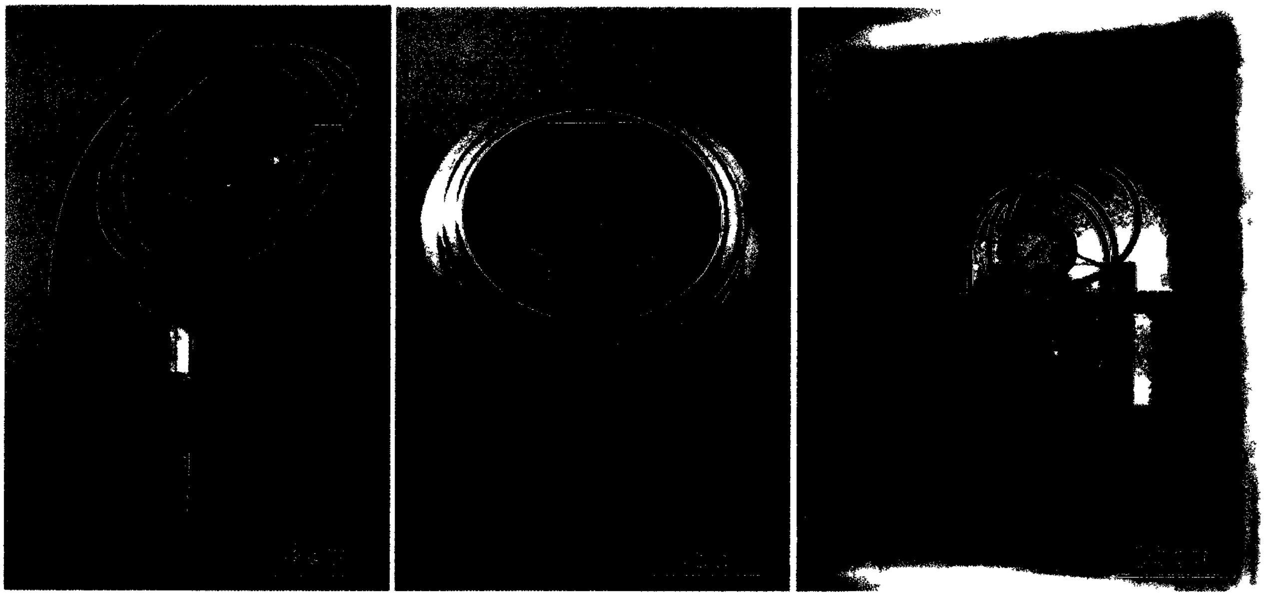

Figure 3.4 - High pressure containment vessel for synthesizing CO_2 clathrate hydrate (left). 5 steel rods are inserted in the vessel along with the constituents (center). The vessel is attached to a motor-driven rotator and then placed into a freezer (right).

The vessel shown in Figure 3.4 was machined out of stainless steel and fixed with a pressure gauge and a high pressure gas line and valve for the introduction of pressurized CO_2 gas. Before the vessel is closed and gas introduced, 5 long stainless steel rods are placed inside along with fine ice crystals made from pure distilled and de-ionized water. The vessel is attached to a motor-driven rotator and then placed into a freezer kept at temperatures below 0°C. The rotator moves the vessel continuously, causing the steel rods to fall on top of each other and crush the ice pellets into a finer powder. After a very fine ice powder is achieved, CO_2 gas is introduced at a pressure of 2.4 MPa as the vessel is kept cold (in a liquid nitrogen bath) to prevent the fine ice from melting. With the gas loaded and the valve closed, the vessel is returned to the freezer on the rotator. Gas is periodically replenished as it is absorbed into the ice. The hydrate synthesis cycling conditions are shown in Figure 3.5.

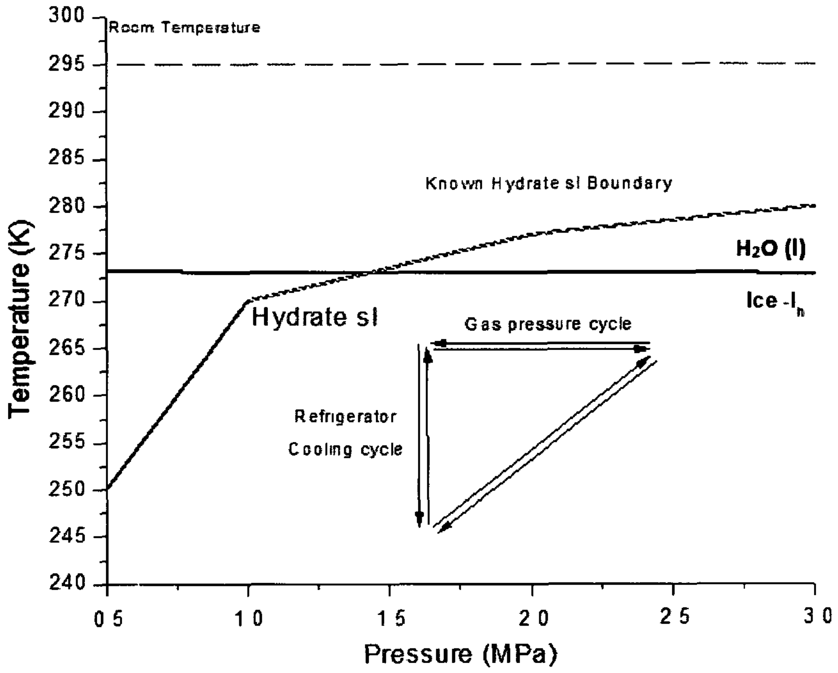

Figure 3.5 – Conditions maintained to synthesize CO_2 hydrate in this work. Freezer temperature cycling and absorption of gas into the ice caused a range of temperature and pressure conditions represented by the arrows. At all times conditions were kept below the hydrate dissociation boundary.

Because synthesis time was not important to this work, less constraint was needed on the exact formation conditions. As a result of the freezer's cooling cycle the temperature varied between -10°C and -25°C as measured by type K thermocouples placed in the freezer. The initial gas pressure in the vessel dropped down to as low as 1.7 MPa several times over a period of days due to gas uptake into the ice leading to the formation of hydrate crystals and was periodically replenished with fresh gaseous CO_2. The net result was a cycle of conditions in the vessel as shown by arrows in Figure 3.5. When the gas pressure no longer decreased, it was assumed that the ice had transformed completely to the hydrate and the sample was ready.

In order to remove the hydrate from the vessel without risking its dissociation, the vessel must be cooled sufficiently to allow the time to extract and store the powder. Because the CO_2 gas would freeze and contaminate the sample, it was first flushed out and replaced with He gas instead. The vessel was then cooled down to 77 K in a liquid nitrogen bath and the He gas was vented. The vessel was opened and the hydrate sample was transferred to a smaller container which was then immersed in liquid nitrogen for long-term storage before the DAC loading stage.

Loading the hydrate into the DAC proceeds exactly as described in Chapter 1, however the dissociation boundary requires that the sample and DAC be kept at low temperatures at all times during the loading process. The cell and all instruments used in loading are thus pre-cooled in liquid nitrogen prior to loading and the loading procedure itself is done quickly to ensure that frost does not form in time to contaminate the compression chamber before it is sealed. Figure 3.6 shows the loading of CO_2 hydrate into a DAC.

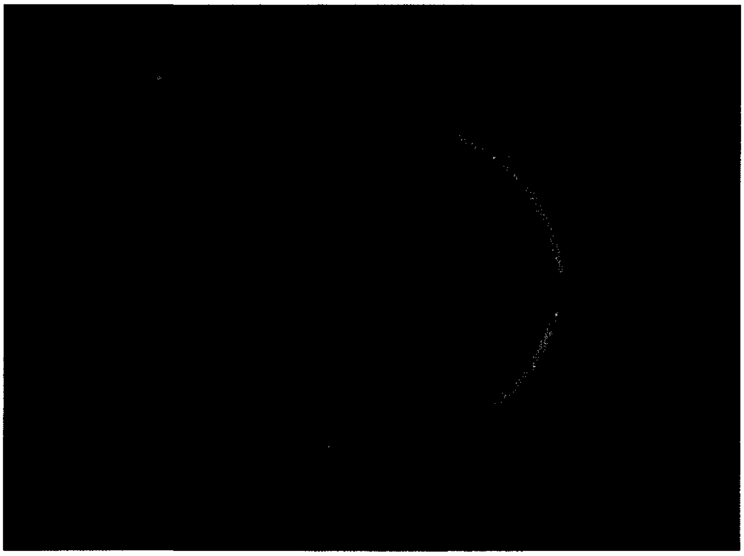

Figure 3.6 – Cryogenic loading of CO_2 hydrate. The DAC cylinder is half immersed in liquid nitrogen to keep conditions below the hydrate dissociation boundary. Hydrate crystals are smashed into a fine powder atop the gasket and then pushed into the compression chamber. The cell must be closed before frost contaminates the chamber.

After loading, the cell is quickly brought up in pressure to ensure the seal on the compression chamber and then stored in the freezer. In the following Chapter, the x-ray diffraction experiments performed on CO_2 hydrate will be presented along with the structural results obtained in this hydrate system. Comparisons will be made to the published work by Honda *et al.* [77] and conclusions will be drawn.

Chapter 4 - The CO_2-H_2O system: analysis and results

4.1 - Introduction to powder x-ray diffraction experiments

Powder x-ray diffraction was performed between 0.2 GPa and 2.5 GPa on two separate samples of CO_2 hydrate prepared from the same batch. The sample temperatures were monitored and kept between 250 K and 260 K during the x-ray exposure. The uncertainties on pressure and temperature measurements were ±0.1 GPa and ±1 K, respectively. The same structures and phase transitions obtained from the x-ray diffraction images were observed in both samples with increasing pressure; all crystalline phases were recovered upon decreasing pressure, indicating the reversibility of these phase transitions. Even the dissociated hydrate at high pressures could be returned to a pure hydrate compound with a decrease in pressure, allowing for the collection of a complete dataset as a function of pressure. Figure 4.1 shows an overlay of selected x-ray diffraction patterns at different pressures.

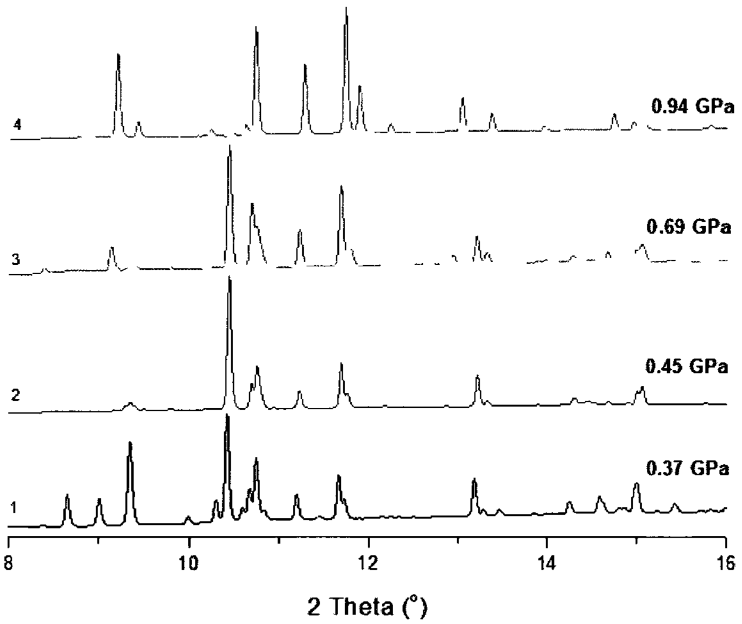

Figure 4.1 – X-ray diffraction patterns of the CO_2 - H_2O system recorded with increasing pressure. 1) Pure sI CO_2 Hydrate. 2) Phase mixture containing FIS I_h, Ice VI, and an unknown phase. 3) Phase mixture containing FIS I_h, Ice VI, CO_2, and an unknown phase. 4) Mixture of Ice VI and CO_2.

At the lowest pressure achieved in the DAC during this experiment, 0.27 GPa, pure sI CO_2 hydrate exists, as expected. A structural phase transition is observed to occur at 0.45 GPa to FIS I_h, with the release of excess H_2O forming Ice VI, and an additional phase of unknown structure. Pure CO_2-I appears in the mixture at 0.70 GPa. By 0.94 GPa, a complete dissociation of the hydrate compound to H_2O (Ice VI) and CO_2 (CO_2 -I) is achieved. Indexing and refinement of the crystalline structures, for 3 cases representative of each phase of interest in the CO_2-H_2O system, will be presented where required in the following sections: first, pure CO_2 hydrate sI at 0.27 GPa and 260 K, second, FIS I_h and Ice VI at 0.45 GPa and 250K, and finally, dissociation at 0.94 GPa and 250 K.

4.2 – sI CO_2 Hydrate

Like most gas clathrate hydrates with guests above 4 Å in diameter, CO_2 hydrate adopts sI initially at low pressures (~5 MPa [82]). Figure 4.2 shows a comparison between the expected x-ray diffraction pattern from a sI hydrate with full cage occupancy (top, simulated using PowderCell with published parameters [53, 83,84]) and the observed x-ray diffraction pattern of one of our samples (bottom). As a first step in pattern analysis, an attempt at simulating the expected x-ray diffraction pattern was made. It is apparent that a major discrepancy exists between the simulated pattern and the observed pattern. The (200), (210), and (211) peaks which dominate the simulated sI diffraction pattern between angles 4° and 7° (2θ) are entirely missing from the observed x-ray diffraction pattern. While it is possible to index the remaining pattern and get a good agreement with the sI structure, it is better to deal with this discrepancy first.

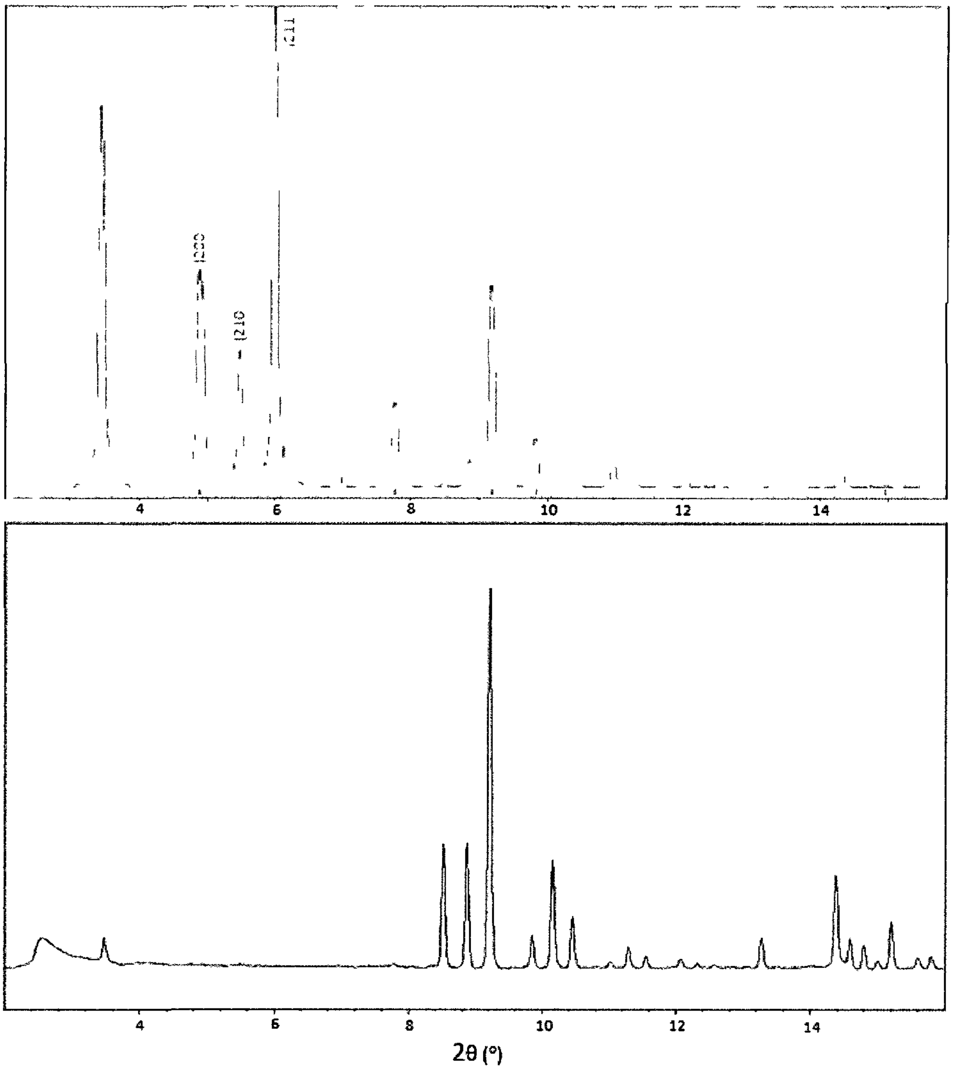

Figure 4.2 – Comparison of simulated x-ray diffraction pattern for CO_2 hydrate sI (top) and observed pattern (bottom). Certain peaks that exist in the simulated pattern are absent from the observed pattern between the angles of 4° and 7° (2θ).

As previously mentioned, gas clathrate hydrates usually present non-stoichiometric properties, such as variable cage occupancies, which complicate their structural characterization. The x-ray diffraction pattern for sI hydrate (Figure 4.2, top) was simulated under the assumption that each cage was fully occupied with one guest molecule occupying fixed coordinates. In reality this may not be true as cages do not necessarily have to be fully occupied for the hydrate to stabilize [53]. Furthermore, the guest molecules are not strongly bonded to the cage and are thus not localized in one place; they tend to occupy different areas within the cage depending on its geometry (not necessarily in the center) and their interactions with other guest molecules in the same cage, which is a subject beyond the scope of this work. When 5 guest atoms occupy the large cage in sH hydrate, for example, they will assume a trigonal bipyramid arrangement [3]. Some molecules, like CO_2 specifically, even show evidence of rotation up to 31° away from its equatorial plane [85]. With this in mind, the simulation was redone in Figure 4.3, assigning the CO_2 molecules a lower contribution to the diffraction pattern.

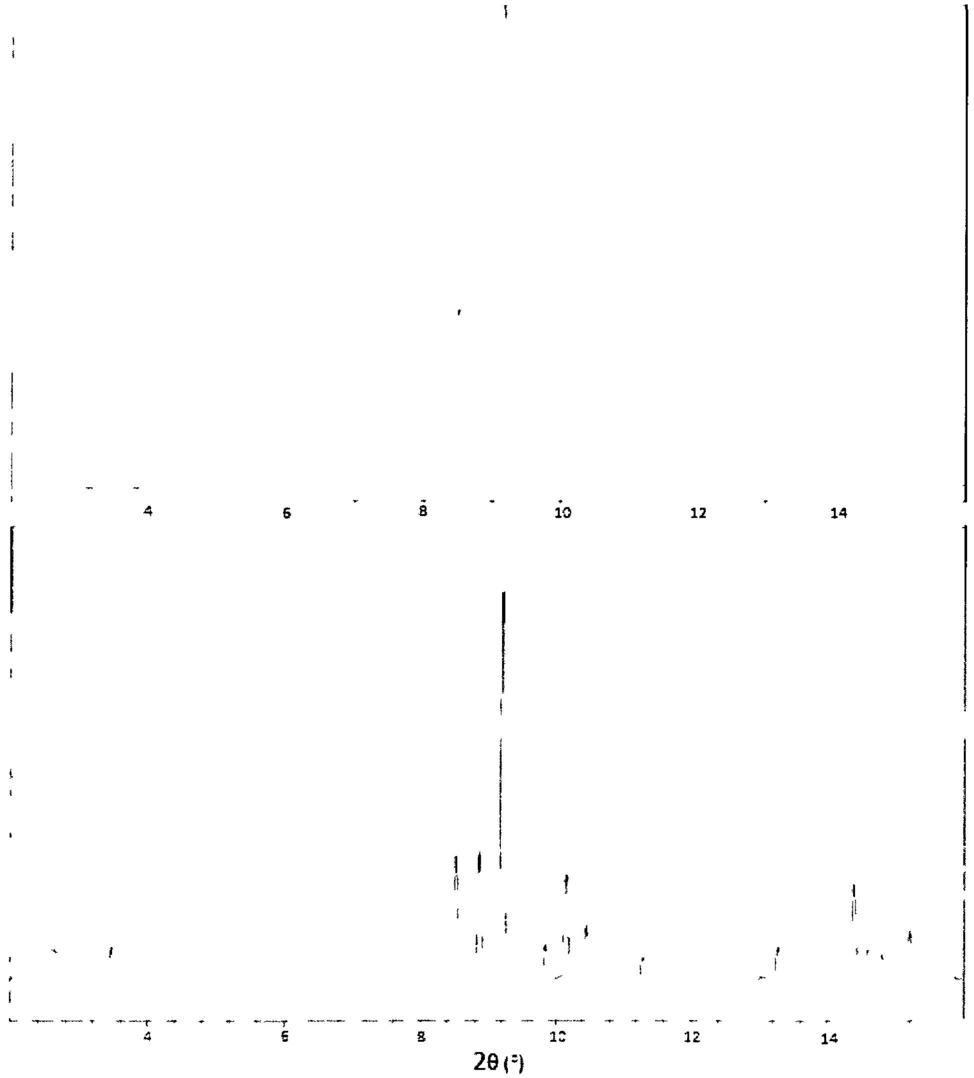

Figure 4.3 - Comparison of x-ray diffraction simulated pattern for CO_2 hydrate sI having low CO_2 site occupancy (top) and observed pattern (bottom). The (200), (210), and (211) peaks that were strong for full cage occupancy between the angles 4° and 7° (2θ) have now vanished. The calculated and observed x-ray diffraction patterns closely resemble each other.

This time the simulated pattern agrees visually with the observed pattern. The (200), (210), and (211) peaks almost completely vanish as CO_2 site occupancy is lowered below 5%. These simulations suggest that the CO_2 cage occupancies must be low; however, due to the multitude of factors mentioned above about guest positioning and rotation, an estimation of the true cage occupancies can only be done through a proper structure refinement of high quality x-ray diffraction data. Before this, however, indexing results are presented.

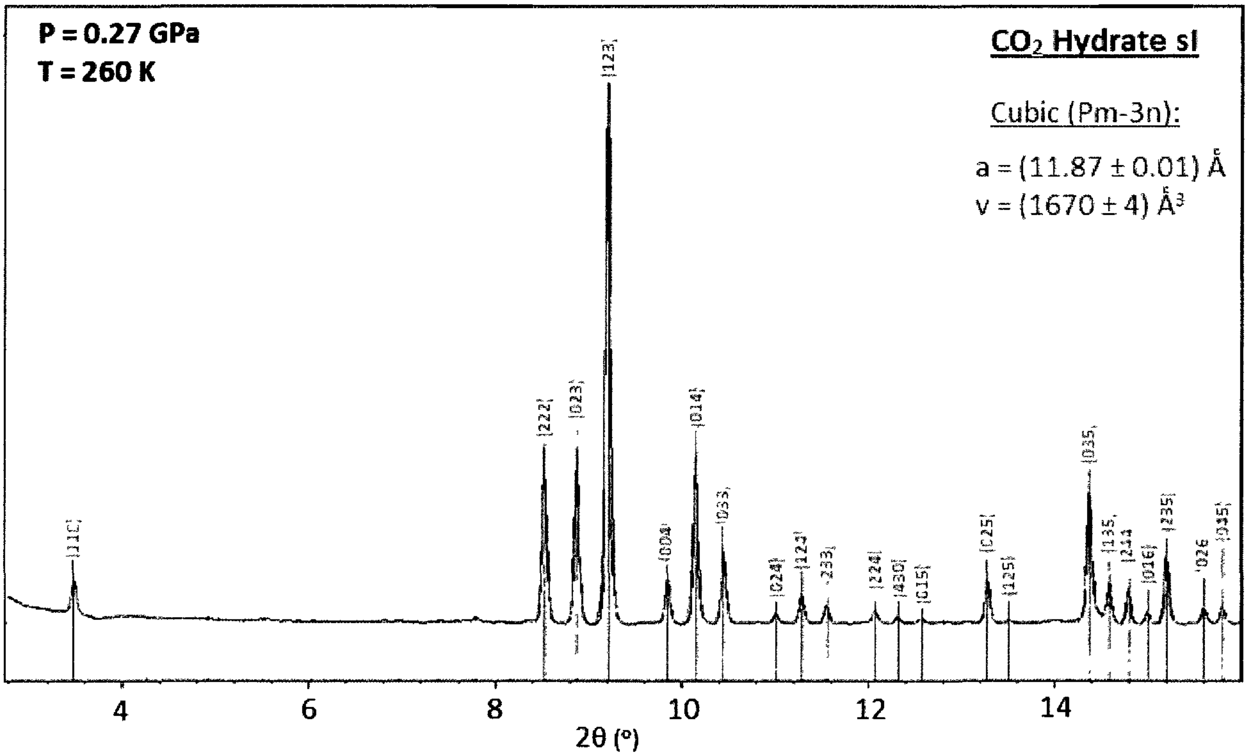

Figure 4.4 - Indexing of peaks recorded by x-ray diffraction of sI CO_2 hydrate done in XRDA. All peaks in the diffraction pattern match expected reflections for an sI clathrate with low guest site occupancy.

In Figure 4.4, the peaks observed in the x-ray diffraction pattern are indexed to the cubic sI hydrate, as observed in other hydrate systems. It is found to be in good agreement with the unit cell assignment. The lattice parameter and unit cell volume were found to be (11.87 ± 0.01) Å and (1670 ± 4) $Å^3$, respectively. Observed d-spacings for different assigned (hkl) Miller indices, as well as the differences between them and expected d-spacings, are shown in Table 4.1. From the differences in d-spacings, the agreement is excellent. Typically, (d_{calc}- d_{obs}) / (d_{obs}) is less than 0.5%.

(hkl)	$2\theta_{obs}$ (°) ± 0.001	d_{obs} (Å) ± 0.01	d_{calc} (Å) ± 0.002	(d_{calc}- d_{obs}) (Å) ± 0.01
110	3.478	8.39	8.390	0.01
222	8.525	3.43	3.425	-0.01
023	8.873	3.29	3.291	-0.01
123	9.210	3.17	3.171	0.01
004	9.847	2.97	2.966	-0.01
014	10.152	2.88	2.878	0.01
033	10.447	2.80	2.797	0.01
024	11.014	2.65	2.653	0.01
124	11.285	2.59	2.589	-001
233	11.553	2.53	2.530	0.01
224	12.069	2.42	2.422	0.01
430	12.317	2.37	2.373	-0.01
015	12.566	2.33	2.327	0.01
025	13.272	2.20	2.203	0.01
125	13.502	2.17	2.166	0.01
035	14.377	2.03	2.035	0.01
135	14.585	2.01	2.006	-0.01
244	14.795	1.98	1.978	0.01
016	15.002	1.95	1.951	0.01
235	15.203	1.92	1.925	0.01
026	15.601	1.88	1.876	0.01
045	15.795	1.85	1.853	0.01

Table 4.1 – Miller indices, observed Bragg angles (2θ), and d-spacings for diffraction peaks for sI CO_2 hydrate at 0.27 GPa and 260 K. Low differences between expected and observed d-spacings indicate a good fit to the cubic structure with lattice parameter a = (11.87 ± 0.01) Å.

Rietveld refinement was then performed to obtain exact structural parameters and cage occupancies. The structural model was based on CO_2 sI hydrate work done by Henning *et al.* [86]. Figure 4.5 shows the refined x-ray diffraction pattern with fit parameters.

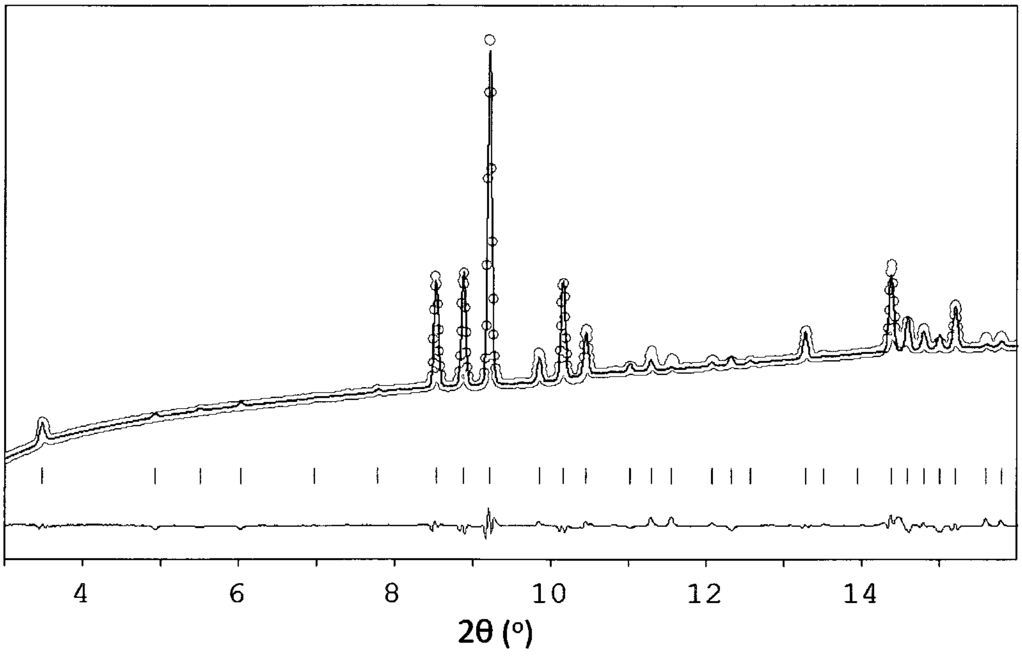

Figure 4.5 – Rietveld refinement of x-ray diffraction pattern of CO_2 hydrate sI at 0.27 GPa and 260 K. The black line represents the experimental data, the red dots represent calculated intensities, the tick marks represent calculated peak positions and the line at the bottom is the difference between the calculated and observed pattern.

Parameters used in the refinement include the scale factor, lattice parameter, profile function parameters, atomic coordinates and site occupancy of the guest atoms. Results for fractional atomic coordinates and occupancy of guest atoms are listed in Table 4.2.

Atom	X	Y	Z	Occ. (%)
O1	0.00000	0.3263	0.11172	
O2	0.18513	0.18513	0.18513	
O3	0.00000	0.50000	0.25000	
H1	0.23410	0.23410	0.23410	
H2	0.00000	0.43130	0.20510	
H3	0.00000	0.38210	0.16130	
H4	0.00000	0.31660	0.03670	
H5	0.06865	0.26710	0.13820	
H6	0.11630	0.22770	0.15760	
C1	0.00000	0.00000	0.00000	10
O4	0.01497	0.00000	0.06879	22
C2	0.00000	0.25000	0.50000	100
O5	-0.07315	0.21420	0.43800	21

Table 4.2 – Refined fractional coordinates of atoms in CO_2 sI hydrate. Occupancies of guest atoms are presented as found by FullProf. Uncertainties on occupancy could not be evaluated and are certainly larger than 10%.

Because the differences between observed and calculated patterns is small (as shown in Figure 4.5), the refinement was fairly successful, indicating the model proposed by Henning *et al.* [86] is correct. Based on the occupancy values listed in Table 4.2, the hydration formula for CO_2 sI hydrate was determined to be CO_2•17.86H_2O in this work, a value falling short of the 1:5.75 ratio of an ideal sI clathrate.

4.3 – CO_2 FIS I_h

At 0.45 GPa the sI CO_2 hydrate transforms into a mixture of phases. As mentioned in Chapter 1, when a mixture of phases exists in an x-ray diffraction pattern, it is common practice to begin analysis by indexing any expected patterns first. For the CO_2-H_2O system, the constituents, if occluded from a hydrate structure under increasing pressure as a result of phase transformation, would be present in their solid forms. CO_2 exists as a cubic structure (known as the CO_2-I phase) from 0.15 GPa until 10 GPa [87] in this temperature region (see Figure 4.6), however it was not detected initially in the mixture (it does appear at 0.70 GPa, however, as seen in Figure 4.1, pattern 3). This pressure-temperature region is especially complicated with regards to the possible phases of H_2O (see Figure 4.6). Deviations of 20K and 0.3 GPa could cause occluded H_2O to take up any one of 6 different forms.

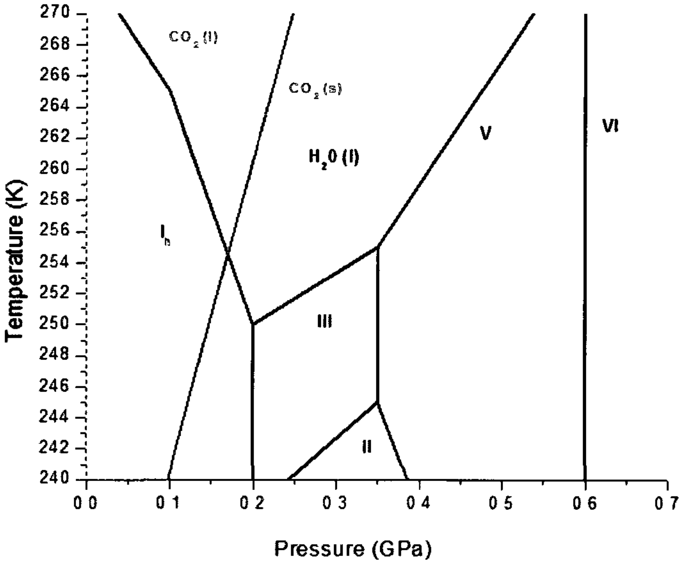

Figure 4.6 – Superimposed phase diagrams of H_2O [28] and CO_2 [79] in the region of interest. Uncertainty in pressure or temperature measurements make sorting out occluded constituent H_2O difficult because as many as 6 different phases are expected in this region of the phase diagram.

In the x-ray diffraction pattern taken at 0.45 GPa and 250 K (Figure 4.1, pattern 2), Ice VI was the only one of the possible phases observed. It should be noted that this disagrees with the phase diagram presented in Figure 4.6, even when taking into account the 0.1 GPa uncertainty on pressure measurements. As will be discussed in Chapter 5, uncertainty in pressure and temperature measurements may indeed have been underestimated.

After all the possible constituents were exhausted (Ice I_h, II, III, V, VI, CO_2-I), indexing proceeded, by assigning any unassigned x-ray diffraction peaks to the hydrate structures. If the observed trends that were discussed in Chapter 3 and the predictions from computational results of Alavi *et al.* [3] were correct, then sH hydrate should exist as the hydrate phase denser than sI in the CO_2-H_2O system. Unfortunately no evidence of this hexagonal structure was found in any diffraction images taken after the sI hydrate's pressure-induced transformation (Attempts at indexing the x-ray diffraction patterns to CO_2 sH hydrate will be presented immediately after the following discussion on CO_2 FIS I_h).

The filled ice structures were the next possibility, despite the fact that they were unexpected according to the trends shown in Chapter 3. By comparing work done on CH_4 FIS I_h [5] to the remaining peaks found at 0.45 GPa, the orthorhombic FIS I_h structure was successfully indexed. To our knowledge, this is the first instance a structure other than sI hydrate has been identified in the CO_2-H_2O system before dissociation. Figure 4.7 shows the indexing of this pattern and resulting unit cell volume, while Table 4.3 shows the resulting Miller indices. The small difference between expected and observed d-spacings indicates a good fit to the FIS I_h structure.

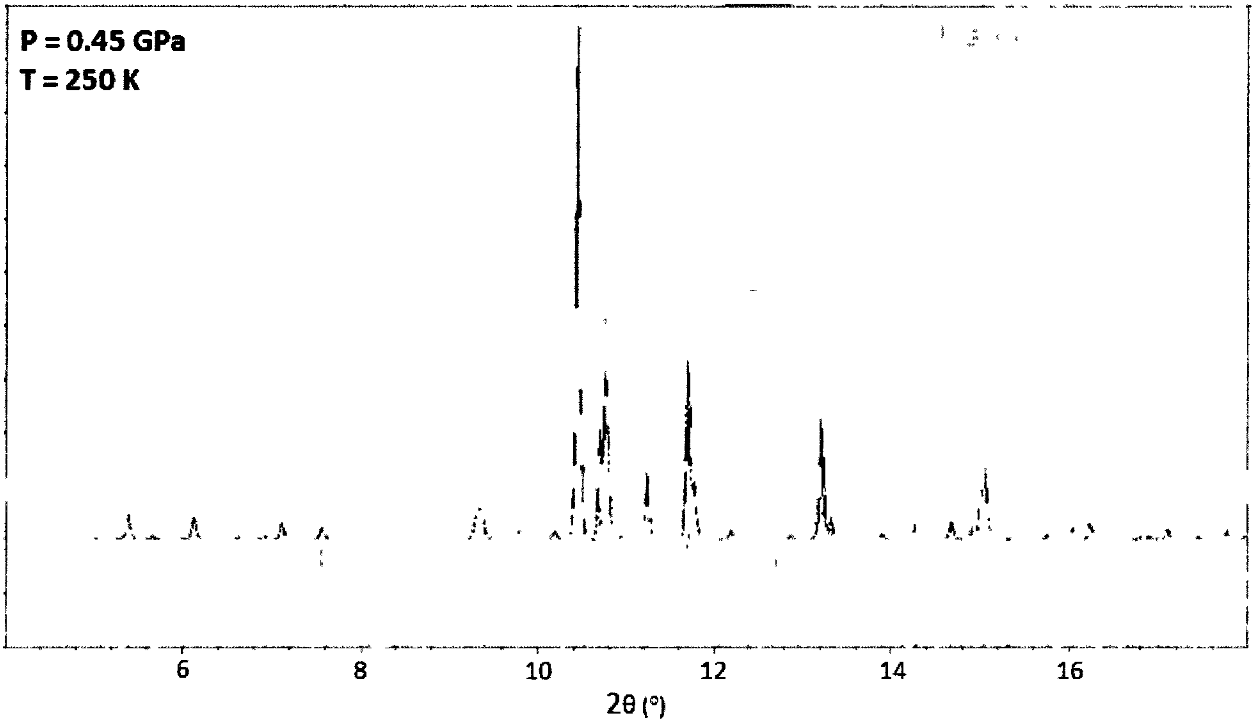

Figure 4.7 – Indexing of the x-ray diffraction pattern recorded at 0.45 GPa and 250K with CO_2 FIS I_h (green) and occluded Ice VI (red) at 0.45 GPa and 250 K. Blue tick marks represent an unknown phase in the mixture.

In Figure 4.7, Ice VI is indexed in red, CO_2 FIS I_h is in green, and the blue ticks below the pattern indicate peaks not belonging to either phase. Unfortunately this phase could not be identified and will be discussed in Chapter 5. Comparison to other FISs and clathrate structures has, so far, proved unsuccessful. Because of the number of unidentified peaks in the x-ray diffraction pattern (greater than 20), refinement of the FIS I_h was not attempted. The unidentified peaks are given in Table 4.4 for two different recorded diffraction patterns.

(hkl)	2θ (^{o}) ±0.001	d_{obs} (Å) ± 0.01	d_{calc} (Å) ± 0.002	(d_{calc}- d_{obs}) (Å) ± 0.01
011	5.395	5.41	5.408	-0.01
110	7.125	4.10	4.097	-0.01
112	10.451	2.80	2.796	0.01
211	13.211	2.21	2.213	-0.01
202	14.291	2.05	2.048	0.01
123	15.053	1.94	1.944	0.01
033	16.239	1.80	1.803	0.01
114	16.899	1.73	1.733	0.01
213	17.098	1.71	1.713	0.01
051	19.547	1.50	1.500	0.01
321	20.046	1.46	1.462	-0.01
143	20.100	1.46	1.459	0.01
242	20.990	1.40	1.398	0.01
330	21.489	1.37	1.366	-0.01
044	21.699	1.35	1.352	-0.01

Table 4.3 - Miller indices, observed Bragg angles (2 θ), and d-spacings for diffraction peaks for CO_2 FIS I_h at 0.45 GPa and 250 K. The small difference between expected and observed d-spacings indicate a good fit to the orthorhombic structure with lattice parameters a = (4.85 ± 0.01) Å, b = (7.65 ± 0.01) Å, c = (7.65 ± 0.01) Å.

d_{obs1} (Å) ± 0.01	d_{obs1} (Å) ± 0.01		d_{obs2} (Å) ± 0.01	d_{obs2} (Å) ± 0.01
5.15	2.48		5.16	1.94
4.76	2.30		4.66	1.55
3.94	2.27		3.75	1.35
3.86	2.09		3.10	
3.14	1.95		3.07	
3.12	1.79		2.94	
3.11	1.56		2.70	
3.07	1.54		2.68	
2.98	1.52		2.66	
2.71	1.49		2.46	
2.67			2.03	

Table 4.4 – List of d-spacings for unknown peaks at 0.45 GPa and 250K (left), and at 0.93 GPa and 250 K (right). It is suggested in Chapter 5 that two separate unknown phases (1 and 2) coexist with CO_2 FIS I_h at different pressures.

The indexing of CO_2 FIS I_h was presented first in order to use the unidentified peaks from that indexing in the discussion on CO_2 sH hydrate. In Figure 4.8, the same diffraction pattern as in Figure 4.7 is presented with an overlaid histogram of the expected peaks from CO_2 sH hydrate, generated from parameters given by Manakov *et al.* [70] on Argon sH hydrate.

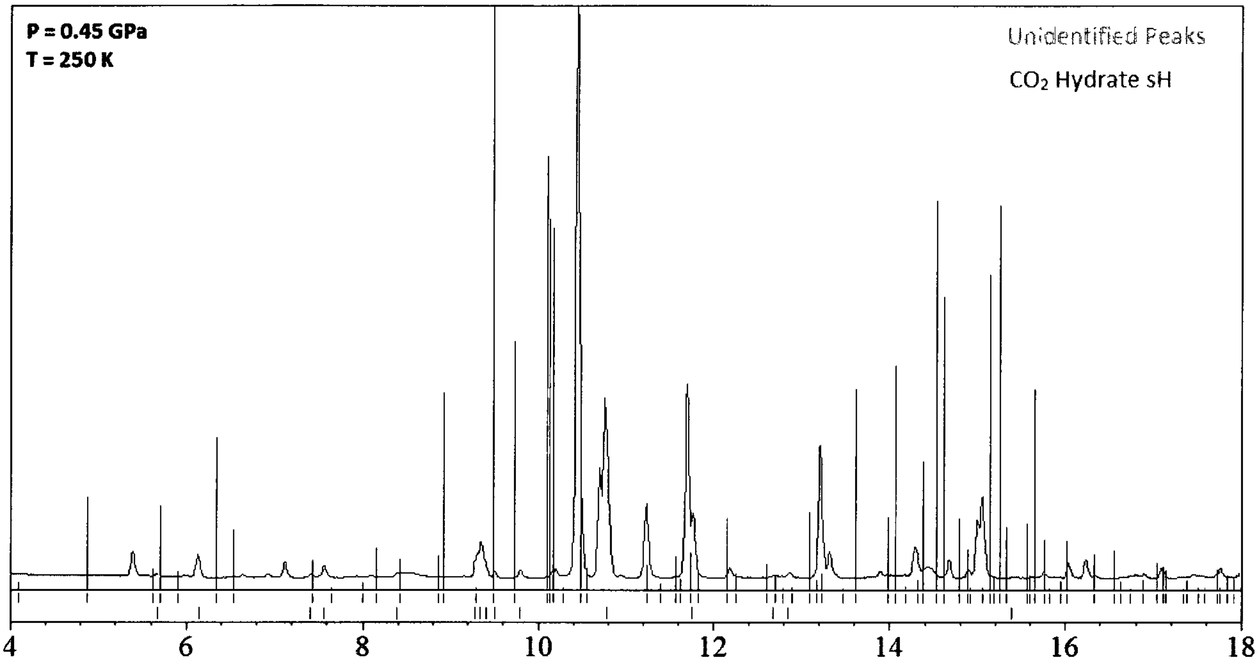

Figure 4.8 - Histogram (red bars) of CO_2 sH hydrate overlaid over the diffraction pattern taken at 0.45 GPa and 250 K. Blue tick marks represent unidentified peaks after the fitting of CO_2 FIS I_h. No match can be found between the two, indicating that CO_2 sH hydrate is likely not present.

Similar to sI clathrate hydrates, the x-ray diffraction pattern of sH hydrates should not change much for different guest molecules. Cage occupancy can change the relative intensities of the x-ray diffraction peaks somewhat, but not the peak positions. The structural parameters of Ar sH hydrate used to create the histogram in Figure 4.8 were obtained at 0.76 GPa, therefore, the histogram could potentially be downshifted in pressure compared to the diffraction pattern upon which it is overlaid on. Even correcting for this, a match between the unknown peaks and the histogram cannot be found. Finally, the lattice parameters from the Ar sH hydrate refinement by Manakov *et al.* [70] were unchanged. This could introduce errors in histogram positioning, but likely not to the extent observed in Figure 4.8. Parameters used to generate the histogram are given in Table 4.5. The fact that CO_2 sH hydrate was not observed in this study is an important finding that will be discussed further in Chapter 5.

CO_2 sH Hydrate				
Hexagonal, P6/mmm a = 11.9791 Å, c = 9.8701 Å				
Atom	X	Y	Z	Fractional Occupancy
O1	0.7929	0.5853	0.2693	1
O2	0.3333	0.6667	0.3636	1
O3	0.3842	0.0000	0.1353	1
O4	0.8639	0.7253	0.5000	1
Guest1 (S)	0.5000	0.5000	0.5000	1
Guest2 (M)	0.6667	0.3333	0.0000	1
Guest3 (L)	0.0000	0.0000	0.2972	1
Guest4 (L)	0.2182	0.1092	0.0000	0.5

Table 4.5 – Atomic fractional coordinates, unit cell symmetry, space group, and lattice parameters used to generate the histogram for CO_2 sH hydrate shown in Figure 4.8. Guest atoms are also labled to which cage they belong in brackets. Data taken from Manakov *et al.* [70].

4.4 - Dissociation into Ice VI and CO_2-I

Above 0.94 GPa at 250 K the CO_2 FIS I_h and unknown phases completely dissociate into CO_2-I and Ice VI. All diffraction peaks are accounted for in the indexing, shown in Figure 4.9, as belonging to one of the two constituents. After dissociation, increasing pressure up to 2.5 GPa at 250 K yielded only the expected transition of Ice VI to Ice VIII. All previous phases can be recovered upon reduction in pressure.

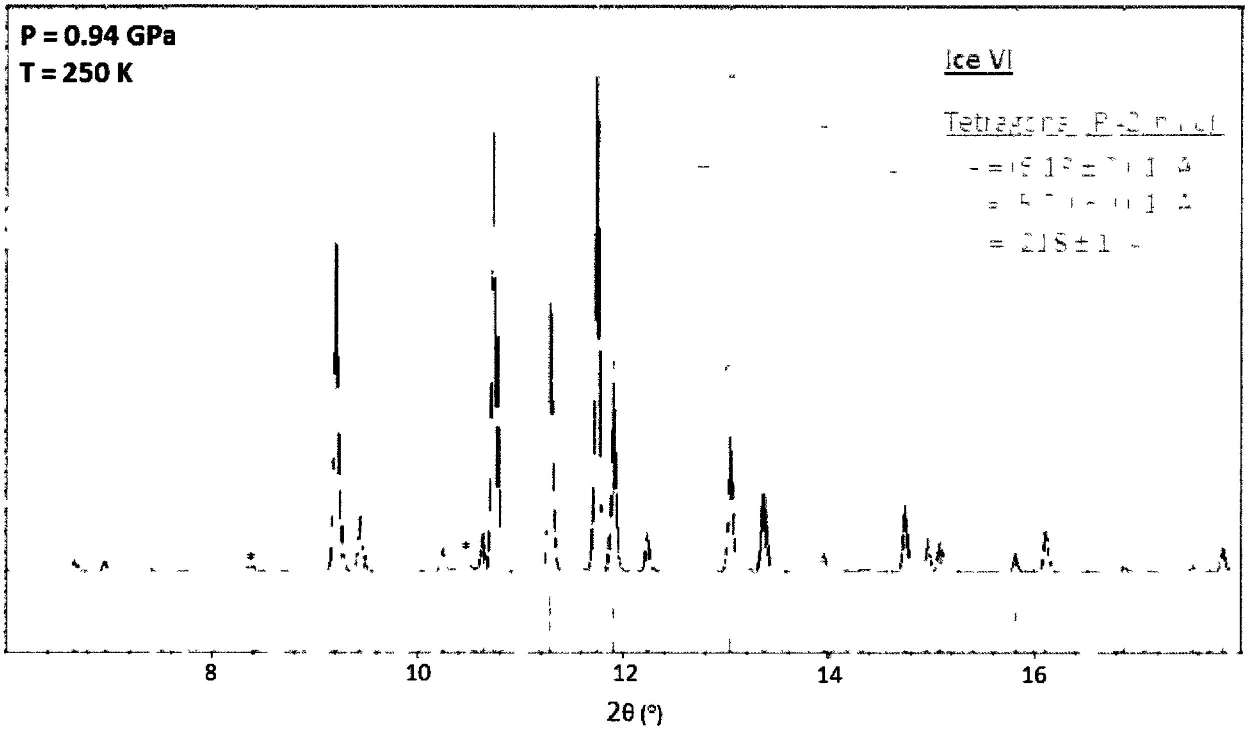

Figure 4.9 – Indexing of peaks recorded by x-ray diffraction at 0.94 GPa and 250 K. All peaks in the diffraction pattern match expected reflections for either solid CO_2 (red) or Ice VI (green). * indicate two unidentified peaks likely arising from a contaminant.

In the next chapter, the present results are discussed and compared to previous reports of similar structures. An amendment to the existing phase diagram will be followed by the outlook of CO_2 hydrate as a means of carbon sequestration, as well as future work required on this subject.

5.1 – Comparison of CO_2 hydrate sI to other systems

Of all the x-ray diffraction experiments carried out on both CO_2 hydrate samples, seven x-ray diffraction images were identified as containing CO_2 sI hydrate between 0.27 GPa and 0.76 GPa. The unit cell volumes measured for CO_2 sI hydrate as a function of pressure and V/V_0 as a function of pressure are graphed in Figure 5.1 along with data from two other systems that form sI clathrate hydrate: xenon hydrate and methane hydrate [10, 74, 83, 88-91].

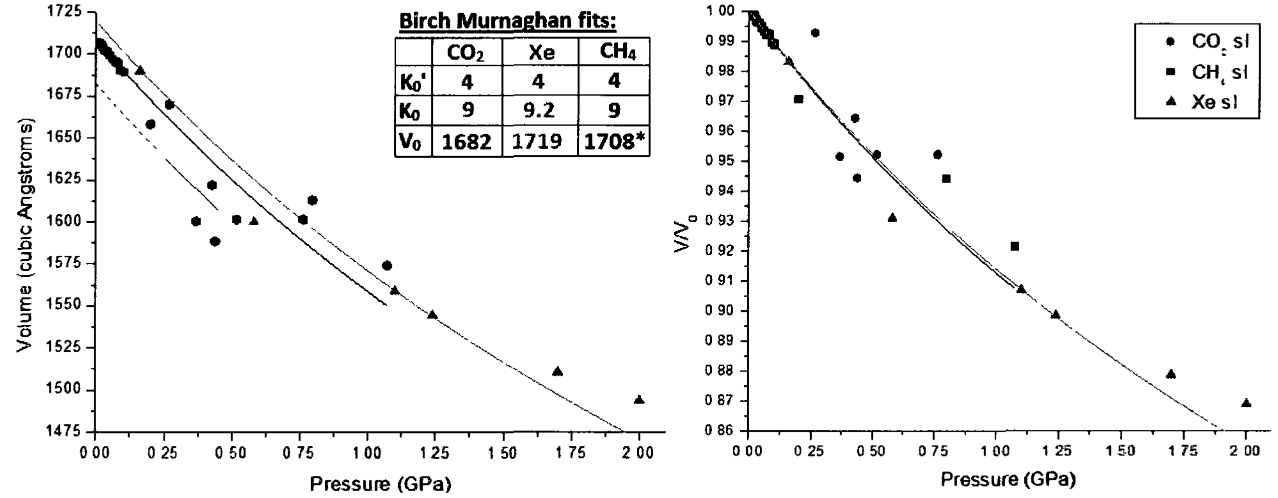

Birch Murnaghan fits:

	CO_2	Xe	CH_4
K_0'	4	4	4
K_0	9	9.2	9
V_0	1682	1719	1708*

Figure 5.1 Unit cell volumes (left) and V/V_0 (right) vs. pressure of sI clathrate hydrate for three different systems. Overlaid are Birch-Murnaghan equations of state that best fit the available data (fit parameters are given in the inset table in the left panel). Data for xenon and methane hydrates are compiled from many sources [10, 74, 83, 88-91]. The parameter marked with an asterisk was altered to better fit the published data [89]. Uncertainty on V, V_0, K_0, and P for CO_2-sI are 8 Å^3, 20 Å^3, 0.5 GPa, and 0.4 GPa respectively.

The fits to the Birch-Murnaghan equation of state in Figure 5.1 (left) are overlaid to guide the eye and bring out the trends in the data. Unfortunately, not much experimental data is available in literature on the compression of sI clathrate hydrates to high pressure. This is surprising as the methodology to pursue this research has been around for two decades. Various bulk moduli (K_0) have been proposed in each system with little success in fitting all available data. Nevertheless it is possible to make general observations based on the accumulated data shown in Figure 5.1 (left). The compression of xenon and methane hydrates follow nearly identically, save for the different values of V_0. It stands to reason that xenon, being the larger of the two guests, should form a larger unit cell than methane. Theoretical studies carried out on sI clathrate hydrates [92] show that the influence of guest molecules having a large van der Waals radius leads to slight stretching of the host lattice. This line of reasoning breaks down, however, with the consideration of the CO_2 sI hydrate data. Data from Udachin *et al.* [83] place V_0 for CO_2 hydrate sI below that of methane (1682 $Å^3$). Because the CO_2 molecule is larger than methane and xenon, one would expect it to appear above 1719 $Å^3$ on Figure 5.1 (left). Despite this discrepancy, bulk moduli were selected to best model the available data. In Figure 5.1 (right), the data was re-plotted with V/V_0 on the vertical axis. In this way, the relative compressions of all sI hydrates considered can be compared. Because of the similar bulk moduli used to fit the data of all three systems, the compression rates are nearly identical. This makes sense as the majority of the sI structure, such as the host framework, is made from hydrogen-bonded H_2O. With more data, especially for CO_2 sI hydrate, the equations of state can be improved. It is unlikely, however, that substantial change will be observed from the values given in Figure 5.1, considering that the structures are identical and the guest molecules' bonding are not strong.

In addition to the lack of data for sI hydrates as a function of pressure, the data available was all collected at different temperature conditions. Temperature has a substantial effect on lattice parameters [92], thus this is another reason why comparison among these systems is difficult. Even the temperature range used in this work (250 to 260K) would be affected by this somewhat. The equation of state obtained for sI CO_2 hydrate in the course of the present work, although subject to several sources of error, is nevertheless quite accurate.

From the scattering of the sI CO_2 hydrate data, it is clear that problems arose in accurately measuring the pressure. It should be noted that it is difficult to measure pressure using the ruby fluorescence method below 1 GPa, and exceedingly difficult when temperature correction must also be applied. Based on the pressure measurements for the FIS I_h phase of CO_2 which occurs at higher pressure, the transition from the sI to the next phase was set at 0.45 GPa and 250 K. A Raman spectroscopy study with more stringent control of pressure and temperature could be used in the future to verify the assignment of the transition pressure.

Despite difficulties inherent to pressure measurement, enough sufficient quality x-ray diffraction patterns were obtained to perform the refinement of CO_2 sI hydrate shown in Chapter 4. The hydrate structure cage occupancies obtained from the refinement along with those obtained in other studies of CO_2 sI hydrate and other sI hydrates are given in Table 5.1. The hydration numbers along with pressure and temperature conditions are included.

Guest Species	Cage Occupancy (%)		Hydration Number	Pressure (MPa)	Temp. (K)	Reference
	Large Cage	Small Cage				
Kr	67.53	77.25	8.22	50	295	90
N_2	108.4	95.7	5.46	75	273	93
CH_4	97.4	87.6	6.06	3.36	273	94
Xe	75.68	81.10	7.46	160	295	90
CO_2	10	100	17.86	270	260	This work
	73	98	7.26	6.2	14	86
	99	90	5.94	1.3	7	96

Table 5.1 – Cage occupancies, hydration numbers, and experimental conditions for several sI hydrate forming systems.

In Table 5.1, guest species are listed in order of increasing diameter. At first glance, no observable trend is seen among the cage occupancies and hydration numbers shown. The predominant reason for this is that the available data in literature were all acquired under different experimental conditions of pressure and temperature. Compression or change in temperature of sI hydrate may affect the occupancy of its cages, especially over the ~290 K range of Table 5.1. This fact was highlighted by the theoretical study done by Alavi *et al.* [3] on CO_2 sH hydrate, which concluded that the occupancy is much greater for that structure at low temperatures.

To further complicate matters, work by Henning *et al.* [86] provides evidence that synthesis conditions also affect the final cage occupancies. In the data presented in Table 5.1, several key differences in synthesis procedure can be observed. In the work of Chazallon and Kuhs [93] and Sum *et al.* [94] on N_2 and CH_4 sI hydrates respectively, formation of the hydrate was restricted to pressure and temperature conditions directly below either system's dissociation line for a period of 2-3 weeks. The idea of holding the conditions as close as possible to the dissociation line has been established as ideal by Kawamura *et al.* [81] because it will create the hydrate in the shortest amount of time. The result of this synthesis approach produced sI hydrates with cage occupancies of 108% and 95% for the large and small cages of N_2 sI hydrate respectively, and 97% and 87% for those of CH_4 sI hydrate, as seen in Table 5.1. (The figure of 108% includes a statistical occurrence of doubly occupied large cages, something not possible in the other systems discussed, but true of N_2 sI hydrate).

The synthesis used to produce Kr and Xe sI hydrate for Flacau's studies [90] used a method described by Handa [95]. Ice in a high pressure vessel containing excess guest gas was continually ground by falling metal rods inside the vessel for a period of 7 days. The temperature was held at 253 K in both cases; a temperature more than 60 K lower than the hydrates' dissociation boundaries as seen in Figure 2.3. The fact that the synthesis conditions were farther away from the dissociation boundaries of the hydrates than suggested by Kawamura *et al.* [81], and because the conditions were maintained for a shorter time, led to cage occupancies of 67% and 77% for the large and small cages of Kr sI hydrate, and 75% and 81% for those of Xe sI hydrate.

The synthesis method used in this work is similar to those described above for the studies of Kr and Xe. However, in the present report, careful control of the synthesis temperature over long periods of time could not be realized (as described in Chapter 3, the freezer used constantly cycled between -10°C and -25°C). Thus, the quality of the sample in powder form was likely not as good. The crushing of the Ice I_h starting material could have been insufficient to produce a very fine powder as compared to that reported for the Kr and Xe studies. The more crushed the ice is, the more surface area exists for the gas to permeate leading to more efficient hydrate formation. The final occupancies found for CO_2 sI hydrate in this work were 9% and 100% for the large and small cages respectively.

The other two works on CO_2 sI hydrate shown in Table 5.1 had key differences in their syntheses. The work by Henning *et al.* [86] began sample synthesis close to the dissociation line until an estimated 50% occupancy was reached, and then ramped up the temperature across the boundary to 278 K. This quickened the process of cage filling that would normally take several weeks by the other methods described, but took only hours according to Henning et al. [86]. The occupancy reported in that work was approximately 73% and 98% for the large and small cages respectively.

The work in Table 5.1 that produced the highest occupancies for CO_2 sI hydrate was that of Ikeda *et al.* [96], where 90% and 99% occupation of the large and small cages, respectively, were recorded. Ikeda *et al.* [96] achieved this by allowing more than one month for synthesis to occur. Like Henning *et al.* [86], the sample was cycled across its dissociation boundary between 253 K and 277 K to increase the reaction rate. In addition, several times during the synthesis, the sample was extracted from its vessel and reground manually under a CO_2 atmosphere to ensure the quality of the powder.

The conclusion that can be reached following this discussion is that it is likely possible to achieve full occupancy for a sI hydrate in any system, provided sufficient care is taken in sample preparation. The lack in occupancy of the large cages in this work need not be an indication that CO_2 sequestration in clathrate hydrates is not possible.

5.2 – Comparison of CO_2 FIS I_h to other systems

Four x-ray diffraction images were recorded, and subsequent patterns indexed as containing the orthorhombic CO_2 FIS I_h between the pressures of 0.45 GPa and 0.94 GPa. For discussion purposes, lattice parameters of FIS I_h in two other systems were graphed alongside those of CO_2 FIS I_h in Figure 5.2.

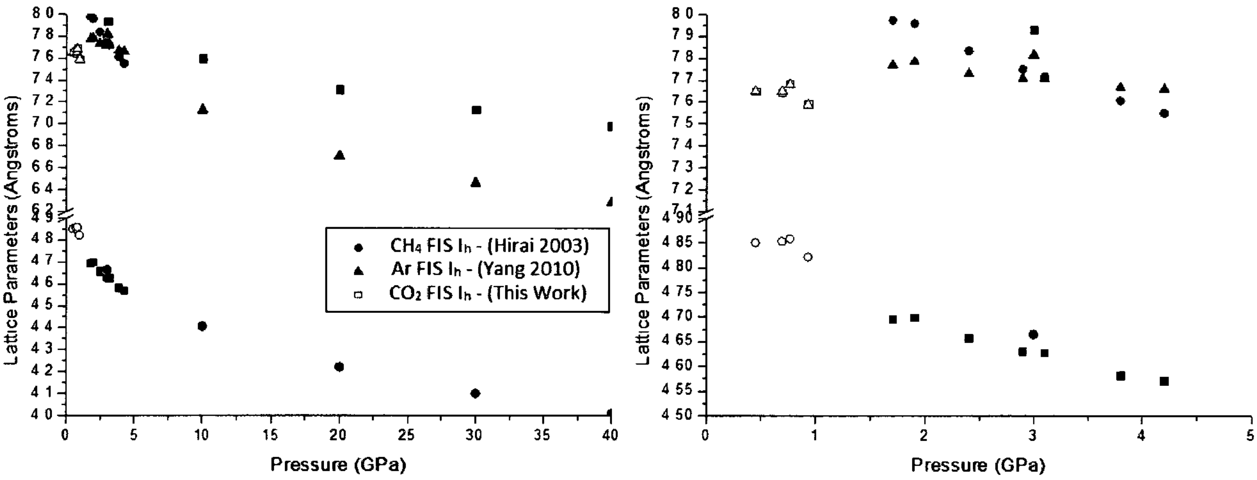

Figure 5.2 - Comparison of orthorhombic FIS I_h lattice parameters vs pressure for three different systems. Data for Ar-H_2O and CH_4-H_2O systems taken from works by Yang *et al.* [97] and Hirai *et al* [66] respectively. Data points shown with squares, circles, or triangles represent a, b, and c lattice parameters respectively. The left graph shows the entire range of data points in which methane FIS I_h exists, while the right graph shows the low pressure region of interest. The b and c lattice parameters are nearly identical for the CO_2 FIS I_h and thus overlap on the graph. Uncertainty on lattice parameters and P for CO_2 FIS I_h are 0.01 Å and 0.4 GPa respectively.

The work by Hirai *et al.* [66] on methane FIS I_h indicates that the phase is stable up to at least 42 GPa. As pressure is reduced, the lattice parameters increase steadily. Between 10 GPa and 3 GPa the *c* parameter, indicated with black triangles in Figure 5.2, increases its slope of relaxation compared to the other parameters, falling short of equaling the *b* parameter before it reverts to the sH phase. In the work on argon FIS I_h by Yang *et al.* [97], a similar trend is observed going down in pressure from 4.2 GPa to 1.7 GPa with a crossing occurring at 3.2 GPa. The reason for this anisotropic compressibility of the c parameter was attributed by Hirai *et al.* [66] to the fact that linking between layers of H_2O and guest rings in the FIS I_h structure produce large channels perpendicular to the *c* direction. The increase of pressure quickly reduces these channels, and the *c* parameter's compressibility returns to that of the other two lattice parameters. Because only four data points were taken for the CO_2 FIS I_h, it is unclear whether a similar anisotropic compression can be observed in this system. However, judging from the fact that the b and c parameters are nearly identical over the small stability range observed in this work, it is unlikely.

The fact that the b and c lattice parameters are nearly identical may also lead one to wonder if the structure under consideration is in fact tetragonal, not orthorhombic. This is likely not the case, and only a coincidence, as the diffraction pattern closely resembles those of other orthorhombic FISs like Hirai et al. [66] with similar relative intensities. This question may be solved by extending the range of CO_2 "FIS I_h" in Figure 5.2 to see if the lattice parameters separate, although this may not be possible before the compound dissociates.

The *b* and *c* lattice parameters in CO_2 FIS I_h are also noticeably smaller than those in the argon and methane examples (smaller by ~0.3Å). Compensating for this is the increase in the *a* lattice parameter by ~0.15Å compared to the other two systems. These differences in lattice parameter may be explained by the linear shape and size of the CO_2 molecule itself, whereby the long axis requires a longer dimension of the ice structure in which to fit, yet not as much in the other directions. The other two examples of hydrate with the FIS I_h structure have guest species (Ar and CH_4) which possess more spherical electronic distribution. Despite the changes in the lattice parameters of CO_2 FIS I_h, the unit cell volumes remain similar to those observed in the other two systems. In Figure 5.3, the unit cell volumes of CO_2 FIS I_h are graphed as a function of pressure alongside those by Hirai *et al.*[66] and Yang *et al.*[97]

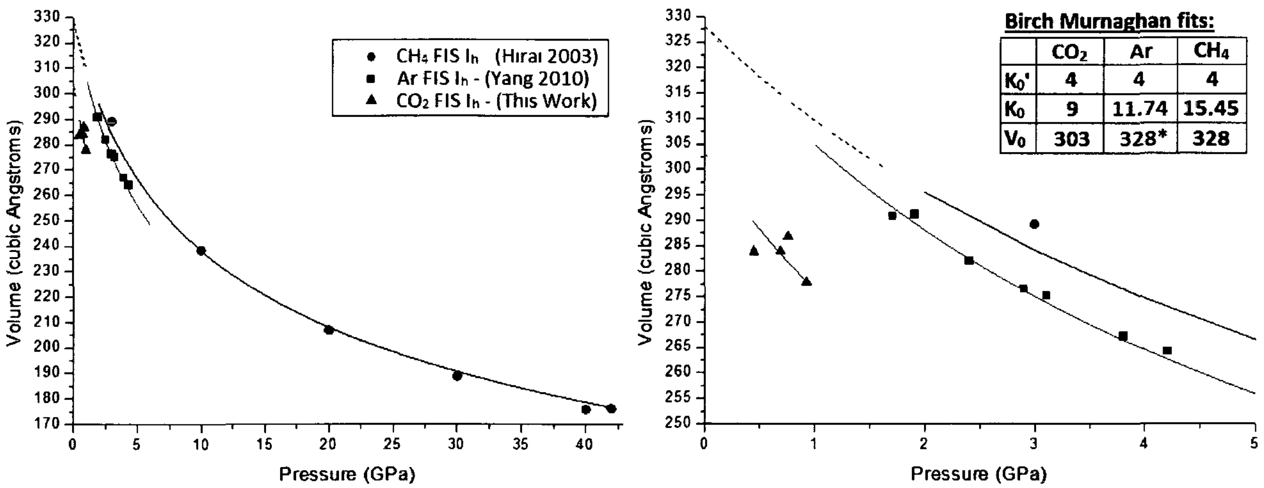

Birch Murnaghan fits:

	CO_2	Ar	CH_4
K_0'	4	4	4
K_0	9	11.74	15.45
V_0	303	328*	328

Figure 5.3 – Comparison of FIS I_h unit cell volumes vs pressure for three different systems. Actual data points are shown as well as Birch-Murnaghan equation of state fits proposed by the authors [66, 97]. The left graph shows the entire range of data points used to fit the EOS to methane FIS while the right graph shows the low pressure region of interest. The volume parameter marked with an asterisk was altered to better fit the author's data. Uncertainty on V, V_0, K_0, and P for CO_2 FIS I_h are 2 Å^3, 10 Å^3, 2 GPa, and 0.4 GPa respectively.

In addition to the data points, the Birch-Murnaghan equations of state proposed by the authors are overlaid as solid lines within the stability region and as dotted lines below and towards V_0. Bulk moduli values, K_0, and their corresponding pressure derivatives, K_0', given by Hirai *et al.*[66] and Yang *et al* [97] were unchanged; V_0 was changed, however, from 317 Å^3 to 328 Å^3 (as reported in the work by Yang et al. [97]) to better fit the data. Since V_0 was not given by Hirai et al. [66], the value which fit their data best was determined. Incidentally, this value was also 328 Å^3. In the present work, a bulk modulus of 9 GPa (while keeping K_0' fixed to 4) was proposed to fit CO_2 FIS I_h, along with a V_0 of 303 Å^3. Proposal of an equation of state based on four data points that, according to Figure 5.3, do not all follow a trend is perhaps premature, but it was done nevertheless to complete the description of this system using the evidence available. More x-ray diffraction data of this phase can be used to improve the equation of state in the future. To compare compression trends, V/V_0 is graphed in Figure 5.4 for the three systems.

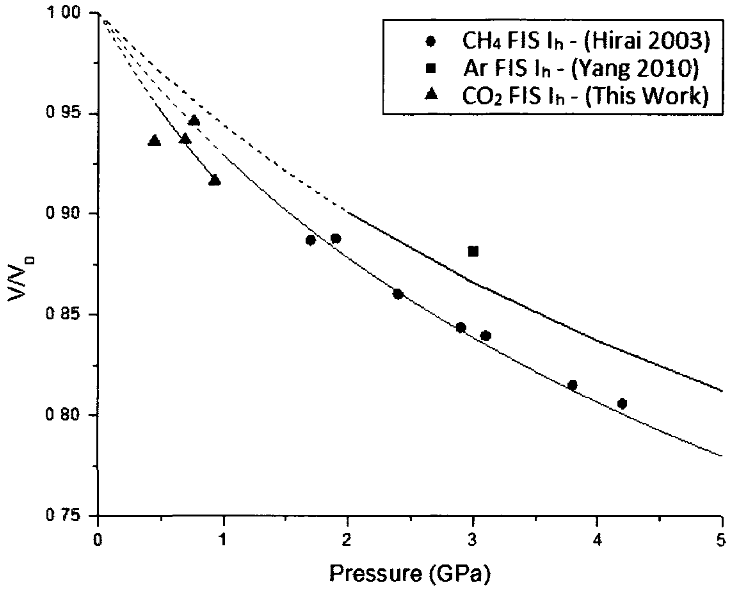

Figure 5.4 - Comparison of FIS I_h V/V_0 vs. pressure graph for three different systems.

From Figure 5.4, it is clear that the FIS I_hs have slightly different compression rates compared to the sI hydrates in Figure 5.1 (right), which were nearly identical for the three systems compared. As mentioned before in the case of the sI hydrates, the fact that H_2O forms the "backbone" of these structures and that they should not be affected much by the guest species, equations of state would be expected to be fairly close. Owing to the fact that methane FIS I_h is fit up to 42 GPa, it definitely has the most reliable equation of state in Figure 5.4. The high compression rate of CO_2 FIS I_h is problematic and could be explained by a systematic error in pressure measurement (to be discussed in the following sections). A shift of 0.4 GPa could very possibly bring the compression rate of CO_2 FIS I_h closer to the others in Figure 5.4.

The guest diameter may not necessarily be the only factor behind the appearance and stability range of the FIS I_h. As seen in Figure 3.3, the FIS I_h consistently appeared first at higher pressures and then lasted to higher pressures as the guest diameter increased from the case of argon to that of methane. This trend was broken with xenon, where no FIS I_h was found before dissociation, and now in carbon dioxide where the structure appears first at a much lower pressure than all the others.

For the sequestration of CO_2, the FIS I_h would provide a 1:2 ratio of CO_2 to H_2O in terms of storage capacity; however, the pressures involved may not be practical. The formation pressure of 0.45 GPa found in this work is equivalent to almost 5 times the pressure found at the deepest part of the Pacific ocean. Achieving these pressures in a large volume storage tank and preserving the compounds formed would prove challenging if not impossible.

5.3 - Unknown Phases

After indexing the CO_2 FIS I_h phase, many diffraction peaks were left (as many as 21) and could not be attributed to this phase or any hydrate or constituent phase previously encountered at lower or higher pressures in this system. This leads to the conclusion that at least one unknown phase coexists with CO_2 FIS I_h between 0.45 GPa and 0.94 GPa. At 0.70 GPa, when solid CO_2 begins to show its presence in the diffraction patterns, the number and position of these unknown peaks changes noticeably as shown in Table 4.4. This could mean that the first unknown phase transforms into a second unknown phase. As a result of this observation, a distinction is made in Figure 5.5 that two separate unknown phases most likely exist at high pressure. Of course, one should note that without conclusive indexing, one can only speculate at this point. Nevertheless, extra reflections in the x-ray diffraction pattern have been systematically observed under those pressure and temperature conditions.

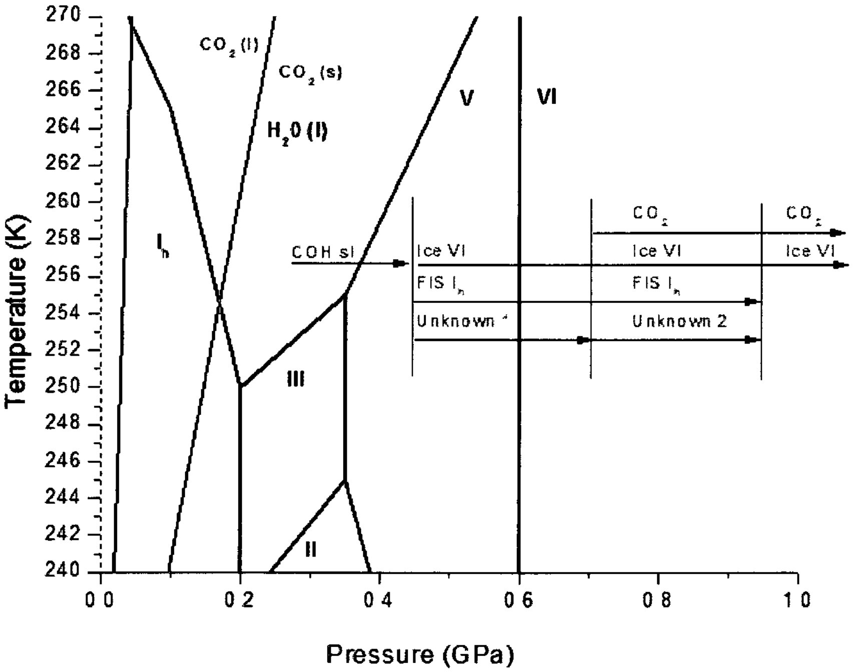

Figure 5.5 - Observed phases in the CO_2-H_2O system represented as arrows and overlaid by the phase diagram of pure H_2O [28] and CO_2 [79]. The vertical height of the green bars is representative of the experimental temperature range. The sI CO_2 hydrate phase transforms into a phase mixture containing CO_2 FIS I_h and an unknown phase at 0.45 GPa. At 0.70 GPa the peaks of the unknown phase change enough to call this as a separate unknown phase. Beyond 0.95 GPa, CO_2 hydrate is unstable against the formation of its constituents. Uncertainty on pressure measurements is 0.4 GPa.

At 0.45 GPa, H_2O is occluded from the collapsing sI hydrate as the FIS I_h structure forms. According to Figure 5.5, the phase that H_2O must assume at this pressure is Ice V. The fact that Ice VI appears instead suggests that either the reference phase line for H_2O is incorrect, or the pressure measurements in this work are incorrect. Consultation with H_2O phase diagrams of others led to the conclusion that indeed the error stated on pressure measurements in this work must exceed 0.1 GPa and perhaps a larger systematic error should be considered. As mentioned before, this problem was also encountered during the analysis of CO_2 sI hydrate below 0.45 GPa. It is likely that this shift in pressure is related to incorrect temperature measurement. The accuracy in temperature measurement of the thermocouple was established to within ±1 K by testing its readings at the set temperatures of boiling N_2 (77K) and the ice point of water (273K). While the measurement itself is precise, it may not accurately represent the sample temperature as the thermocouple is actually positioned against the diamond anvil, outside the compression chamber of the DAC, and not against the sample. Furthermore, the temperature correction to pressure method adopted from the work by McCumber and Sturge [30] requires the exact temperature of the ruby, not the sample, to provide an accurate result. These were assumed to be the same in this work. The actual sample/ruby temperatures for all diffraction patterns taken in this work were likely overestimated. When the sample was taken out of the freezer and taken for a pressure measurement, there was likely a lag between the time it took to heat up the thermocouple hot junction and the actual sample in the compression chamber (and subsequently the ruby). An overestimation of 20K, for example, would yield, according to a calculation based the Equation 10 presented in Chapter 1, a pressure ~0.30 GPa higher than that actually recorded.

Another systematic error could have been introduced by the spectrograph used in pressure measurement at the CLS. The spectral calibration was only correct to within 0.05 nm. This would correspond to, at worst, a 0.1 GPa shift in pressure measurements.

Using these arguments, the previously stated bounds of uncertainty on temperature and pressure measurements can be updated to ±20K and ±0.4 GPa respectively. Within the new bound of uncertainty for pressure, the appearance of Ice VI at 0.45 GPa is plausible. A study of temperature gradients across diamond is needed in the configuration used in this experiment if these bounds are to be improved further.

As for the possible identity of the new phases found to coexist with FIS I_h, it is important to notice that at the 0.70 GPa transition point, solid CO_2 begins to appear. This abrupt appearance suggests that enclathrated CO_2 was occluded following a volume collapse in one of the hydrate structures. Two possible explanations for this observation are as follows: either the excess CO_2 arose from the decomposition of CO_2 FIS I_h, or it came from a transformation involving Unknown Structure 1. The first possibility could be substantiated by an examination of the change in relative intensity of diffraction peaks of the FIS I_h, CO_2 being occluded, and the Ice VI with increasing pressure. Unfortunately, the four data points obtained in the region of interest is not enough to reach any conclusions using this method. More x-ray diffraction patterns taken at different pressures within the region of interest could help explain the CO_2 occlusion.

As a second possibility, the excess CO_2 could have come from the transformation of Unknown Structure 1 into Unknown Structure 2, which seems more likely. The available structure candidates for the Unknown Structures, based on work on other clathrate hydrate systems found in the literature and on the phase diagram in Figure 5.5, are pure phases of H_2O (Ice II, III, or V), novel clathrate hydrates, other FISs (I_c, II), or a novel FIS. As shown in Chapter 4, the appearance of CO_2 sH hydrate as a dense phase in the CO_2-H_2O system could not be realized as attempts to index this phase failed. This in itself is an important result as theoretical work reported by Alavi *et al.* [3] concluded that this phase should be stable. If CO_2 hydrate indeed presents a sH phase, it does not exist within the pressure- temperature range explored and presented in this work. The pure phases of H_2O were also explored by attempting indexing, however no positive results were obtained. Attempts were also made using CRYSFIRE to generate new possible candidate unit cells based on the x-ray diffraction peaks identified to belong to the unknown phase. Again, no conclusive results were obtained. As mentioned in Chapter 1, using indexing software to test unit cells based on x-ray diffraction data that may contain peaks from multiple phases instead of just one is a difficult endeavour that is not guaranteed to produce results. More x-ray diffraction data of good quality, as well as better control of pressure and temperature, is needed to improve the chances in identifying these unknown phases.

5.4 – Dissociation into Ice VI and CO_2-I

Thirteen x-ray diffraction images taken between the pressures of 0.94 GPa and 2.15 GPa at 250 K were identified as containing only pure CO_2-I and Ice VI. Unit cell volumes vs. pressure are graphed in Figure 5.6, along with second-order Birch-Murnaghan equation of state fits. Fitting parameters are also given in Figure 5.6.

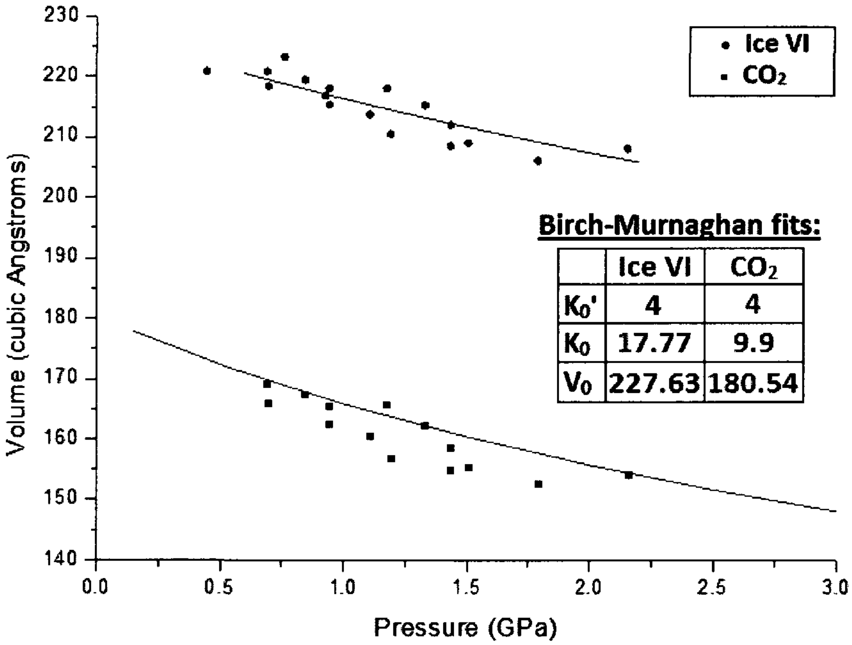

Figure 5.6 – Unit cell volume vs. pressure for Ice VI and CO_2-I observed throughout the course of the experiment. Data points of occluded material before and after complete dissociation of hydrates are included. Data is in agreement with Birch-Murnaghan equations of state (parameters in the inset table) based on other high pressure works on these pure substances [98-101]. Uncertainty for V and P data points are 2 Å^3 and 0.4 GPa respectively.

In general, compression data of the dissociated phases, namely, ice VI and CO_2-I, agree with published equations of state of those systems. The present data and published equations of state are presented in Figure 5.6. The minor scattering of data points about the fit lines can be attributed mostly to thermal fluctuations. Because the lattice parameter is affected by temperature, and because our exposures were taken over a 10 K temperature range, some deviation is expected. It should also be noted that the fit parameters were obtained from works of others who operated at slightly different temperature conditions. Parameters for CO_2-I, for example, were obtained at room temperature. This and the new error bounds established for this work account for the fact that the data points appear slightly lower than the fit line.

5.5 – Summary, conclusions and future work

Summary and conclusions

A systematic high pressure study of the CO_2–H_2O system was performed by powder x-ray diffraction at the Canadian Light Source's HXMA beamline. Analysis of x-ray diffraction patterns, taken at pressures ranging from 0.27 GPa to 2.5 GPa with temperatures ranging from 250K to 260K, indicates that at the lowest pressures, the system adopts a clathrate hydrate sI structure with a CO_2 occupancy of 100% for small cages and 10% for large cages, resulting in a hydration number of 17.86. Comparison to the work of others [86, 96] leads to the conclusion that differences in methods of sample synthesis contributed to the unfavorable hydration number in this work. As far as CO_2 sequestration is concerned, it is concluded that achieving a low hydration number for a sI hydrate is possible for CO_2 when a more rigorously constrained synthesis procedure is followed.

Above 0.45 GPa, the sI clathrate breaks down into an orthorhombic "filled ice" structure resembling Ice I_h which survives up to 0.94 GPa. This "filled ice" structure has been observed for the case of other gas hydrates at high pressure. Although not a "clathrate" structure, FIS I_h is known to hold a guest gas in the ratio of 1 guest to 2 H_2O molecules [10]. Occlusion of H_2O from the sample into Ice VI at 0.45 GPa is consistent with a large reduction in unit cell volume. This is indeed observed when clathrate sI transforms into FIS I_h. Alongside the CO_2 FIS I_h found in this study, another phase exists that could not be identified. The fact that the occlusion of pure CO_2-I from these structures occurs abruptly at 0.70 GPa suggests one of two possibilities. The first possibility is that the unknown phase transforms into a second unknown phase with a smaller volume, occluding CO_2-I in the process. Based on observed trends in other hydrate systems, it was suggested that these unknown phases must be either pure phases of H_2O (Ice II, III, or V), novel clathrate hydrates, other FISs (I_c, II), or a novel FIS, none of which could be indexed.

The second possible explanation for the appearance of pure CO_2-I at 0.70 GPa might be that the CO_2 FIS I_h begins to decompose at this pressure, releasing its guest CO_2 molecules in the process. Above 0.94 GPa the sample completely dissociates into Ice VI and CO_2-I. The observed unit cell volumes and the Birch-Murnaghan equations of state for these pure phases agree for both Ice VI and CO_2-I.

Based on the present work, the phase diagram for the CO_2-H_2O system can be revised from Figure 3.2 to Figure 5.7. Likewise, the summary of the phases adopted by gas hydrates as a function of gaseous species diameter (Figure 2.4), can now be revised (Figure 5.8).

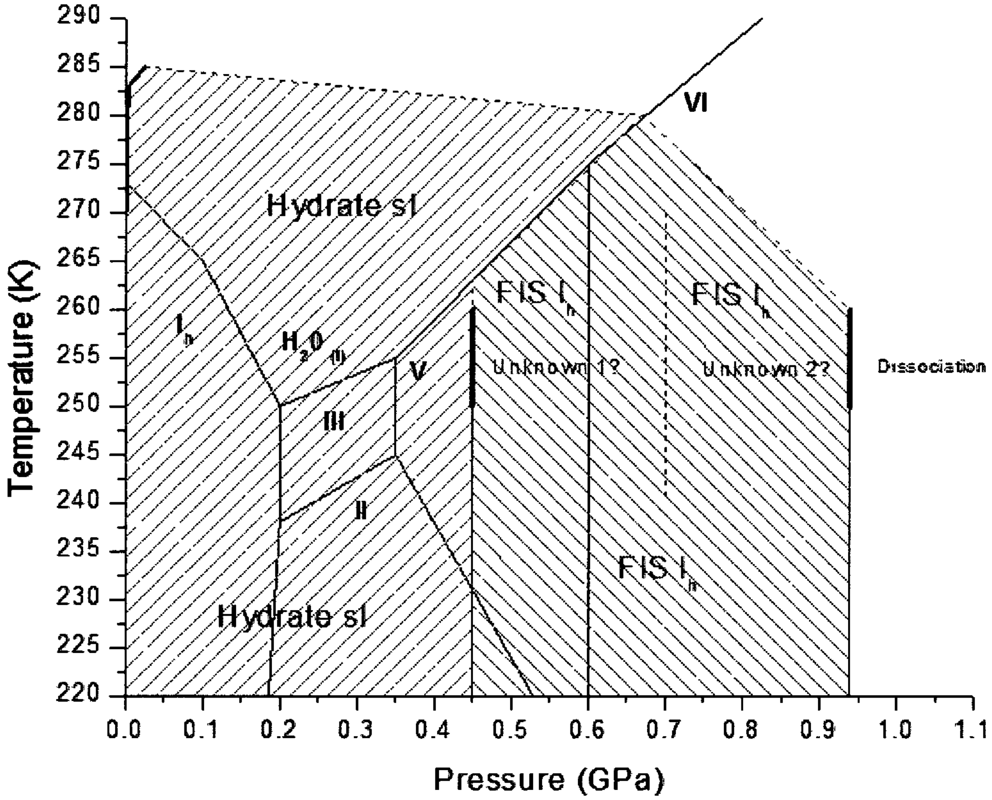

Figure 5.7 – New proposed phase diagram for the CO_2-H_2O system. Thin black lines represent the phase diagram for pure H_2O. The solid blue line represents the known dissociation boundary for CO_2 hydrate sI. Thick solid light green lines represent new phase boundaries of CO_2 FIS I_h. Dotted lines represent extrapolations. The dark green dotted line at 0.7 GPa is the proposed phase boundary between two unidentified phases coexisting with FIS I_h. Dissociation occurs at 0.94 GPa in this system.

Figure 5.7 provides a clearer view of the CO_2-H_2O system, and is a step forward from what was done by Honda *et al.* [77]. Because our study is incomplete, the proposed new phase lines should be considered as tentative. The coexistence of the CO_2 FIS I_h phase with two yet unidentified structures may have been the reason why Honda *et al.* [77] were unable to proceed in their study. In contradiction to the study by Alavi *et al.* [3], it appears that the CO_2 sH phase does not exist, or at least not in the pressure and temperature range explored in this work. This does not bode well for the sequestration of CO_2 in hydrate form. Even if one of the unknown phases shown in Figure 5.7 turns out to contain CO_2 with a low hydration number, the stability pressure may already be too high for practical use. The option of using CO_2 sI hydrate as a means for sequestration despite its higher hydration number may still be practical as full cage occupancy can be realized by using specific synthesis procedures.

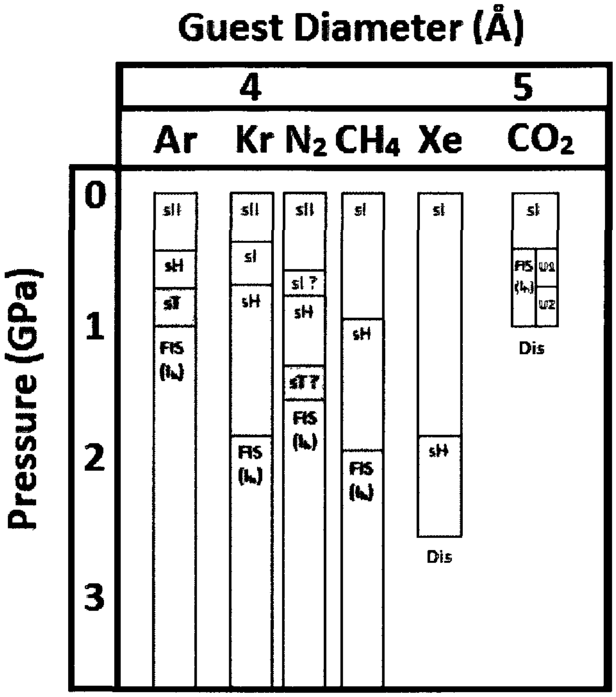

Figure 5.8 - Guest species (atoms or molecules) shown with increasing diameter and the hydrate structures they adopt as a function of increasing pressure. The structures found in this work for the CO_2-H_2O system are included. Clathrate hydrates involved are the cubic structure I (sI), cubic structure II (sII), hexagonal structure (sH), and the tetragonal structure (sT). The filled ice structure resembling Ice I_h is also indicated (FIS I_h). Two unknown structures are labeled (U1) and (U2). Systems that dissociate in the shown pressure range are labeled (Dis).

Future Work

More work is required to clarify the behaviour of this system at high pressures. The first major issue is that of the unknown structure(s) that exist alongside the FIS I_h. More x-ray diffraction work is necessary in the pressure region 0.45 to 0.94 GPa in order to aid in their identification. The use of a cryostat with adequate temperature control and regulation and a diamond anvil cell with fine pressure control (by a pressure membrane) would aid in achieving smaller pressure steps and allow for longer exposure times without the need to re-cool the cell. With better x-ray diffraction images in this region the unknown phases stand a better chance of being sorted out.

The second issue arising from discussion and comparison to works of others is the accuracy of pressure and temperature measurements. Despite stated values of uncertainty, pressure measurements via the ruby fluorescence method in the sub 1 GPa region are prone to error. In situations where the temperature is constantly changing, such as this work, the chance of error is magnified because a temperature correction to the pressure must be applied. The fact that the thermocouple hot junction used to measure the temperature is not in direct contact with the sample itself (and the rubies in the sample) is likely to cause a large error in the stated values for the pressure. New error bounds were estimated to be ±20 K and ±0.4 GPa for this work. A study of the temperature change across a DAC anvil is needed to better estimate these errors.

CO_2 hydrate was studied in the present work between 250 K and 260 K. The fact that certain structures like clathrate sH were not discovered in this work for CO_2 may be simply explained by the fact that it does not exist in this temperature region. It would be useful to perform x-ray diffraction along the isotherms closer to 270 K as well as below 250 K to see if any new structures arise. For this, a cryostat with good temperature control would be necessary.

In all pressure regions, this system would benefit from a Raman spectroscopy study to pinpoint transition pressures. As mentioned before, the vibrational modes characteristic of CO_2 hydrate sI are very similar to those of pure CO_2, and thus care would be required to ensure that the sample remains pure and at the correct temperature conditions. At higher pressures, after pure CO_2-I extrudes from the FIS I_h structure at ~0.7 GPa, Raman signals from an enclathrated CO_2 molecule may prove to be indistinguishable from the pure CO_2-I if care is not taken. If this is the case, perhaps another complimentary method would be appropriate.

Chapter 6 - Structural phase transition in dickite at high pressure and room temperature

6.1 - Introduction to dickite

Making up almost 90% of the Earth's crust, silicate minerals are a very broad category of materials classified according to their structure. Dickite belongs to the clay mineral group of the phyllosilicates, or "sheet silicates", which assemble as parallel sheets of silicate groups. The clay mineral group is distinguished by either a 1:1 stacking of tetrahedral and octahedral sheets of material, or a 2:1 stacking per layer. Dickite belongs to a further sub-group called the Kaolin group, which has a 1:1 stacking and the chemical formula $Al_2Si_2O_5(OH)_4$. The Kaolin group can achieve this sheet stacking at least 12 different ways, [102] leading to the possibility of many polytypes with the same chemical formula, but with a different structure. Only three polytypes, however, are energetically favourable and found in nature: kaolinite, dickite and nacrite. [103]

The study of clay minerals is immensely important because they control and direct most physical, biological, and chemical reactions that occur in subsurface environments. Clay minerals play a crucial role in structural stability of soils, influence water regulation, and are thought to be important in triggering deep-focus earthquakes [104]. The hydrophobic/hydrophilic duality of clay minerals leads to their interaction with a wide range of solutes. Proteins bound to clay minerals regulate biological activity in soils and provide microbal nutrition [105]. In fact, nearly all inorganic and organic solutes found in soil are found to interact in some way with this group of silicates [104].

The following section describes a powder x-ray diffraction and Raman spectroscopy study of St. Claire Dickite (dickite originating from St. Claire, Pennsylvania is known for its quality by mineralogists) subjected to pressures as high as 18.76 GPa at room temperature. Two structural phase transitions are observed, one between 2.20 GPa and 2.30 GPa and the second between 8.18 GPa and 8.48 GPa. To our knowledge, dickite has never been studied up to such large pressures.

6.2 - Powder x-ray diffraction of dickite

Two samples of St. Claire Dickite, prepared from finely ground single crystals, were loaded into DACs with a pressure transmitting medium consisting of methanol:ethanol:water in the proportion of 16:3:1 by volume and brought to the CLS HXMA beamline to carry out powder x-ray diffraction. The first sample was studied up to 14.57 GPa at room temperature (295K), and the second up to 18.76 GPa at 295 K. Selected x-ray diffraction patterns are shown with increasing pressure for sample 1 in Figure 6.1.

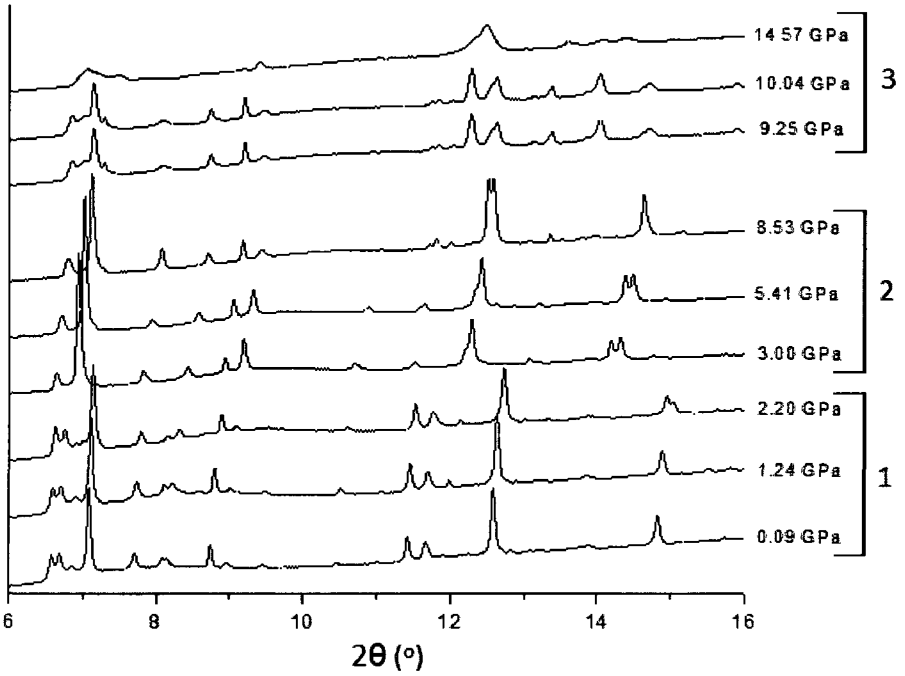

Figure 6.1 – Powder x-ray diffraction patterns of St. Claire Dickite from sample 1. The changes observed in the x-ray diffraction patterns indicate a sequence of three different phases labeled 1-3.

Figure 6.1 shows that three clear phases exist for dickite up to 14.57 GPa. The first transition occurs between 2.20 GPa and 3.00 GPa according to Figure 6.1. This transition has been previously observed and described in the work of Johnston *et al.* [103] The structure of dickite at low pressures is monoclinic, with the space group cc. In this work, indexing was used to confirm the identity of the phases of dickite observed initially by Johnston *et al.* [103] The indexing of phase 1 is shown in Figure 6.2, and the peak data is given in Table 6.1.

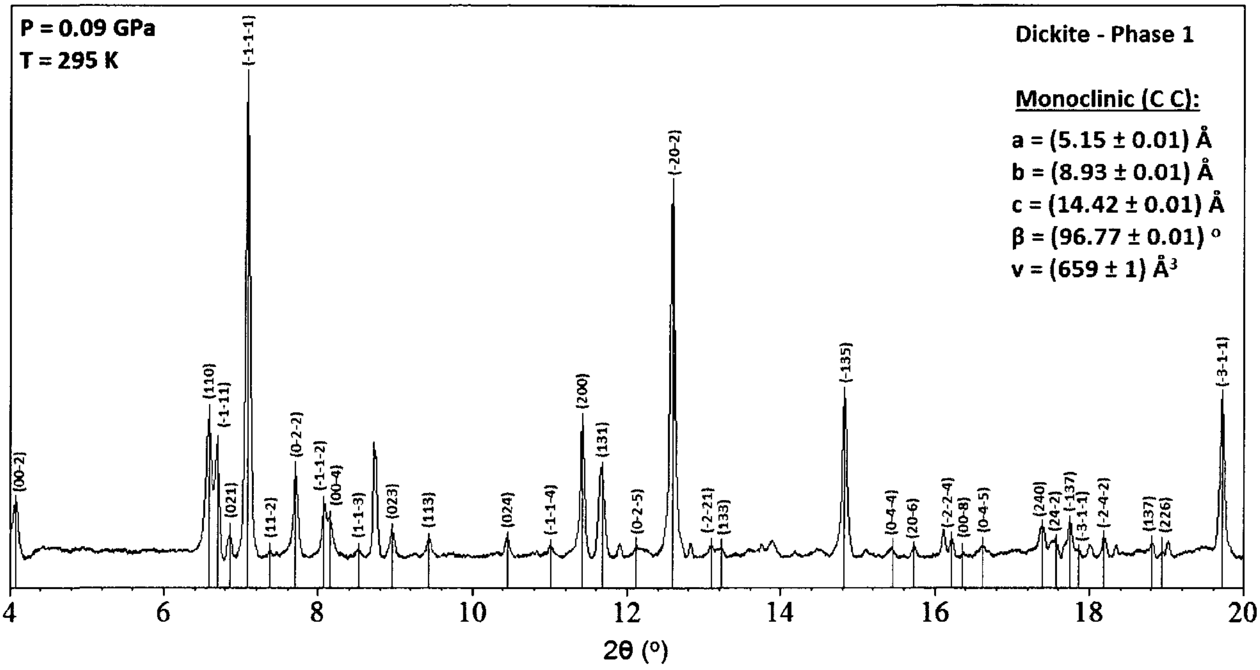

Figure 6.2 – Indexing of x-ray diffraction pattern recorded from dickite's intitial phase at 0.09 GPa at room temperature. Note the x-ray diffraction pattern has been background subtracted. The unit cell is monoclinic with the space group cc. The lattice parameters are a = (5.15 ± 0.01) Å, b = (8.93 ± 0.01) Å, c = (14.42 ± 0.01) Å, with angle β = (96.77 ± 0.01) °, giving a unit cell volume v = (659 ± 1) Å^3.

The indexing in Figure 6.2 and the difference between expected and observed d-spacings in Table 6.1 shows that the unit cell proposed for dickite by Newnham and Brindley [106] is confirmed in this work. This phase persists up to 2.20 GPa, above which it transforms into another monoclinic structure with the same space group (cc). The indexing of phase 2 is shown in Figure 6.3, and the peak data is shown in Table 6.2.

(hkl)	$2\theta_{obs}$ (°) ± 0.001	d_{obs} (Å) ± 0.01	d_{calc} (Å) ± 0.002	(d_{calc}- d_{obs}) (Å) ± 0.01
0 0-2	4.074	7.16	7.158	-0.01
1 1 0	6.576	4.44	4.438	-0.01
-1-1 1	6.688	4.36	4.367	0.01
0 2 1	6.849	4.26	4.263	0.01
-1-1-1	7.083	4.12	4.122	-0.01
1 1-2	7.397	3.95	3.958	0.01
0-2-2	7.706	3.79	3.789	0.01
-1-1-2	8.079	3.61	3.610	-0.01
0 0-4	8.149	3.58	3.579	-0.01
1-1-3	8.519	3.43	3.430	0.01
0 2 3	8.961	3.26	3.261	0.01
1 1 3	9.439	3.09	3.096	0.01
0 2 4	10.455	2.79	2.793	-0.01
-1-1-4	11.004	2.66	2.656	0.01
2 0 0	11.421	2.56	2.557	-0.01
1 3 1	11.667	2.50	2.507	0.01
0-2-5	12.120	2.41	2.410	-0.01
-2 0-2	12.583	2.32	2.323	-0.01
-2-2 1	13.091	2.23	2.228	-0.01
1 3 3	13.223	2.21	2.219	0.01
-1 3 5	14.827	1.97	1.973	-0.01
0-4-4	15.448	1.89	1.895	0.01
2 0-6	15.736	1.86	1.857	-0.01
-2-2-4	16.225	1.80	1.805	0.01
0 0-8	16.375	1.79	1.790	0.01
0-4-5	16.624	1.76	1.761	-0.01
2 4 0	17.397	1.68	1.682	-0.01
2 2 5	17.515	1.67	1.673	0.01
24-2	17.575	1.67	1.666	-0.01
15-2	17.682	1.66	1.656	-0.01
-137	17.755	1.65	1.649	-0.01
-3-1-1	17.873	1.64	1.641	0.01
-2-4-2	18.200	1.61	1.610	0.01
137	18.825	1.56	1.557	0.01
226	18.926	1.55	1.548	-0.01
-3-31	19.719	1.49	1.487	0.01
33-3	20.147	1.46	1.456	0.01
-2-2-7	20.481	1.43	1.433	0.01
-3-3-3	21.352	1.37	1.374	-0.01
-1-3-9	22.282	1.32	1.319	0.01
260	22.827	1.29	1.287	0.01

Table 6.1 - Miller indices, observed Bragg angles (2 θ), and d-spacings for diffraction peaks of St. Claire Dickite at 0.09 GPa and 295 K. The small differences between the expected and observed d-spacings indicate a good fit to the monoclinic structure.

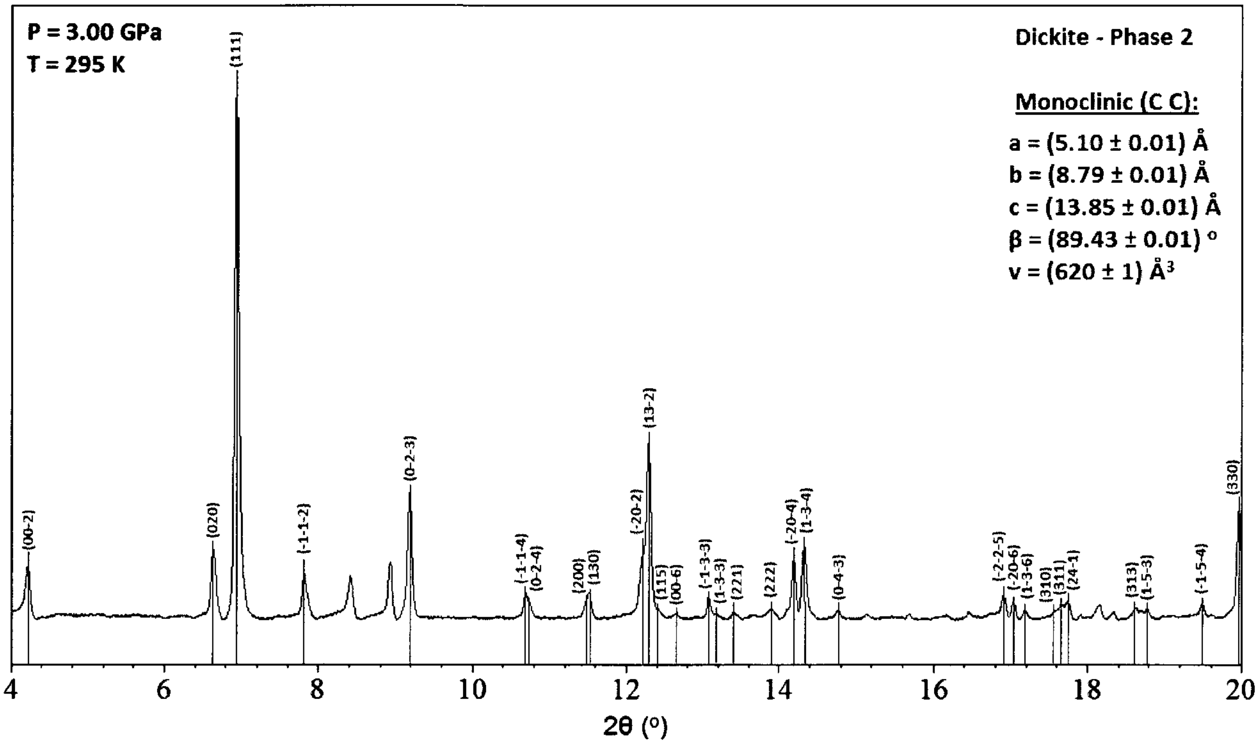

Figure 6.3 - Indexing of x-ray diffraction pattern recorded from dickite's second phase, at 3.00 GPa and 295 K. The unit cell is monoclinic with the space group cc, lattice parameters a = (5.10 ± 0.01) Å, b = (8.79 ± 0.01) Å, c = (13.85 ± 0.01) Å, angle β = (89.43 ± 0.01) °, and unit cell volume v = (620 ± 1) Å^3.

The indexing in Figure 6.3 and the difference between expected and observed d-spacings in Table 6.2 shows that the unit cell proposed for dickite by Johnston [104] is confirmed in this work. This phase persists up to 8.53 GPa according to Figure 6.1. This transition is interesting because dickite essentially retains its unit cell and space group across the boundary. An examination of the lattice parameters, beta angle, and volume as a function of pressure across the transition boundary show the nature of this transition. Figure 6.4 shows that the c lattice parameter experiences a sudden compression and the beta angle is reduced significantly. Johnston [104] explained this by postulating that one sheet in the structure "slips" onto the other and settles into a new configuration. This phenomenon is likely to occur in sheet silicates. Having the same formula as the lower pressure phase of dickite, this new phase can be considered a polytype of dickite.

(hkl)	$2\theta_{obs}$ (°) ± 0.001	d_{obs} (Å) ± 0.01	d_{calc} (Å) ± 0.002	(d_{calc}- d_{obs}) (Å) ± 0.01
0 0-2	4.210	6.93	6.925	-0.01
0 2 0	6.639	4.40	4.394	-0.01
1 1 1	6.937	4.21	4.211	0.01
-1-1-2	7.826	3.73	3.733	0.01
0-2-3	9.186	3.18	3.183	0.01
-1-1-4	10.686	2.73	2.734	0.01
0-2-4	10.733	2.72	2.720	-0.01
2 0 0	11.457	2.55	2.548	-0.01
1 3 0	11.514	2.54	2.540	0.01
-2 0-2	12.202	2.40	2.399	0.01
1 3-2	12.287	2.38	2.381	0.01
1 1 5	12.416	2.35	2.355	0.01
0 0-6	12.648	2.31	2.308	-0.01
-1-3-3	13.070	2.24	2.230	-0.01
1-3-3	13.172	2.22	2.221	0.01
2 2 1	13.392	2.18	2.180	-0.01
-2-2 1	13.442	2.18	2.174	-0.01
2 2 2	13.900	2.10	2.105	0.01
-2 0-4	14.191	2.06	2.062	0.01
1-3-4	14.321	2.04	2.043	0.01
0-4-3	14.765	1.98	1.984	0.01
-2-2-5	16.915	1.73	1.732	0.01
-2 0-6	17.039	1.72	1.719	0.01
1-3-6	17.190	1.70	1.704	0.01
3 1 0	17.585	1.67	1.668	0.01
3 1 1	17.667	1.66	1.658	-0.01
2 4-1	17.753	1.65	1.651	0.01
3 1 3	18.630	1.57	1.573	0.01
3 1-3	18.710	1.57	1.564	-0.01
1-5-3	18.781	1.56	1.562	0.01
-1-5-4	19.490	1.50	1.500	-0.01
3 3 0	19.963	1.47	1.469	0.01
-2 0-8	20.383	1.44	1.439	-0.01
-1-3-8	20.462	1.43	1.434	0.01
1-3-8	20.602	1.42	1.427	0.01

Table 6.2 - Miller indices, observed Bragg angles (2 θ), and d-spacings for diffraction peaks of St. Claire Dickite at 3.00 GPa and 295 K. The small difference between expected and observed d-spacings indicate a good fit to the monoclinic structure.

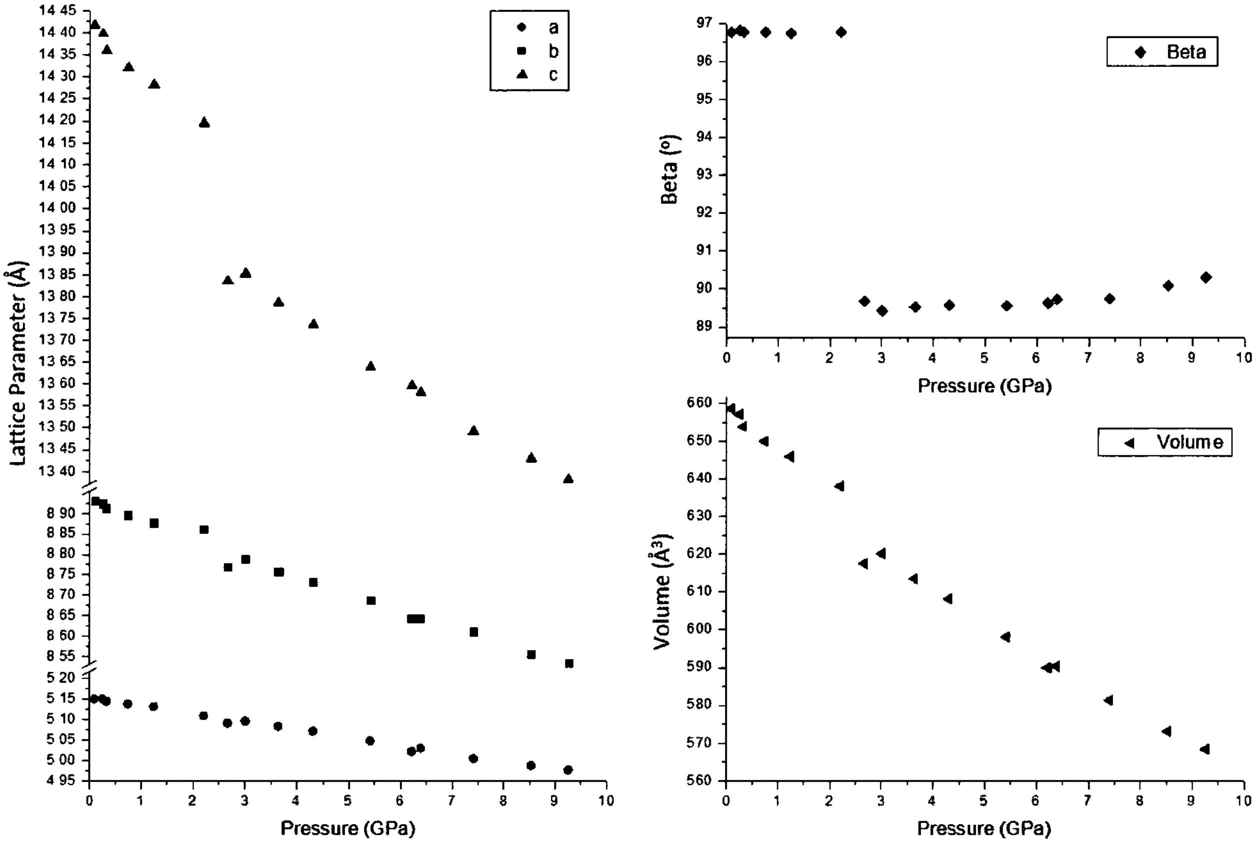

Figure 6.4 – Lattice parameters (left), beta angle (top right), and volume (bottom right) of St. Claire Dickite as functions of increasing pressure. The phase transition at 2.20 GPa can be described as a "layer-slipping", which occurs when one sheet settles onto another, causing the c-axis to suddenly compresses and beta angle to shrink. The reduction of the c lattice parameter naturally causes a reduced unit cell volume. Uncertainty for lattice parameters, β, V and P are 0.01 Å, 0.01 °, 1 Å^3 and 0.1 GPa respectively.

Above 8.53 GPa, a third phase was observed in this work. Unfortunately, a unit cell could not be found for this phase, so it is unclear whether this is another polytype of dickite or another structure entirely. The background subtracted diffraction pattern is shown in Figure 6.5, along an inset showing the raw pattern. The line shape is somewhat altered by the background subtraction, especially for the group of peaks around 7° (2θ). Peak positions are given in Table 6.3.

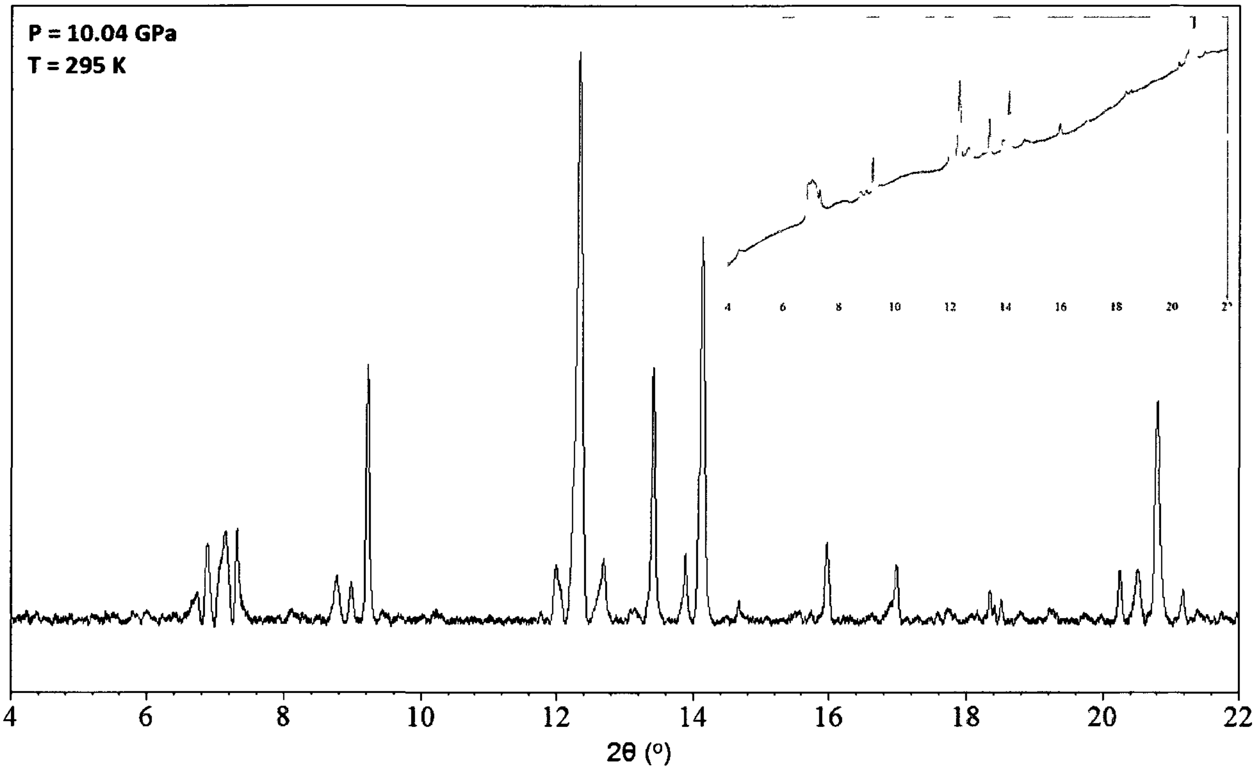

Figure 6.5 –Background subtracted powder x-ray diffraction pattern of dickite's unknown third phase recorded at 10.04 GPa and 295 K. Inset shows the pattern without background subtraction.

$2\theta_{obs}$ (°) ± 0.001	d_{obs} (Å) ± 0.01		$2\theta_{obs}$ (°) ± 0.001	d_{obs} (Å) ± 0.01
4.375	6.67		14.130	2.07
4.489	6.50		14.664	1.99
6.888	4.24		15.968	1.83
7.032	4.15		16.983	1.72
7.164	4.08		18.349	1.60
7.312	3.99		18.416	1.59
8.772	3.33		18.518	1.58
8.986	3.25		20.258	1.45
9.227	3.17		20.525	1.43
11.995	2.44		20.723	1.42
12.073	2.42		20.800	1.41
12.341	2.37		21.181	1.39
12.654	2.31		22.439	1.31
12.694	2.30		22.524	1.30
13.417	2.18		22.703	1.29
13.886	2.11		23.760	1.24

Table 6.3 - Observed Bragg angles (2 θ) and d-spacings for diffraction peaks of St. Claire Dickite's unknown third phase at 10.04 GPa and 295 K.

Despite not being able to identify this new phase, it should be pointed out that a few of the x-ray diffraction peaks from phase 2 appear in phase 3 (see Figure 6.1), suggesting that they are, perhaps, closely related. Without a further detailed analysis, phase 3 of dickite is most likely another possible polytype which can be characterized by a layer sliding.

6.3 - Raman spectroscopy of dickite

Raman spectroscopy experiments were performed at the *Laboratoire de physique des solides denses* (LPSD), in the Department of Physics, University of Ottawa on two samples of St. Claire Dickite (single crystals) loaded in DACs with a pressure transmitting medium consisting of methanol:ethanol:water in the proportion of 16:3:1 by volume. The first sample was studied closely from 0 to 6.55 GPa, while the other was studied in a higher pressure range from 6.65 to 12.32 GPa. The goal was to use Raman spectroscopy as a complimentary method to x-ray diffraction in order to better determine the exact transition pressures of the two observed phase changes in dickite. Samples were illuminated by a 532 nm light frequency-doubled YAG laser and spectrally analyzed by a 0.3 m spectrograph (Andor) equipped with a thermoelectrically cooled CCD. Two regions of interest in the Raman spectrum of dickite were studied as a function of pressure. The first was the OH vibration mode region, between 3580 and 3750 cm^{-1}, and the second was the lattice vibration mode region, between 100 and 1000 cm^{-1}. According to Johnston *et al.* [107], the OH region of dickite at low pressures is characterized by three bands. One, at 3623 cm^{-1}, represents an OH group located in between the Al-octahedral and Si-tetrahedral sheets. Two more bands at 3655 and 3708 cm^{-1} represent two OH groups located in the interlayer region.

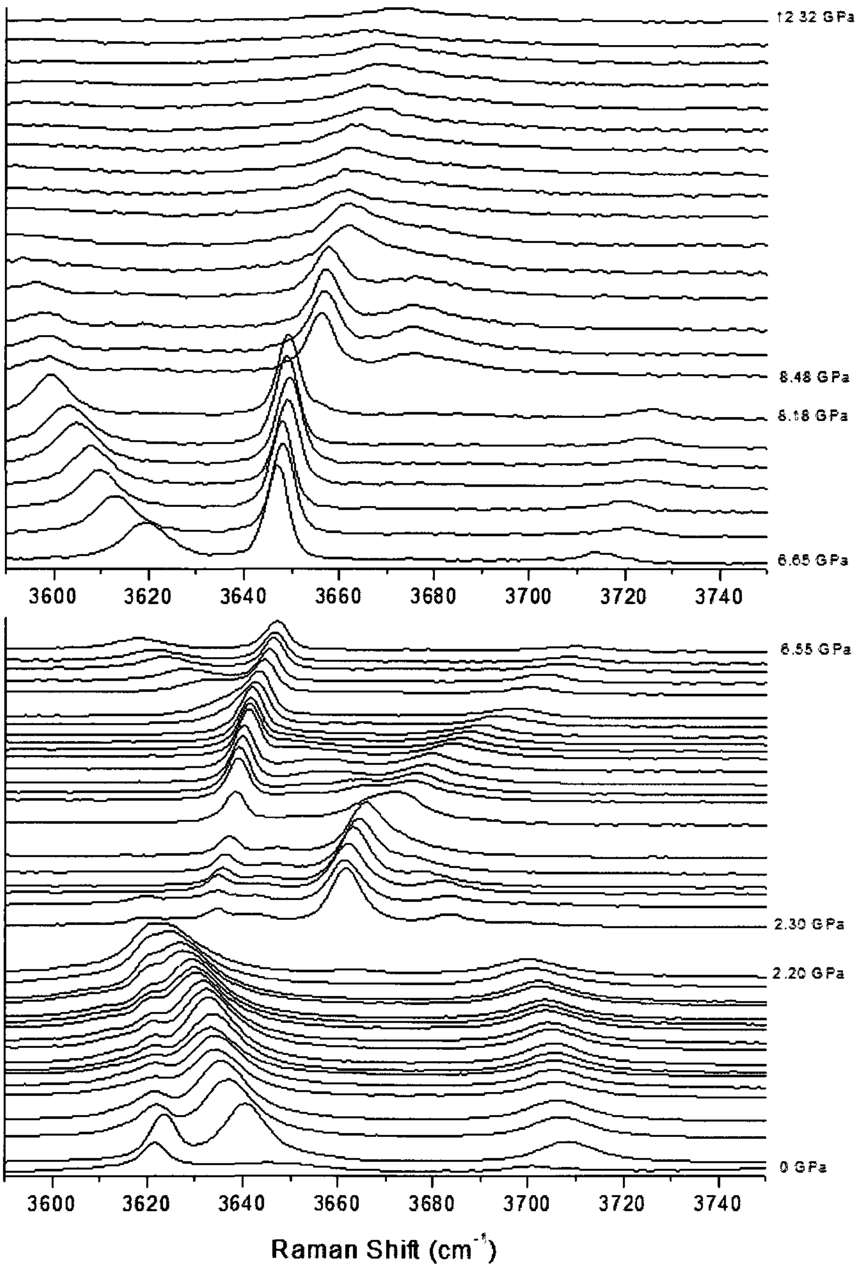

Figure 6.6 – Raman spectra of the OH stretching modes plotted as a function of pressure. In the first sample (bottom panel) a clear transition is observed between 2.20 GPa and 2.30 GPa. In the second sample (top panel), a clear transition is seen between 8.18 GPa and 8.48 GPa. Uncertainty on pressure measurements are 0.1 GPa.

In Figure 6.6, the Raman spectra in the OH region of dickite are plotted for both samples with increasing pressure. The three expected bands [107] are present and remain until 2.30 GPa is reached. Above 2.30 GPa, they suddenly disappear and are replaced by other bands. At 8.48 GPa, another transition occurs, as seen in Figure 6.6, identified by the disappearance of bands and appearance of new bands. In Figure 6.7, the band wavenumbers are graphed as a function of pressure and the two transitions are again seen.

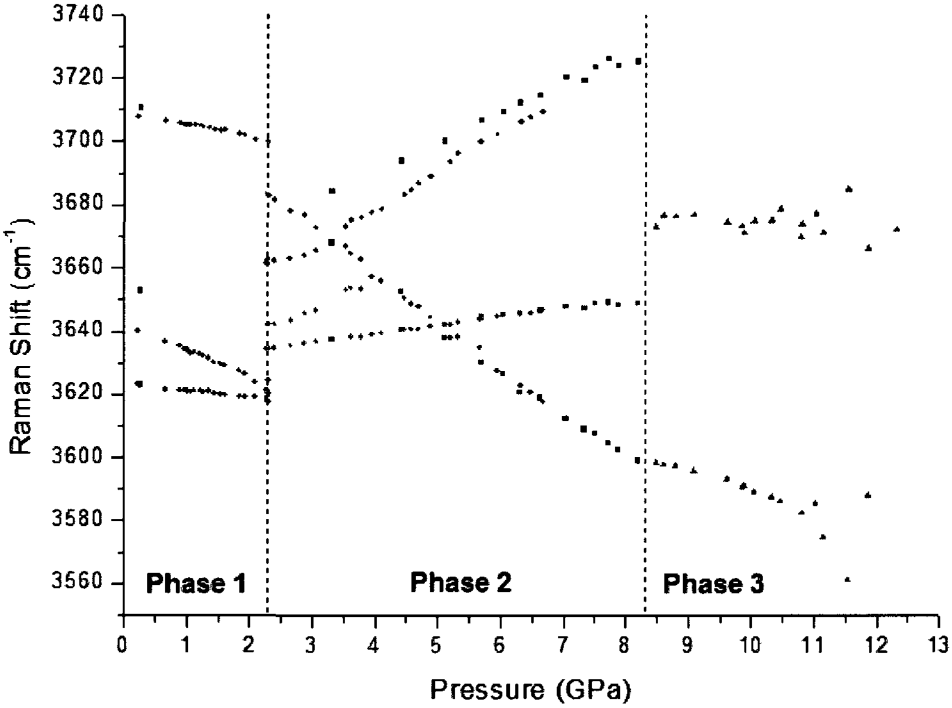

Figure 6.7 – Band wavenumber vs. pressure for the OH stretching modes of St. Claire Dickite. Two transitions are seen and marked with dotted vertical lines.

The second region of interest on the Raman spectrum is between 100 and 1000 cm^{-1} where the structural lattice modes appear. The spectra taken of this region are plotted in Figure 6.8, for both samples, with increasing pressure. The transitions are not as obvious in this region as they are in the OH region, so the spectra marking the border between phases are labeled with their respective pressures (between 2.20 GPa and 2.30 GPa, and between 8.18 GPa and 8.48 GPa). In Figure 6.9, the peak wavenumbers are graphed as a function of pressure and the two transitions are marked with dotted vertical lines. Small shifts in peak positions are observed for all modes at the transition points.

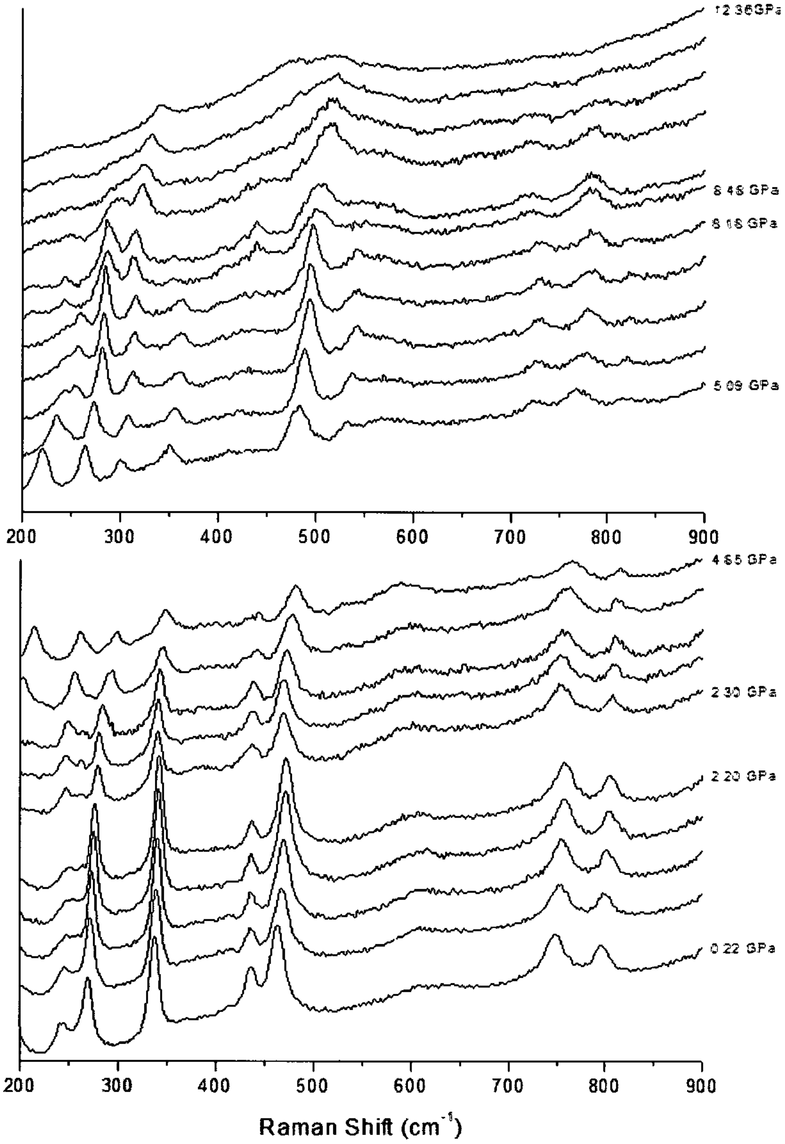

Figure 6.8 - Raman structural lattice modes overlaid as a function of pressure. Phase transitions are not as obvious as they were for the OH stretching modes, but can be marked by a slight down-shift in peak position. In the first sample (bottom panel) the transition occurs between 2.20 GPa and 2.30 GPa. In the second sample (top panel), the transition occurs between 8.18 GPa and 8.48 GPa. Uncertainty on pressure measurements are 0.1 GPa.

According to Johnston *et al.* [107], who did a vibrational study of single crystals of dickite in several different polarization orientations, the lattice mode region of dickite at low pressures is characterized by nine structural lattice modes at 223, 248, 271, 339, 437, 468, 525, 750, and 799 cm^{-1} and two OH bending modes at 847 and 921 cm^{-1} . Seven of these lattice modes are observed in our work (see Figure A.6, 0.22 GPa spectrum) while no OH- bending modes are observed. This corresponds exactly to the spectrum obtained by Johnston *et al.* [107] for illumination perpendicular to the (001) face This observation leads to the conclusion that our single crystals were also loaded in this orientation.

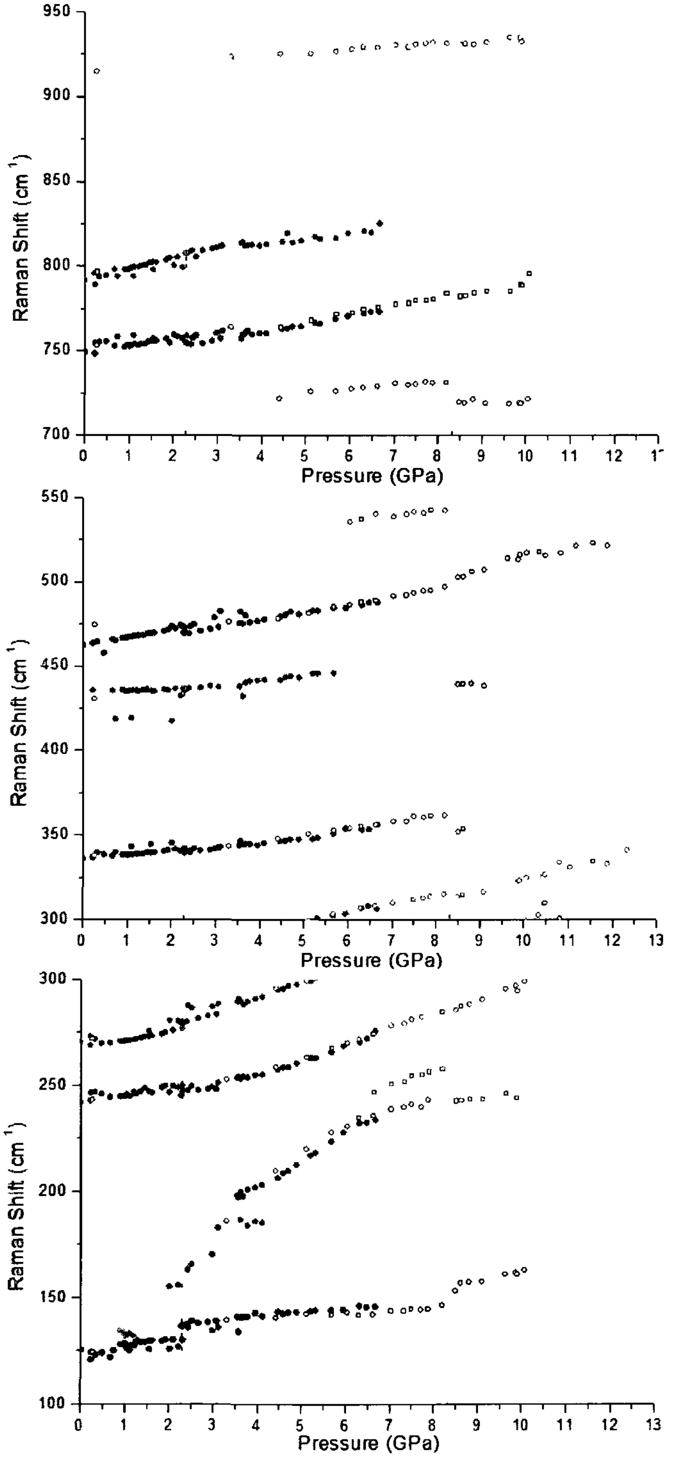

Figure 6.9 – Peak position vs. Pressure graph of the lattice modes of Ste. Claire Dickite. Two transitions are seen and marked with dotted vertical lines.

The three plots in Figure 6.9 show the evolution of the lattice modes with pressure through the two phase transitions. For each mode, a shift in peak position is observed at each transition point.

In summary, a high pressure x-ray diffraction and Raman study of St. Clair Dickite was performed using DACs. The purpose of this study was to verify an observed structural phase transition by Johnston *et al.* [103] and to search for any other possible transitions at higher pressures. The x-ray diffraction experiment done up to 18.76 GPa and 295 K confirmed two structural phase transitions, one at ~2.20 GPa and the second at ~8.18 GPa. The nature of the first transition was indeed, as described by Johnston *et al.* [103], a sudden compression in the c-axis of dickite's monoclinic structure. The second phase transition, although observed, could not be identified. Based on the Raman spectroscopy work done in the present work, the bounds placed by Johnston *et al.* [103] on the first phase transition (2.0 GPa to 2.5 GPa at 295 K) can be reduced down to between 2.20 GPa and 2.30 GPa at 295 K. The second phase transition can be localized between 8.18 GPa and 8.48 GPa at 295 K. This work is still in progress, but it is likely that the newly observed phase transition is to another polytype of dickite.

Licenses

The majority of figures and tables in this work were created by the author. Those that were taken from literature are listed in the table below along with their license reference number obtained from the publisher.

	Reference Number	License Provider	License Number
Figure 1.5	20	National Institute of Standards and Technology	None Provided
Figure 1.29	40	Elsevier	2551410998431
Figure 2.1	45	Taylor & Francis Group	None Provided
Figure 2.2	45	Taylor & Francis Group	None Provided
Table 2.1	53	American Chemical Society	2551421456231
Table 4.5	70	Springer Science + Business Media	2551430231089

References

[1] J. S. Loveday and R. Nelmes, Phys. Chem. Chem. Phys. **10**, 937 (2008).

[2] C. Marchetti, Clim. Change. **1**, 59 (1977).

[3] S. Alavi et al., J. Chem. Phys. **126**, 044703 (2007).

[4] M. von Stackelberg and H. R. Müller, J. Chem. Phys. **19**, 1319 (1951).

[5] J. S. Loveday et al., Phys. Rev. Lett. **87**, 215501 (2001).

[6] C. E. Weir et al., J. Res. Natl. Bur. Stand., Sec. A **63**, 55 (1959).

[7] J. S. Schilling, Physica C. **460**, 182 (2007).

[8] T Matsuoka and K. Shimizu, Nature **458**, 186 (2009).

[9] I. D. H. Oswald et al., High Pressure Res. **30**(2), 280 (2010).

[10] J. S. Loveday et al., Nature **410**, 661 (2001).

[11] H. Davy, Philos. Trans. R. Soc. London **101**, 1 (1811).

[12] F. D. Murnaghan, Proc. Natl. Acad. Sci. USA. **30**, 244 (1944).

[13] J. S. Smith. "A high-pressure study of the heavy alkaline earth hydrides." PhD thesis. U. of Ottawa, ON (2009).

[14] V. N. Zharkov and T. V. Gudkova. "Modern models of giant planets." High-Pressure Research: Application to Earth and Planetary Sciences. Eds. Y. Syono and M. H. Manghnani. Tokyo: Terra Scientific Publishing, 393 (1992).

[15] J. I. Lunine and D. J. Stevenson, Icarus **70,** 61 (1987).

[16] W. J. Nellis, Planet. Space Sci. **48**, 671 (2000).

[17] C. G. Sammis, Prog. Mat. Sci. **46**, 231 (2001).

[18] W. A. Basset, High Pressure Res. **29**(2), 163 (2009).

[19] http://nobelprize.org/nobel_prizes/physics/laureates /1946/bridgman.html

[20] G. J. Piermarini, J. Res. Natl. Inst. Stand. Technol. **106,** 889 (2001).

[21] Serge Desgreniers, personal communication (2010).

[22] V. E. Bean et al., "Toward an international practical pressure scale: An AIRTRAPT task group report." Proceedings of the Xth AIRTRAPT International High Pressure Conference on Research in High Pressure and Technology. Amsterdam, the Netherlands, July 8-11, 144 (1985).

[23] R. A. Forman et al., Science **176**, 284 (1972).

[24] H. K. Mao et al., J. Appl. Phys. **49**, 3276 (1978).

[25] H. K. Mao et al., J. Geophys. Res. **91**, 4673 (1986).

[26] A. Dewaele et al., Phys. Rev. B **78**, 104102 (2008).

[27] K. Syassen, High Pressure Res. **28**(2), 75 (2008).

[28] B. Minceva-Sukarova et al., J. Phys. C: Solid State Phys. **17**, 583 (1984).

[29] Omega Engineering. *The Temperature Handbook*, Vol. MM, 21st Century Edition. Stamford: Omega Press, Z-204 (1999).

[30] D. McCumber and M. Sturge, J. Applied Phys. **34**(6), 1682 (1963).

[31] J. I. Langford and Daniel Louër, Rep. Prog. Phys. **59**, 131 (1996).

[32] J. Smith and S. Desgreniers, J. Synchrotron. Rad. **16**, 83 (2009).

[33] http://nist.gov/srm

[34] A. P. Hammersley, ESRF Internal Report, EXP/AH/95-01, FIT2D V6.r Reference Manual V1.18 (1995).

[35] S. Desgreniers and K. Lagarec, J. Appl. Crystallogr. **27**, 432 (1994).

[37] R. Shirley, The CRYSFIRE System for Automatic Powder Indexing: User's Manual, The Lattice Press, Guildford, Surrey GU2 7NL, England, 2000.

[37] W. Kraus and G. Nolze, PowderCell for Windows (Version 2.4), Federal Institute for materials Research and Testing Rudower Chanssee 5, 12489, Berlin, Germany.

[38] H. M. Rietveld, J. Appl. Crystallogr. **2**, 65 (1969).

[39] J. Rodriguez-Carvajal, Physica B **192**, 55 (1993).

[40] H. Shimizu et al., Chem. Phys. Lett. **368**, 132 (2003).

[41] E. G. Hammerschmidt, Ind. Eng. Chem. **26**, 851 (1934).

[42] M. von Stackelberg and H. R. Müller, Z. Electrochem. **58**, 25 (1954).

[43] J. A. Ripmeester et al., Nature **325**, 135 (1987).

[44] G. A. Jeffrey, Inclusion Compounds Vol. 1, London: Acad. Press. 135 (1984).

[45] V. Y. Komarov et al., Crystallogr. Rev. **13**(4), 257 (2007).

[46] K. W. Allen and G. A. Jeffrey, J. Chem. Phys. **38**, 2304 (1963).

[47] S. R. Gough et al., Can. J. Chem. **52**, 3193 (1974).

[48] S. Brownstein et al., J. Chem. Phys. **46**, 1454 (1967).

[49] J. L. Schlenker et al., Nature **294**, 240 (1981).

[50] C. Cros and M. Pouchard, C. R. Chimie **12**, 1014 (2009).

[51] W. L. Vos et al., Phys. Rev. Lett. **71**, 3150 (1993).

[52] R. J. Speedy et al., J. Phys. Chem. **91**, 909 (1987).

[53] E. D. Sloan. Clathrate Hydrates of Natural Gases, 2nd Edition. New York: Marcel Dekker (1998).

[54] V. R. Belosudov et al., Izv. Akad. Nauk SSSR, Ser. Khim. **6**, 49 (1989).

[55] A. V. Kurnosov et al., Dokladny Phys. Chem. **381**, 303 (2001).

[56] A. V. Kurnosov et al., Angew. Chem. Int. Ed. **43**, 2922 (2004).

[57] Y. A. Dyadin et al., Mendeleev Commun. **6**, 44 (1996).

[58] Y. A. Dyadin et al., Mendeleev Commun. **7**, 32 (1997).

[59] Y. A. Dyadin et al., Mendeleev Commun. **7**, 74 (1997).

[60] Y. A. Dyadin et al., Mendeleev Commun. **9**, 209 (1999).

[61] A. Demirbas, Energ. Convers. Manage. **51**, 1547 (2010).

[62] S. Solomon et al., Climate Change 2007: The Physical Science Basis. Contribution of Working Group I to the Fourth Assessment Report of the Intergovernmental Panel on Climate Change. Cambridge Univ. Press, Cambridge, UK (2007).

[63] C. Marchetti, Clim. Change. **1**, 59 (1977).

[64] R. Susilo et al., Fluid Phase Equilibr. **263**, 6 (2003).

[65] H. Hirai et al., J. Phys. Chem. Solids **65**, 1555 (2004).

[66] H. Hirai et al., Phys. Rev. B **68**, 172102 (2003).

[67] H. Hirai et al., J. Phys. Chem. B **106**, 11089 (2002).

[68] H. Shimizu et al., J. Phys. Chem. B **106**, 30 (2002).

[69] J. S. Loveday et al., Can. J. Phys. **81**, 539 (2003).

[70] A. Y. Manakov et al., J. Incl. Phenom. Macro. **48**, 11 (2004).

[71] W. L. Mao et al., Science, **297**, 2247 (2002).

[72] W. L. Vos et al., Chem. Phys. Lett. **257**, 524 (1996).

[73] S. Sasaki et al., J. Chem. Phys. **118**, 7892 (2003).

[74] C. Sanloup et al., PNAS **99**, 25 (2002).

[75] S. Desgreniers, personal communication (2010).

[76] D. Londono et al., Nature **332**, 141 (1988).

[77] M. Honda et al., Proceedings from the High Pressure Conference of Japan, **18**, 14 (2008).

[78] S. V. Wrobelski, Compt. Rend. **94**, 1355 (1882).

[79] http://www.chemicalogic.com/download/co2_phase_daigram.pdf

[80] S. Circone et al., J. Phys. Chem. B **107**, 5529 (2003).

[81] T. Kawamura et al., J. Cryst. Growth **234**, 220 (2002).

[82] C. Giavarini et al., Energ. Fuel. **21**, 3284 (2007).

[83] K. Udachin et al., J. Phys. Chem. B **105**, 4200 (2001).

[84] M. Kirchner et al., J. Am. Chem. Soc. **126**, 9407 (2004).

[85] C. I. Ratcliffe and J. A. Ripmeester, J. Chem. Phys. **90**, 1259 (1986).

[86] R. J. Henning et al., J. Phys. Chem. A **104**, 5066 (2000).

[87] Aoki et al., Science **263**, 356 (1994).

[88] A. Klapproth et al., Can. J. Phys. **81**, 503 (2003).

[89] H. Hirai et al., Proc. Japan Acad. Ser. B **78**, 39 (2002).

[90] R. I. Flacau. "Structural and Electron Density Changes in Dense Guest-Host Systems: Analysis of X-ray Diffraction Data by the Rietveld and Maximum Entropy Methods." PhD thesis. U. of Ottawa, ON (2008).

[91] L. Yang et al., Proc. Natl. Acad. Sci. **106**, 6060 (2009).

[92] V. R. Belosludov et al., J. Supramol. Chem. **2**, 453 (2002).

[93] B. Chazallon and W. F. Kuhs, J. Chem. Phys. **117**(1), 308 (2002).

[94] A. K. Sum et al., J. Phys. Chem. B **101**, 7371 (1997).

[95] Y. P. Handa, J. Chem. Therm. **18**, 891 (1986).

[96] T. Ikeda et al., J. Phys. Chem. Solids **60**, 1527 (1999).

[97] L. Yang et al., Chem. Phys. Lett. **485**, 104 (2010).

[98] C. A. Tulk et al., J. Chem. Phys. **104**(20), 7854 (1996).

[99] C. Kamb, Science **150**, 205 (1965).

[100] R. T. Downs and M. S. Somayazulu, Acta Cryst. C **54**, 897 (1998).

[101] B. Olinger, J. Chem. Phys. **77**(12), 6255 (1982).

[102] S. W. Bailey, Rev. Mineral. **19**, 9 (1988).

[103] C. T. Johnston et al., Geophys. Res. Lett. **29**(6), 17 (2002).

[104] C. T. Johnston, Clay Mineral. **45**, 245 (2010).

[105] L. Gianfreda et al., Soil Mineral-Organic Matter-Microorganism Interactions and Ecosystem Health : Ecological Significance of the Interactions among Clay Minerals, Organic Matter and soil Biota. Vol **28B**, 301 (2002).

[106] R. E. Newnham and G. W. Brindley, Acta Cryst. **9**, 759 (1956).

[107] C. T. Johnston et al., Am. Mineral. **83**, 75 (1998).